TOPOLOGICAL DEFECTS IN FRUSTRATED NEMATICS

Pavlo Kurioz

Doctoral Dissertation
Jožef Stefan International Postgraduate School
Ljubljana, Slovenia

Supervisor: Prof. Dr. Samo Kralj, Jožef Stefan Institute, Ljubljana, Slovenia, University of Maribor, Maribor, Slovenia
Co-Supervisor: Assist. Prof. Dr. Milan Ambrožič, University of Maribor, Maribor, Slovenia

Evaluation Board:
Prof. Dr. Aleksander Zidanšek, Chair, University of Maribor, Maribor, Slovenia, Jožef Stefan International Postgraduate School, Ljubljana, Slovenia
Prof. Dr. Zdravko Kutnjak, Member, Jožef Stefan Institute, Ljubljana, Slovenia
Prof. Dr. Sylwester Rzoska, Member, Institute of High Pressure Physics, Polish Academy of Sciences, Warsaw, Poland

MEDNARODNA PODIPLOMSKA ŠOLA JOŽEFA STEFANA
JOŽEF STEFAN INTERNATIONAL POSTGRADUATE SCHOOL

Pavlo Kurioz

TOPOLOGICAL DEFECTS IN FRUSTRATED NEMATICS

Doctoral Dissertation

TOPOLOŠKI DEFEKTI V FRUSTRIRANIH NEMATIKIH

Doktorska disertacija

Supervisor: Prof. Dr. Samo Kralj

Co-Supervisor: Assist. Prof. Dr. Milan Ambrožič

Ljubljana, Slovenia, January 2019

Acknowledgments

First and foremost, I would like to express my sincere gratitude to my advisor Prof. Dr. Samo Kralj for the continuous support of my Ph.D. study and related research, for his patience, motivation, and immense knowledge. His guidance helped me in all the time of research and writing of this thesis. I was deeply honored to have an opportunity to work with him. The door to Prof. Samo Kralj office was always open whenever I ran into a trouble spot or had a question about my research or writing. I could not have imagined having a better advisor and mentor for my Ph.D.

I would also like to acknowledge Dr. Milan Ambrožič as the second supervisor of this thesis, and I am gratefully indebted to his for his very valuable comments on this thesis that greatly improved the manuscript. Our meetings have resulted in the interesting work and simultaneously deepened my understanding of dynamical behaviour of nematic liquid crystals.

To continue, I would like to thank Prof. Dr. Aleš Iglič for his excellent comments and insights on our articles.

I am also very grateful to Dr. Georgios Cordoyiannis for helpful suggestions and insightful comments.

Furthermore, I also thank Public Scholarship, Development, Disability and Maintenance Fund of the Republic of Slovenia for providing financial support through my doctoral studies.

Last but not the least; I would like to thank my colleagues, my friends, and my family for supporting me spiritually throughout writing this thesis and my life in general. Thank you.

Abstract

The dissertation considers singular topological defects (TDs) and also dynamic solition-like excitations in nematic liquid crystals (NLCs). TDs are an inevitable consequence of continuous symmetry breaking phase transitions, which are ubiquitous in nature. Due to topological origin TDs display several universalities and therefore bridge diverse fields of physics. Furthermore, fields might represent fundamental entities of nature and possible candidates for “fundamental particles” could be TDs. Consequently, it is of interest to identify systems in which TDs are relatively easy created, manipulated and experimentally observed. For this purpose, NLC configurations represent ideal testing grounds due to their unique combination of softness, liquid character, optical anisotropy&transparency and a large diversity of TDs that they display. In fact, NLCs are even named after TDs.

Our investigations were directed towards an understanding of general mechanisms to generate, stabilize and manipulate singular and nonsingular topological excitations. In particular, we consider configurations to which we enforce relatively large topological charges, we demonstrate new electrostatic analogies, we analyze the impact of extrinsic curvature on number and position of TDs, we study interactions between appropriate nanoparticles (NPs) and TDs, and we analyze dynamically generated topological excitations in plane-parallel cells. The work consists of theoretical modeling and numerical simulations. Defect structures are described either by the nematic tensor order parameter or the nematic director field. In the former case, the Landau-de Gennes phenomenological approach was used. In the latter case, we used the Lebwohl-Lasher lattice type modeling.

In quasi-two-dimensional (2D) planar systems, we demonstrate that confinement-enforced total topological charge $m \gg 1$ decays into elementary TDs bearing charge $m = 1/2$. These assemble close to the bounding substrate to enable essentially bulk-like uniform nematic ordering in the central part of a system. This effect is reminiscent of the Faraday cavity phenomenon in electrostatics. In addition, we showed that the total topological charge within a 2D region enclosed by a boundary possessing sharp edges is not uniquely defined due to the head-to-tail invariance of nematic ordering. In this study, a nematic LC was confined within a square, where the strong tangential anchoring condition was enforced at the boundaries. We demonstrated that using an external electric field one could switch between different topological configurations without melting NLC. In addition, we demonstrated that "domain"-type reorientations could be enabled by creation or/and annihilation of pairs $\{defect, antidefect\}$. Finally, we analysed topologically enforced structures consisting of several TDs where the total topological charge of the system was zero. We investigated possible mechanism which would trigger annihilation of TDs into a defect-free state. Our analysis revealed different annihilation channels which are in general relatively strongly sensitive to various perturbations. We also observed that in certain confinement geometries varying the order parameter correlation length size could trigger global rotation of an assembly of TDs. Finally, we showed in three-dimensional (3D) that an external electric field could be used to drag the boojum fingertip towards a confinement cell interior. This proof-of-concept reveals that assemblies of TDs could be exploited as

movable traps for appropriate nanoparticles, opening several opportunities for development of functional nanodevices.

In curved geometries, we analyzed the impact of intrinsic and extrinsic curvature on the distribution of TDs in 2D patches exhibiting negative Gaussian curvature. As model geometries, we choose catenoids and pseudospheres. Such geometries are often locally present in biological membranes. For example, catenoids roughly mimic neck-like shapes which appear in membrane fission, fusion or budding processes. On the other hand, pseudospheres roughly mimic structures realized in inter-membrane cellular cargo exchange. We demonstrated that defects robustly assemble in regions exhibiting strong enough localized distortions in the substrate curvature field. In particular, we investigated the impact of extrinsic curvature on TDs, which has been in most studies so far neglected. Our analysis revealed that the extrinsic curvature contributions are in general always present and are of comparable strength with respect to the intrinsic curvature contributions. Furthermore, we showed that the extrinsic curvature strongly affects the position of TDs in geometries exhibiting the negative Gaussian curvature. We also demonstrated that local assembling tendency of TDs can be well predicted by the Effective Topological Charge Cancellation mechanism.

Finally, we studied NLC confined in a plane-parallel cell which enforces the so-called double easy axis at the confining plates. In addition, a rotating external field was present. The resulting frustrations yielded complex patterns and dynamics if the external field was strong enough to enable synchronized global nematic order dynamics. Of particular interest were conditions suggesting the presence of the edge of chaos. On approaching this regime, we obtain diverse and complex nematic patterns on varying the external field frequency.

Keywords: Topological defects, continuum fields, nematic liquid crystals, confinement, Gaussian curvature, intrinsic curvature, extrinsic curvature, nanoparticles, electrostatic analogy, Landau-de Gennes formalism, Lebwohl-Lasher lattice model

Povzetek

V tej doktorski disertaciji se ukvarjamo s singularnimi topološkimi defekti (TD) in tudi z dinamičnimi solitonskimi vzbujanji v nematičnih tekočih kristalih (NTK). TD nastanejo kot neizbežna posledica zloma zvezne simetrije in spremljajočih faznih prehodov, ki so v naravi splošno značilni. Zaradi topološkega izvora kažejo TD veliko univerzalnih značilnosti, tako da povezujejo različna fizikalna področja. Poleg tega so morda polja osnovni gradniki v naravi in so tako mogoči kandidati za "osnovne delce " prav TD. Zato je zanimivo in pomembno najti fizikalne sisteme, kjer nastanejo TD razmeroma enostavno in kjer se jih da kontrolirati in eksperimentalno opazovati. V ta namen lahko imamo razne konfiguracije NTK za idealne testne sisteme, in sicer tako zaradi njihove enkratne kombinacije mehkosti, tekočinskih lastnosti, optične anizotropije in prozornosti, kot tudi zaradi velike raznovrstnosti njihovih struktur. Pravzaprav izhaja ime NTK (nematiki) ravno zaradi TD, ki so prisotni v njih.

Naše raziskave so bile usmerjene k razumevanju splošnih mehanizmov za nastanek, stabilizacijo in kontroliranje singularnih in nesingularnih topoloških ekscitacij. V našem primeru obravnavamo konfiguracije, ki jim lahko vsilimo razmeroma velike topološke naboje, prikažemo nove analogije z elektrostatiko, analiziramo vpliv zunanje ukrivljenosti na število in položaj TD, študiramo interakcije med ustreznimi nanodelci (ND) in TD in preučujemo dinamično generirane topološke ekscitacije v plan-paralelnih celicah. Delo sestavljajo teoretično modeliranje in numerične simulacije. Defektne strukture so opisane z nematičnim ureditvenim parametrom kot tenzorjem ali pa z nematičnim direktorskim poljem. V prvem primeru uporabimo fenomenološki Landau-de Gennesov pristop, v drugem primeru pa modeliranje Lebwohl-Lasherjevega mrežnega tipa.

Za kvazi-dvodimenzionalne (2D) planarne sisteme pokažemo, da celotni topološki naboj $m \gg 1$, ki je bil sistemu vsiljen zaradi geometrijske omejenosti, razpade v elementarne TD, ki nosijo naboj $m = 1/2$. Le–ti se nabirajo blizu mejne površine, zato da omogočijo praktično enakomerno prostorninsko nematično ureditev v centralnem delu sistema. Ta pojav spominja na učinek Faradayeve kletke v elektrostatiki. Pokazali smo tudi, da celotni topološki naboj znotraj 2D območja, omejenega z ostro definiranimi robovi, ni enolično določen zaradi »glava-rep«–invariantnosti nematične ureditve. V tej študiji je bil NTK omejen v kvadratu, kjer je bilo na mejnih stranicah vsiljeno močno tangentno sidranje. Pokazali smo, da lahko z uporabo zunanjega električnega polja preklapljamo med različnimi topološkimi konfiguracijami brez stalitve NTK faze. Pokazali smo tudi, da so reorientacije "domenskega" tipa lahko omogočene z nastankom in/ali anihilacijo parov {*defekt,antidefekt*}. Poleg tega smo analizirali topološko vsiljene strukture, sestavljene iz številnih TD, a s celotnim topološkim nabojem sistema enakim nič. Raziskali smo mogoče mehanizme, ki bi lahko sprožili anihilacijo vseh TD in privedli sistem v brezdefektno stanje. Naša analiza je razkrila različne anihilacijske načine, ki pa so v splošnem zelo občutljivi na razne motnje. Opazili smo tudi, da lahko v določenih omejitvenih geometrijah spreminjanje velikosti korelacijske dolžine, povezane z ureditvenim parametrom, sproži globalno vrtenje celotne strukture TD. Nazadnje smo pokazali za sistem v treh dimenzijah (3D), da lahko uporabimo električno polje za premikanje »boojum« strukture proti notranjosti celice.

Dokaz tega koncepta kaže na to, da lahko skupke TD izkoristimo kot gibljive pasti za ustrezne nanodelce, to pa odpira številne priložnosti za razvoj funkcionalnih nano-naprav.

V ukrivljenih geometrijah smo analizirali vpliv intrinzične in ekstrinzične ukrivljenosti na porazdelitev topoloških defektov v 2D vzorcih z negativno Gaussovo ukrivljenostjo. Kot modelni geometriji smo izbrali katenoide in psevdosfere. Takšne geometrije so pogosto lokalno prisotne v bioloških membranah. Na primer, katenoidi približno ponazarjajo oblike z vratom, ki se pojavljajo pri odcepljanju, zlivanju membran ali pa pri brstenju. Po drugi strani psevdosfere približno ponazarjajo strukture, nastale za izmenjavo snovi med celicami prek membran. Pokazali smo, da se defekti robustno zbirajo v območjih z dovolj močnimi lokalnimi distorzijami polja ukrivljenosti zaradi geometrije. Posebej smo raziskovali vpliv ekstrinzične ukrivljenosti na TD, ki je bil doslej v večini študij zanemarjen. Naša analiza je potrdila, da so prispevki na strukturo zaradi ekstrinzične ukrivljenosti v splošnem vedno prisotni in so primerljivi s tistimi zaradi intrinzične ukrivljenosti. Dalje smo pokazali, da ekstrinzična ukrivljenost močno vpliva na položaj TD v geometrijah z negativno Gaussovo ukrivljenostjo. Potrdili smo tudi, da se da tendenco lokalnega grupiranja TD dobro napovedati z mehanizmom »efektivnega izničevanja topološkega naboja«.

Nazadnje smo študirali NTK, omejen v plan-paralelni celici, ki vsiljuje tako imenovano dvojno »lahko« (preferenčno) os na mejnih ploščah. Prisotno je bilo tudi rotirajoče zunanje električno polje. Posledične frustracije so povzročile kompleksne vzorce in dinamiko, če je bilo zunanje polje dovolj močno, da je omogočilo sinhrono dinamiko globalne nematične ureditve. Posebno zanimivi so bili pogoji, ki so napovedovali/prikazovali dogajanje na robu kaosa. Z bližanjem temu režimu dobimo pri spreminjanju rotacijske frekvence zunanjega polja raznolike in kompleksne nematične vzorce.

Ključne besede: Topološki defekti, nematični tekoči kristali, ograjenost, elektrostatična analogija, topološki naboj, Gaussova ukrivljenost, zunanja ukrivljenost, notranja ukrivljenost, nanodelci, elektrostatična analogija, Landau-de Gennesov formalizem, Lebwohl-Lasherjev mrežni model

Contents

List of Figures

Abbreviations

AFM ... atomic force microscope
BAC ... boundary anchoring conditions
ETCC ... effective topological charge cancellation
FM ... ferromagnetic
LC ... liquid crystal
NLC ... nematic liquid crystal
NP ... nanoparticle
SAC ... surface anchoring consitions
Sm A ... smectic A
TD ... topological defect
TDL ... twist disclination line
WDL ... wedge disclinaion line
TDL ... twist disclination line
2D ... two-dimensional
3D ... three-dimensional

Chapter 1

Introduction

Topological defects (TDs) are an unavoidable consequence of continuous symmetry breaking phase transitions [1-3]. For this reason, they are ubiquitous in nature and present in all branches of physics, including particle physics, condensed matter physics, and cosmology. Due to their topological origin [2] the key properties of TDs are independent of the system microscopic details. The most essential property of TDs is their topological charge q [1, 2, 3] which is a conserved quantity. It is defined based on the topological properties of the relevant order parameter space [2]. In two dimensions, q is equivalent to the winding number m. Consequently, they display several universalities [3]. TDs are relatively energetically costly and in general, it is difficult to stabilize a large number of TDs bearing a relatively large topological charge in equilibrium. There is growing evidence [4, 5] that fields represent basic entities of nature, and not particles. If this is the case, TDs might be a possible candidate to play the role of fundamental particles [5]. Furthermore, in condensed matter systems TDs could have a strong impact on mechanical, electromagnetic, electro-optical properties of materials [6].

For these reasons, it is of high interest to find appropriate systems where the fundamental behavior of TDs could be relatively easily studied [3]. Such systems should possess (i) variety of qualitatively different TDs; (ii) they should be experimentally approachable and (iii) could be manipulated with ease. For this purpose, liquid crystal (LC) phases are particularly adequate. LCs exhibit a unique combination of liquid character, ordering, softness, and optical anisotropy [7, 8, 9]. The condition (i) is fulfilled due to a variety of bulk or confined LC configurations exhibiting orientational or even translational order. The condition (ii) is realized owing to their liquid character, optical transparency, and anisotropy. The condition (iii) arises due to their softness, which is the consequence of continuous symmetry breaking phase transitions via which LC configurations are reached and due to relatively weak intermolecular interactions.

It is of fundamental interest to identify robust mechanisms, which could stabilize structures possessing either a large number of TDs or TDs exhibiting large topological charges [10]. In planar geometries, one could stabilize them in nematic LC cells by Atomic Force Measurement (AFM) inscribing method [11, 12]. Via computer controlled AFM it is possible to enforce a practically arbitrary pattern of TDs [11]. For example, in recent experiments they have stabilized alternating networks of "surface" TDs bearing winding numbers $m = \pm 1$ and $m = \pm 2$ [10, 11]. It is of strong interest to determine conditions for which configurations of TDs possessing relatively large topological charge could be stabilized. Furthermore, several studies indicate that one could stabilize complex patterns of TDs in effectively two-dimensional (2D) systems by exploiting curvature of surfaces confining a nematic LC. Numerous theoretical and numerical studies concerning topology and TDs have been performed in a 2D system [13-20]. Relatively simple XY-type models were typically used [13, 14, 16, 18]. Namely, they are well mathematically accessible and

in some cases, they are "transparent" enough to obtain relatively simple analytic solutions. Impact of topology on TDs is most visible via the Gaussian curvature K. According to the famous Gauss-Bonnet and Poincaré-Hopf theorems [21] the total winding number m_{tot} of TDs within a closed surface possessing in-plane order is determined by the total surface integral of K. Several works demonstrated [13, 18] the electrostatic analogy where K and m play the role of an electric field and electric charges, respectively. Analytic derivations and numerical simulations reveal that positive (negative) Gaussian curvature is mathematically equivalent to a smeared negative (positive) topological charge [18]. Furthermore, it has been demonstrated that surfaces exhibiting regions with both positive and negative K could trigger unbinding of pairs {*defect, antidefect*} [16, 18]. Here *defects* and *antidefects* refer to TDs bearing $m > 0$ and $m < 0$, respectively. In general, geometry influences the structure of an order parameter field within a 2D manifold via two qualitatively different elastic contributions [20], referred to as the *intrinsic* and *extrinsic* terms, respectively. For example, if an in-plane ordering is presented by a vector field $\mathbf{v}$, then the *intrinsic* terms penalize departures of $\mathbf{v}$ from surface geodesics [21]. They are associated with variations of $\mathbf{v}$, as it would live only within the 2D curved surface. On the contrary, the *extrinsic* terms quantify elastic costs of out-of-surface gradients in $\mathbf{v}$. They are sensitive to how 2D manifold is embedded in three-dimensional (3D) Euclidian space. In cases where local principal curvatures are different, the *extrinsic* contributions generate an effective geometrically induced symmetry-breaking field. In general, the corresponding *extrinsic field* enforces alignment either along the maximal or minimal curvature principal direction, depending on the sign of the relevant extrinsic elastic constant. Its strength increases with increasing difference between the principal curvatures. However, in most studies so far [13-24] the impact of extrinsic contributions was neglected, although such terms are generally always present. Therefore, an omission of these terms is not justified by any theorem [25-30].

Complexity in behavior in systems exhibiting TDs is enormously increased if appropriate nanoparticles (NPs) are added to LC materials. Such studies are of hot recent interest. Studies reveal that TDs in LCs could efficiently positionally control assemblies of appropriate nanoparticles (NPs) [10, 31-33]. In general, there are roughly two different regimes of behavior depending on the value of the ratio $\mu = R/d_e$ [7]. Here R stands for the characteristic linear size of a nanoparticle and the surface extrapolation length d_e estimates impact of the nanoparticle on the surrounding order parameter field. The latter possesses two qualitatively different components [34]: an *amplitude* (also referred to as a *hydrodynamic*) *field*, and a *symmetry breaking* (also referred to as a *gauge* or *nonhydrodynamic*) *field*. If a nanoparticle's characteristic size is comparable to an order parameter's *amplitude* correlation length (which roughly estimates the core size of a defect), and if the nanoparticle does not sufficiently disturb the *symmetry breaking field* surrounding the defect's core (in such cases $\mu \sim 1$), then the defect could efficiently trap the NP due to the Defect Core Displacement (DCR) mechanism [32, 33]. Namely, in this case, a relatively energetically expensive defect core volume is (at least partially) replaced by NP's volume, thereby reducing the overall energy. It has been shown that lattices orientational (disclinations) [30, 31] and translational (dislocations) [32, 33] defects can readily trap such NPs. Furthermore, it was demonstrated that line defects could be exploited to form nanowire-type structures [33] consisting of NPs. On the contrary, in cases $\mu \gg 1$, NPs could enforce TDs in surrounding LC matrix. This behavior emerges if a nanoparticle distorts a local *symmetry-breaking field* similarly as a TD [30].

Despite the simplicity of most LC equilibrium phases, LC phases could exhibit a chaotic type of behavior under appropriate conditions [34-40]. In fact, they represent an ideal system for such studies due to their experimental accessibility and sensitivity to external

perturbations. However, so far studies on "chaotic" behavior in LCs are scarce [41, 42]. Chaotic behavior dominates nature and appears in strongly nonlinear systems for appropriate values of "control parameters" constraining global system's behavior. In particular, complexity anomalously increases on approaching the "edge of chaos" [36]. Classical systems, in which such behavior are commonly studied, represent mechanical oscillators, electrical circuits, lasers, nonlinear optical systems, chemical reactions, nerve cells, heated fluids [34]. Emergent behavior suggests several universal features. Nonlinear systems that undergo transitions from stationary to periodic and chaotic states can be classified according to their route to chaos [35]. Among them, one could distinguish irregular [36] and period-doubling behavior [37, 38]. In the latter case, the period of the system's oscillation doubles as a consequence of a change in the value of a relevant control parameter [39, 40]. In particular, some experimental observations report on external field driven a period-doubling behavior in LCs [41, 42]. Nonexistence of a stationary state for LC order parameter field could lead to non-trivial behavior called "tumbling" [43, 44]. Mastering such behavior in LCs could pave the way for novel bistable memory devices [45].

Gained understanding of basic mechanisms might pave the way to the development of LC-based new photonic devices or applications in biomedicine [46-51]. Furthermore, it could yield insight into fundamental open problems in nature. Namely, the interaction between TDs and curvature might explain the existence of dark matter and dark energy even within the standard model if one relaxes the assumption of essentially flat universe [52].

In the thesis, we have studied the aforementioned systems focusing on cases, which are still relatively weakly understood. We were interested in the key mechanisms that pave the way towards the understanding of general mechanisms that reveal how to generate, stabilize and manipulate singular and nonsingular topological excitations. For this purpose, we have described the defect structures by means of the nematic tensor order parameter and have analyzed them by using the Landau-de Gennes phenomenological approach. Within the model, we have considered either 2D or 3D systems, which exhibit either static or dynamic phenomena. We have studied the stabilization of TDs configurations bearing relatively large topological charges by enforcing relevant boundary conditions. We have shown that, in this case, TDs tend to assemble at a confining boundary. In the context of electrostatic analogy, the phenomenon reminiscent of the Faraday cavity effect is shown. We have observed that in certain confinement geometries, varying the order parameter correlation length size could trigger global rotation of an assembly of TDs. Next, special attention has been paid to the interactions between NPs and TDs in nematic LCs. We have shown in 3D that an external electric field could be used to drag the boojum fingertip towards a confinement cell interior.

Then, we have restricted our attention on 2D region enclosed by a boundary possessing sharp edges within which topological charge is not uniquely defined. We have demonstrated that using an external electric field one could switch between different topological configurations without melting NLC. We have analysed topologically enforced structures consisting of several TDs, where the total topological charge of the system was zero. We have studied a possible mechanism, which would trigger annihilation of TDs into a defect-free state.

Afterwards, we have investigated open nematic ordered films with the negative Gaussian curvature. We were interested in the impact of curved substrates on nematic ordering and TDs within them. To test this, we characterized curvatures by curvature fields, where the dominant role has been played by the Gaussian curvature and the mean curvature. Surfaces with the negative Gaussian curvature have been of particular interest since; in this case, positions of TDs strongly depend on elastic constants related to the

extrinsic curvature contributions. Particular emphasis is given to the investigation of the impact of *extrinsic* curvature on TDs, which has been in most studies so far neglected.

Finally, we have studied the impact of a rotational external field on nematic LCs confined within a plane-parallel cell, where the confining surfaces impose two different (perpendicular) easy axes. In order to model this, we described defect structures by the nematic director field and performing modeling in terms of the Lebwohl-Lasher lattice approach. We have studied diverse and complex nematic patterns on varying the rotation frequency and magnitude of the external field. In particular, we have shown that edge of chaos could be characterized by a period doubling mechanism.

The thesis is organized as follows. In Chapter 2 the basic theoretical background is present. In Section 2.1 the models used in our research are given. In Subsection 2.1.1 an overview of the semi-microscopic Lebwohl-Lasher lattice spin model of NLCs is presented. Subsection 2.1.2 is dedicated to reviewing the phenomenological Landau-de Gennes mesoscopic theory. Subsubsection 2.1.2.1 is devoted to describing the two-dimensional free energy density and the corresponding Euler-Lagrange equations. In Subsubsection 2.1.2.2 three-dimensional Landau-de Gennes energy density functional and appropriate differential equations for studying the extremal points of it are introduced. In addition, the interaction of TDs with nanoparticles is discussed. The impact of extrinsic and extrinsic curvatures is reflected in Section 2.2. The main theorems that establish the link between topology and geometry are highlighted in Subsections 2.2.1. In Subsection 2.2.2 surfaces with negative Gaussian curvature are discussed. The key differential geometry features of catenoid and pseudosphere are pointed out in Subsubsection 2.2.2.1 and 2.2.2.2, respectively.

The main results and findings of our study are presented and discussed in Chapter 3. In Section 3.1 we study the impact of the rotational external field on tumbling dynamics within a plane-parallel nematic cell. In Subsection 3.2.1 we study numerically the impact of geometry and topology on patterns and position of nematic TDs. We demonstrate in 2D that for confinements, which topologically enforce relatively large total topological defect, a phenomenon analogous to the Faraday cavity effect could be observed. Particular emphasis is given to collective rotation of a pattern of TDs on changing the defect core size. In Subsection 3.2.2 we reveal the phenomena that exist in confined nematics within sharp edges geometry associated with non-unique defined topological charge. Special attention is paid to continuous structural transitions driven by the external electric field. The Subsection 3.2.3 is devoted to 3D confined NLCs. We demonstrate how appropriately surface coated NPs could be efficiently trapped within the fingertip of a finger-like boojum TD. The study of nematic orientational ordering on surfaces with the negative Gaussian curvature is presented in Subsection 3.2.4. We numerically study the impact of intrinsic and extrinsic terms on numbers, positioning and assembling of TDs within the open ordered films. In addition, the impact of the presence of specific impurities on assembling of TDs is demonstrated.

The final concluding Chapter 4 summarizes the main conclusions of our study.

Chapter 2

Theoretical Background

2.1 Modeling

In this Section, a brief review of theoretical approaches are presented. In our research, both two- and three-dimensional systems are considered. In the first subsection semi-microscopic Lebwohl-Lasher lattice, the approach is introduced, whereas the second subsection is dedicated to mesoscopic Landau-de Gennes type modeling.

2.1.1 Semi-microscopic model

An overview of the semi-microscopic Lebwohl-Lasher lattice spin model of nematic liquid crystals is presented. We study the effect of the bistable surface free energy on the dynamical behavior.

The Lebwohl-Lasher lattice spin model [53] of a NLC is a lattice version of the Maier-Saupe mean field model [54]. Regarded as a prototype for studying the orientational phase transition, it has been used to predict the phase behavior of confined nematogens [55, 56, 57, 58].

One could represent the 3D spin model as a rectangular simulation lattice cell consisting of $M \times N \times L$ sites. In the model, each site is occupied by a nematic spin $\boldsymbol{S}_\alpha$, which is a unit vector and may point in any direction. Standing for LC molecules, the states $\pm\boldsymbol{S}_\alpha$ are taken to be physically equivalent, due to a head-to-tail invariance. Furthermore, they are able to freely rotate in the torque field of their neighbors. Each site is enumerated by a set of indices $\alpha = (i, j, k)$, where $1 \leq i \leq M$,$1 \leq j \leq N$, and $1 \leq k \leq L$. For convenience, the indices i, j and k determine the position of the site α with respect to the x-axis, y-axis and z-axis directions of the Cartesian coordinate system, respectively.

The free energy functional inside the cell is modeled by the sum of the terms of all spin sites:

$$F = \sum_\alpha f_\alpha, \tag{2.1}$$

with the energy term per spin (site):

$$f_\alpha = -\tfrac{1}{2}\sum_{nn} J_{\alpha,nn}\,(\boldsymbol{S}_\alpha \cdot \boldsymbol{S}_{nn})^2 - (\boldsymbol{S}_\alpha \cdot \boldsymbol{B})^2 + \delta_s \cdot f_s. \tag{2.2}$$

The first term defines the intermolecular interactions, namely the coupling between the local spin and its 6 nearest neighbors. The interaction potential tends to align neighbors

spins in parallel directions. The parameter J is set to be a coupling constant, which can have one of the three values, depending on three qualitatively different situations:

(1) $J_{ij} = 0$, if both neighbors are impurities (frozen spins);

(2) $J_{ij} = W$, if one is a nematic spin and the other is an impurity (mixed state);

(3) $J_{ij} = J > 0$, when both neighbors are LC spins.

In order to represent the impact of additional orientation disorder imposed by static impurities, some sites contain static (frozen) random spins instead of freely rotating spins. Consequently, being randomly positioned and oriented they tend to locally reorient the spin orientation in random directions. As a parameter, which measures how many impurities are introduced into the system, the probability p for the specific site to contain the impurity is chosen (to which we henceforth refer to the impurity concentration).

The second term stands for the interaction of all LC spins with the homogeneous external field $\boldsymbol{B}$. Specifically, $\boldsymbol{B} = (B_x, B_y, B_z)$ is a rotating field, with harmonic time variation of the components: $B_x = B_0 \sin\left(\frac{2\pi t}{t_0}\right)$, $B_y = 0$, $B_z = B_0 \cos\left(\frac{2\pi t}{t_0}\right)$, where B_0 is the amplitude, t_0 is the period of rotation.

The third term is the surface anchoring term for the spins at the bottom and upper cell boundary (the symbol δ_s denotes the value 1 for $k = 1$ or L, and 0 otherwise). According to dual axis theory [59], the surface free energy term has the following form:

$$f_s = \frac{X_1}{2}\sin^2\theta + \frac{X_2}{2}\cos^2\theta + \frac{X_3}{4}\sin^4\theta. \tag{2.3}$$

Here, θ is the angle between $\boldsymbol{e}_z = (0,0,1)$ direction and nematic spin at the surface. The energy term f_s mimics the competition between the homeotropic anchoring ($\theta = 0$) and degenerate planar anchoring ($\theta = \frac{\pi}{2}$). According to [60], all the X_1, X_2 and X_3 are positive. In this case, the homeotropic solution $\theta = 0$ is stable (a positive second derivate of f_s with respect to θ) for $X_1 > X_2$, while the tilted anchoring solution $\theta = \arcsin\sqrt{\frac{(X_2 - X_1)}{X_3}}$ is stable for $X_1 < X_2$. This is not appropriate for our problem, because we want to have two minima, i. e., bistable surface free energy. We introduce $W_s = X_1 - X_2$ and express the surface energy as:

$$f_s = W_s(\tfrac{1}{2}\sin^2\theta - \tfrac{\gamma}{4}\sin^4\theta). \tag{2.4}$$

W_s and γ are supposed to be positive. For $\gamma > 1$ the functional f_s has minima at $\theta = 0$ and $\theta = \frac{\pi}{2}$ with the values:

$$f_s(0) = 0, \tag{2.5}$$

$$f_s(\tfrac{\pi}{2}) = \tfrac{W_s}{4}(2 - \gamma). \tag{2.6}$$

The maximum ("potential barrier") is:

$$\theta_{max} = \arcsin\sqrt{\frac{1}{\gamma}}\,, \tag{2.7}$$

$$f_s(\theta_{max}) = \frac{W_s}{4\gamma}. \tag{2.8}$$

We can treat the value from Eq. (2.8), $\Delta f_{\rightarrow} = \frac{W_s}{4\gamma}$, as the potential barrier for the transition of the structure from the left to the right minimum. The value of dimensionless parameter γ also determines which minimum is deeper: at $\theta = 0$ or $\theta = \frac{\pi}{2}$; if we choose $\gamma > 2$, the deeper minimum is $f_s(\frac{\pi}{2}) < 0$. In this case, the effective potential barrier for the transition from the right to the left minimum is:

$$\Delta f_{\leftarrow} = f_s(\theta_{max}) - f_s\left(\frac{\pi}{2}\right) = \frac{W_s}{4}\left(\gamma + \frac{1}{\gamma} - 2\right). \tag{2.9}$$

The potential defined by Eq. (2.4) can be rewritten in a similar form as the field term:

$$f_s = W_s\left(\frac{1}{2}(1 - (\boldsymbol{S}_\alpha \cdot \boldsymbol{e}_z)^2) - \frac{\gamma}{4}(1 - (\boldsymbol{S}_\alpha \cdot \boldsymbol{e}_z)^2)^2\right), \tag{2.10}$$

or if we square the second term and drop constant terms:

$$f_s = -\frac{(1-\gamma)W_s}{2}(\boldsymbol{S}_\alpha \cdot \boldsymbol{e}_z)^2 - \frac{\gamma W_s}{4}(\boldsymbol{S}_\alpha \cdot \boldsymbol{e}_z)^4. \tag{2.11}$$

Then, when we minimize the total free energy Eq. (2.1) with respect to all (non-frozen) spin components, regarding the three components of the same spin as independent variables in this minimization, we must still take into account that $\boldsymbol{S}_\alpha$ is the unit vector: $|\boldsymbol{S}_\alpha| = 1$. In order to satisfy the normalization of the spin vectors, the "operational" total free energy reads:

$$F^* = \textstyle\sum_\alpha f^*_\alpha, \tag{2.12}$$

where

$$f^*_\alpha = \lambda_\alpha(S^2_\alpha - 1) + f_\alpha, \tag{2.13}$$

with additional Lagrange multipliers λ_{ijk}, which also have to be found in order to solve the system. When the normalization of spins is strictly fulfilled, then free energies F and F^* are exactly equal. To shorten the notation in the following derivation, let us denote the spin in a specific site (site α) simply with $\boldsymbol{S}$. Its components are correspondingly denoted by $\boldsymbol{S}_b$, $b = 1 - 3$, with $S_1 \equiv S_x$, $S_2 \equiv S_y$, $S_3 \equiv S_z$. When minimizing the free energy, we notice that all the energy terms in free energy per site Eq. (2.2) are of the same type: $f_s \equiv -W_s(\boldsymbol{S} \cdot \boldsymbol{e})^n$, where n is a natural exponent (2 or 4 in our case). In addition, the interaction term between the neighboring spins is of the same type, since we can take $\boldsymbol{e} = \boldsymbol{S}_{nn}$ for any of nearest neighbors. Because of the head-to-tail invariance (i.e., $\boldsymbol{S} \equiv -\boldsymbol{S}$) of the nematic director, it is natural to take $n = 2$ for the interactions concerning the NLCs. However, the same model can be also used to study binary systems, where for instance, ferromagnetic (FM) particles are included in NLC which direct FM – FM coupling is modeled with the Heisenberg free energy ($n = 1$). Thus, to consider what term in the equilibrium equations results from the free energy term $-W_s(\boldsymbol{S} \cdot \boldsymbol{e})^n$, including the corresponding Lagrange multiplier (now shortly denoted by λ), it suffices to write just that part of F^* which includes S_β and set its derivative to zero:

$$F^* = \lambda S^2_\beta - W_s(S_1 e_1 + S_2 e_2 + S_3 e_3)^n, \tag{2.14}$$

$$\tfrac{\partial F^*}{\partial S_\beta} = 2\lambda S_\beta - nW_s(S_1 e_1 + S_2 e_2 + S_3 e_3)^{n-1} \cdot e_\beta = 0. \tag{2.15}$$

It is a system of 3 equations:

$$\lambda S_1 - \frac{nW_s}{2}(\boldsymbol{S}\ \cdot \boldsymbol{e})^{n-1} \cdot \boldsymbol{e}_1 = 0, \tag{2.16}$$

$$\lambda S_2 - \frac{nW_s}{2}(\boldsymbol{S}\ \cdot \boldsymbol{e})^{n-1} \cdot \boldsymbol{e}_2 = 0, \tag{2.17}$$

$$\lambda S_3 - \frac{nW_s}{2}(\boldsymbol{S}\ \cdot \boldsymbol{e})^{n-1} \cdot \boldsymbol{e}_3 = 0. \tag{2.18}$$

In order to obtain the multiplier λ first, we multiply the first equation with S_1, the second with S_2 and the third with S_3, and then we sum them. By taking again $S_1^2 + S_2^2 + S_3^2 = 1$ on the left side of the equation, we obtain:

$$\lambda = \frac{nW_s}{2}(\boldsymbol{S}\ \cdot \boldsymbol{e})^{n}. \tag{2.19}$$

Inserting this value of λ in Eqs. (2.16, 2.17, 2.18) again, we can write them compactly in a vector form:

$$\boldsymbol{R}^{(n)} = 0, \tag{2.20}$$

with the vector residuum on the left side depending on power n:

$$\boldsymbol{R}^{(n)} = nW\boldsymbol{g}^{(n)}(\boldsymbol{S}, \boldsymbol{e}), \tag{2.21}$$

where

$$\boldsymbol{g}^{(n)}(\boldsymbol{S}, \boldsymbol{e}) = (\boldsymbol{S}, \boldsymbol{e})^{n-1}[(\boldsymbol{S}, \boldsymbol{e})\boldsymbol{S} - \boldsymbol{e}]. \tag{2.22}$$

The complete set of equilibrium equations corresponding to the free energy (2.1) can be expressed as:

$$\boldsymbol{R}_\alpha = 0, \tag{2.23}$$

$$\boldsymbol{R}_\alpha = 2\sum_{nn} J_{\alpha,nn}\boldsymbol{g}^{(2)}(\boldsymbol{S}_\alpha, \boldsymbol{S}_{nn}) + 2B^2\boldsymbol{g}^{(2)}(\boldsymbol{S}_\alpha, \boldsymbol{e}_z) + \delta_s\boldsymbol{R}_{\alpha S}, \tag{2.24}$$

where the functions defined by Eq.(2.22) are taken and the surface residual term (just for sites with $k = 1$ or $k = L$) is written separately as:

$$\boldsymbol{R}_{\alpha S} = W_s[(1-\gamma)\boldsymbol{g}^{(2)}(\boldsymbol{S}_\alpha, \boldsymbol{e}_z) + \gamma\boldsymbol{g}^{(4)}(\boldsymbol{S}_\alpha, \boldsymbol{e}_z)]. \tag{2.25}$$

We also mention that the residuum corresponding to $\alpha-$th spin may be formally written as:

$$\boldsymbol{R}_\alpha = \frac{\partial F^*}{\partial \boldsymbol{S}_\alpha}. \tag{2.26}$$

After the equilibrium Eqs. (2.23, 2.24, 2.25) have been set up ($3MNL$ scalar equations altogether if no spins are frozen), they are to be solved by relaxation methods. If we also consider thermal fluctuations, the corresponding relaxation equations are:

$$\boldsymbol{S}_\alpha(new) = \boldsymbol{S}_\alpha(old) + \frac{D\Delta t}{kT} \cdot \frac{\partial F^*}{\partial \boldsymbol{S}_\alpha}(old) + \Delta\boldsymbol{S}_T. \tag{2.27}$$

Here D is the appropriate degenerated rotation diffusion tensor of the system and k is the Boltzmann constant. The first term on the right side of Eq. (2.27) corresponds to mechanical torque, which tends to rotate the spin towards equilibrium, while the second term $\Delta \boldsymbol{S}_T$ represents random thermal fluctuation. Eq. (2.27) means one iteration or one sweep over all lattice sites. If we introduce dimensionless time step and temperature $\Delta t^* = Dt$, $T^* = \frac{kT}{J}$, and use Eq. (2.4) with dimensionless residuum vector Eq. (2.26): we obtain the corresponding numerical equation:

$$\boldsymbol{S}_\alpha(new) = \boldsymbol{S}_\alpha(old) + \tfrac{\Delta t^*}{T^*} \cdot \boldsymbol{R}_\alpha(old) + \Delta \boldsymbol{S}_T. \tag{2.28}$$

The appropriate dimensionless time interval $\Delta t^* = 0.01$ is chosen as the input parameter. We also set $J = 1$ so that the free energy itself becomes dimensionless.

Note that during relaxation process the external field B_0 varies with time as a sine function, thus, it is appropriate to define its period t_0 as well as the total relaxation time t in dimensionless units of Δt^* Parametrization of the response of the spin configuration to the time varying field is defined as the response only in z-direction:

$$g(t) = \left(\frac{B_z}{B}\right)^2 \langle S_z^2 \rangle. \tag{2.29}$$

The brackets $\langle ... \rangle$ denote the average over the spin configurations.

In the simplest rotational case, Eq. (2.29) can be rewritten as:

$$g(t) = \cos^2\left(\frac{2\pi t}{t_0}\right)^2 \langle S_z^2 \rangle. \tag{2.30}$$

The corresponding total response is obtained as time averages of response defined by Eq. (2.29):

$$\langle g \rangle = \frac{1}{\iota} \int_0^\iota g(t)\, dt. \tag{2.31}$$

The averaging time ι may be one or more periods t_0.

2.1.2 Landau-de Gennes mesoscopic model

In this Subsection, the mesoscopic Landau-de Gennes type modeling in two- and three-dimensions is introduced. Special attention is paid to the curved geometries in two dimensions, which are described with curvature fields. For both cases, the corresponding Euler-Lagrange equations are given. Further, the interaction between NP's surface and LC surrounding is discussed.

2.1.2.1 Two-dimensional free energy

Of our interest is to study the ordered soft films displaying nematic in-plane ordering. For this purpose, we restrict our attention to 2D films, which properties are described by the curvature tensor $\boldsymbol{C}$ and the surface order tensor $\boldsymbol{Q}$.

The curvature of a local membrane surface patch, corresponding to a point at the mesoscopic scale, is characterised by the curvature tensor field [61,62]:

$$C = C_1 \boldsymbol{e}_1 \otimes \boldsymbol{e}_1 + C_2 \boldsymbol{e}_2 \otimes \boldsymbol{e}_2, \tag{2.32}$$

where the unit vectors $\{\boldsymbol{e}_1, \boldsymbol{e}_2\}$ point along the surface principal directions with principal curvatures $\{C_1, C_2\}$, where $\boldsymbol{v} = \boldsymbol{e}_1 \times \boldsymbol{e}_2$ defines the local surface normal, $\otimes$ stands for the tensor product. The local nematic orientational order is described by the traceless and symmetric tensor order parameter field [63]:

$$\boldsymbol{Q} = q_1(\boldsymbol{e}_1 \otimes \boldsymbol{e}_1 - \boldsymbol{e}_2 \otimes \boldsymbol{e}_2) + q_2(\boldsymbol{e}_1 \otimes \boldsymbol{e}_2 + \boldsymbol{e}_2 \otimes \boldsymbol{e}_1), \tag{2.33}$$

where q_1 and q_2 are scalars. In the diagonal form, $\boldsymbol{Q}$ can be expressed as [17]:

$$\boldsymbol{Q} = \lambda(\boldsymbol{n} \otimes \boldsymbol{n} - \boldsymbol{n}_\perp \otimes \boldsymbol{n}_\perp), \tag{2.34}$$

where

$$\boldsymbol{n} = \cos\eta\, \boldsymbol{e}_1 + \sin\eta\, \boldsymbol{e}_2, \tag{2.35}$$

$$\boldsymbol{n}_\perp = -\sin\eta\, \boldsymbol{e}_1 + \cos\eta\, \boldsymbol{e}_2. \tag{2.36}$$

The quantity λ determines the amplitude field and $\boldsymbol{n}$ plays the role of the gauge field [64], η is the angle between the nematic director field and the base vector $\boldsymbol{e}_1$. Here, $\{\boldsymbol{n}, \boldsymbol{n}_\perp\}$ are the eigenvectors of $\boldsymbol{Q}$ corresponding to the eigenvalues of $\{\lambda, -\lambda\}$. By comparing Eqs. (2.33) and (2.34) we obtain [17, 63]:

$$\lambda = \sqrt{q_1^2 + q_2^2}. \tag{2.37}$$

The positive eigenvalue $\lambda \in [0, \frac{1}{2}]$ of $\boldsymbol{Q}$ measures the extent of orientational ordering. In the case $\lambda = 0$ orientational order is absent, whereas the largest degree of order corresponds to $\lambda = 1/2$. The former state in general fingerprints positions of TDs. The corresponding unit eigenvector $\boldsymbol{n}$ defines the local nematic order and is commonly referred to as the nematic director field. Note that at the origin of defects $\boldsymbol{n}$ is not uniquely defined and consequently $\lambda = 0$.

In terms of $\boldsymbol{C}$ and $\boldsymbol{Q}$, we express the free energy density as the sum $f = f_b + f_c + f_e^{(int)} + f_e^{(ext)}$ of surface bending (f_b), nematic condensation (f_c), intrinsic elastic ($f_e^{(int)}$) and extrinsic elastic ($f_e^{(ext)}$) contributions, where [65]:

$$f_b = \tfrac{\kappa}{2}\big(Tr(\boldsymbol{C})\big)^2, \tag{2.38}$$

$$f_c = -aTr(\boldsymbol{Q^2}) + b\Big(Tr(\boldsymbol{Q^2})\Big)^2, \tag{2.39}$$

$$f_e^{(int)} = k_i(Tr(\boldsymbol{\nabla}_S \boldsymbol{Q})^2), \tag{2.40}$$

$$f_e^{(ext)} = k_e^{(1)} Tr(\boldsymbol{QC})^2 + k_e^{(2)} Tr(\boldsymbol{C}^2\boldsymbol{Q}^2). \tag{2.41}$$

The parameters entering Eqs. (2.38, 2.39, 2.40, 2.41) are the following. κ is the membrane bending modulus. $a = a_0(T - T_c)$, T determines the temperature, a_0 and b stand for the Landau coefficients, T_c is the phase transition temperature. Note that the cubic term is absent. Namely, the nematic tensor order parameter is traceless and consequently, in 2D, it follows $Tr(\boldsymbol{Q}^3) = 0$. Consequently, for a positive value of the third term, the system exhibits in bulk 2$^{\text{nd}}$ order isotropic-nematic phase transition on varying T. The coupling between orientational ordering and local curvature is determined by the

following quantities. The quantity $\boldsymbol{\nabla}_S$ defines the surface gradient operator [17]. k_i stands for the intrinsic elastic modulus and $\left\{k_e^{(1)}, k_e^{(2)}\right\}$ are extrinsic elastic constants [31].

The first term in Eq. (2.41) was introduced by Napoli [66], who arrived at it by deriving an effective 2D elastic energy density from the classical three-dimensional energy of a thin LC layer [1]. We refer to $k_e^{(1)}$ as the Napoli elastic constant. In terms of the principal curvatures, it follows:

$$f_e^{(ext,1)} = q_1(C_1^2 - C_2^2) \equiv -q_1 h_N, \tag{2.42}$$

where h_N stands for the Napoli field. In cases $h_N > 0$, this elastic term forces $\boldsymbol{n}$ to orient along $\boldsymbol{e_1}$ (meridians). Alternatively, when $h_N < 0$, the Napoli field forces $\boldsymbol{n}$ to be aligned along $\boldsymbol{e_2}$ (parallels).

Note that in case of minimal curvature the first term in Eq. (2.41) is equal to zero. For instance, for the catenoid geometry, it holds $C_1 = -C_2$. In this regard, among the extrinsic energy terms the second term in Eq. (2.41) is relevant. It could be expressed as:

$$f_e^{(ext,2)} = \ k_e^{(2)}(q_1^2 + q_2^2)(C_1^2 + C_2^2). \tag{2.43}$$

In almost all theoretical studies (based on XY-type models) focusing on the coupling between curvature and TDs in the 2D manifold, the extrinsic terms were neglected [67]. Namely, in these studies, the elastic term was expressed using covariant derivatives. In such approaches, only the intrinsic contributions are present. However, recently it has been shown [52] that the extrinsic curvature might introduce quantitative and qualitative changes in behaviour. Moreover, this curvature is sensitive to how 2D manifold is embedded in $\mathbb{R}^3$ Cartesian space.

For scaling purposes, we introduce two charteristic quantities, namely the equilibrium scalar order parameter and the nematic correlation length. The former determines the bulk equilibrium value of the order parameter in flat geometries and expressed as [68]:

$$\lambda_b = \lambda_0 \ \sqrt{-\tau}, \tag{2.44}$$

where $\lambda_0 = \sqrt{a_0/2b}$ and $\tau = \frac{T - T_c}{T_c}$.

The nematic correlation length is defined as:

$$\xi = \frac{\xi_0}{\sqrt{|\tau|}}, \tag{2.45}$$

where ξ_0 characterises the typical core size of a TD [17].

We introduce the scaled order parameter as $\boldsymbol{Q} \to \boldsymbol{Q}/\lambda_0$, the scalled curvature tensor $\boldsymbol{C} \to R\boldsymbol{C}$ where R is a geometrically imposed length. The resulting dimensionless free energy density $f \to fR^2/k_i$ [25]. Thus, the dimensionless free-energy density reads as:

$$\begin{gathered} f = \tfrac{\kappa}{k_i}\big(Tr(\boldsymbol{C})\big)^2 + \lambda_0^2(-\,Tr(\boldsymbol{Q})^2 + \tfrac{1}{4}(Tr(\boldsymbol{Q})^2)^2 + Tr(\boldsymbol{\nabla}_s\boldsymbol{Q})^2) + \\ \tfrac{k_e^{(1)}}{k_i} Tr(\boldsymbol{Q}\boldsymbol{C}^2) + \tfrac{k_e^{(2)}}{k_i} Tr(\boldsymbol{Q}^2\boldsymbol{C}^2). \end{gathered} \tag{2.46}$$

2.1.2.1.1 Euler-Lagrange equations in 2D

Equilibrium textures of ordered nematic films are obtained by solving numerically the Euler- Lagrange equations. Taking into account the fact that the quantities q_1 and q_2 are

scalar functions of (u, v) coordinates the corresponding Euler- Lagrange equations for the free energy density are expressed as:

$$\frac{\partial}{\partial v}\left(\frac{\partial f}{\partial q_{1,v}}\right)+\frac{\partial}{\partial u}\left(\frac{\partial f}{\partial q_{1,u}}\right)-\frac{\partial f}{\partial q_1}=0, \tag{2.47}$$

$$\frac{\partial}{\partial v}\left(\frac{\partial f}{\partial q_{2,v}}\right)+\frac{\partial}{\partial u}\left(\frac{\partial f}{\partial q_{2,u}}\right)-\frac{\partial f}{\partial q_2}=0. \tag{2.48}$$

Here, $q_{1,i}$ and $q_{2,i}$ denote the partial derivative of q_1 and q_2 with respect to coordinate $i = (u, v)$. The Euler-Lagrange equations were solved numerically, using the standard over relaxation method [69].

2.1.2.2 Three-dimensional free energy

Let us consider that LC occupies a region $\mathcal{W}$ of the three-dimensional Euclidean space, with boundary $\partial\mathcal{W}$. The corresponding nematic LC free energy functional in terms of the nematic tensor order parameter can be written as [19]:

$$F=\iiint_{\mathcal{W}}(f_c+f_e+f_f)d^3\boldsymbol{r}+\iint_{\partial\mathcal{W}}f_s\,d^2\boldsymbol{r}, \tag{2.49}$$

where the condensation (f_c), elastic (f_e) an external field (f_f) free energy densities are expressed as [1,8,12]:

$$f_c=a_0(T-T_*)Tr(\boldsymbol{Q}^2)-\frac{b}{3}Tr(\boldsymbol{Q}^3)+\frac{c}{4}\left(Tr(\boldsymbol{Q}^2)\right)^2, \tag{2.50}$$

$$f_e=\frac{k_i}{2}|\boldsymbol{\nabla Q}|^2, \tag{2.51}$$

$$f_f=-\frac{\Delta\chi\boldsymbol{E}\cdot\boldsymbol{Q}\cdot\boldsymbol{E}}{2}. \tag{2.52}$$

Here, T_* is the supercooling temperature. The elastic term f_e penalizes the deviations from a spatially homogeneous ordering. For simplicity, we limit attention to the approximation of equal nematic constants [1, 8, 12] where a single positive elastic constant k_i represents the elasticity of the system. The f_f term reflects a presence of an external electric or magnetic ordering field: $\boldsymbol{E} = E\boldsymbol{e}$, where $\Delta\chi$ corresponds to LC field anisotropy constant. In case of positively anisotropic LCs, an orientational order tend to be aligned along $\boldsymbol{e}$.

We model conditions at the LC confining boundaries either by [70,71]:

$$f_s=\frac{w}{2}\boldsymbol{v}\cdot\boldsymbol{Qv}\ , \tag{2.53}$$

or

$$f_s=\frac{w}{2}Tr(\boldsymbol{Q}-\boldsymbol{Q}_s)^2, \tag{2.54}$$

where w stands for the positive anchoring constant, which measures the strength of surface imposed anchoring, $\boldsymbol{v}$ is the local confinement surface normal. The nematic ordering imposed by the confining substrate is described by $\boldsymbol{Q}_s$. The surface term given by Eq. (2.53) enforces for $w > 0$ ($w < 0$) degenerate tangential (homeotropic) anchoring. On the other hand the contribution in Eq. (2.54) is minimized for $\boldsymbol{Q} = \boldsymbol{Q}_s$. For example, let's assume that an uniaxial orientational ordering is enforced along the unit vector $\boldsymbol{e}_s$, then it leads to [19]:

$$\boldsymbol{Q}_s = S_s(\boldsymbol{e}_s \otimes \boldsymbol{e}_s - \tfrac{1}{3}\boldsymbol{I}), \tag{2.55}$$

where S_s describes the surface enforced degree of uniaxial ordering.

The tensor order parameter $\boldsymbol{Q}$ can be represented in its eigenframe as [1]: $\boldsymbol{Q} = \sum_{i=1}^{3} \lambda_i \boldsymbol{e}_i \otimes \boldsymbol{e}_i$, where $\boldsymbol{e}_i$ and λ_i are the eigenvectors and eigenvalues, respectively. In simulations, we study TDs either in the Cartesian coordinate system (x, y, z) or in the cylindrical coordinate system (r, ϑ, z). Their coordinate frames are determined by the unit vectors $\{\boldsymbol{e}_x, \boldsymbol{e}_y, \boldsymbol{e}_z\}$ and $\{\boldsymbol{e}_r, \boldsymbol{e}_\vartheta, \boldsymbol{e}_z\}$, respectively.

For the computational purpose we parametrize the $\boldsymbol{Q}$-tensor order parameter as [72,73]:

$$\boldsymbol{Q} = (q_3 + q_1)\boldsymbol{e}_x \otimes \boldsymbol{e}_x + (q_3 - q_1)\boldsymbol{e}_y \otimes \boldsymbol{e}_y + q_2(\boldsymbol{e}_x \otimes \boldsymbol{e}_y + \boldsymbol{e}_y \otimes \boldsymbol{e}_x) - 2q_3\boldsymbol{e}_z \otimes \boldsymbol{e}_z, \tag{2.56}$$

$$\boldsymbol{Q} = (q_3 + q_1)\boldsymbol{e}_r \otimes \boldsymbol{e}_r + (q_3 - q_1)\boldsymbol{e}_z \otimes \boldsymbol{e}_z + q_2(\boldsymbol{e}_r \otimes \boldsymbol{e}_z + \boldsymbol{e}_z \otimes \boldsymbol{e}_r) - 2q_3\boldsymbol{e}_\vartheta \otimes \boldsymbol{e}_\vartheta, \tag{2.57}$$

where q_1, q_2, q_3 are variational order parameters, functions of x and y.

In the parametrization performed in the Cartesian coordinate system, we set that $\boldsymbol{e}_3 = \boldsymbol{e}_z$ is always an eigenvector of $\boldsymbol{Q}$. This choice implies that the vectors $\{\boldsymbol{e}_1, \boldsymbol{e}_2\}$ are allowed to rotate within the $(\boldsymbol{e}_x, \boldsymbol{e}_y)$ plane [12]:

$$\boldsymbol{e}_1 = \cos\varphi\, \boldsymbol{e}_x + \sin\varphi\, \boldsymbol{e}_y, \tag{2.58}$$

$$\boldsymbol{e}_2 = -\sin\varphi\, \boldsymbol{e}_x + \cos\varphi\, \boldsymbol{e}_y, \tag{2.59}$$

$$\boldsymbol{e}_3 = \boldsymbol{e}_z. \tag{2.60}$$

On the other hand, in case of the cylindrical symmetry, we impose the following parametrization. $\boldsymbol{e}_\vartheta$ is set to be a eigenvector of $\boldsymbol{Q}$. The eigenvectors $\{\boldsymbol{e}_1, \boldsymbol{e}_3\}$ are allowed to rotate in the plane $(\boldsymbol{e}_r, \boldsymbol{e}_z)$ with the angle $\varphi \in [0, \pi)$ [74]:

$$\boldsymbol{e}_1 = \sin\varphi\, \boldsymbol{e}_r + \cos\varphi\, \boldsymbol{e}_z, \tag{2.61}$$

$$\boldsymbol{e}_2 = \boldsymbol{e}_\vartheta, \tag{2.62}$$

$$\boldsymbol{e}_3 = -\cos\varphi\, \boldsymbol{e}_r + \sin\varphi\, \boldsymbol{e}_z. \tag{2.63}$$

In terms of $\{q_1, q_2, q_3\}$ the three $\boldsymbol{Q}$ eigenvalues are expressed as: $s_1 = q_3 + \sqrt{q_1^2 + q_2^2}$, $s_2 = q_3 - \sqrt{q_1^2 + q_2^2}$, $s_2 = -2q_3$. The exchange [75] of eigenvalues $s_1 \leftrightarrow s_2$ is realized when $\sqrt{q_1^2 + q_2^2} = 0$. It can be shown from Eq. (2.55) that in the case of uniaxial

ordering (where we enforce $\boldsymbol{n} = \boldsymbol{e}_1$) it holds that $q_1 = S\cos(2\varphi)$, $q_2 = S\sin(2\varphi)$, $q_3 = S/6$.

In order to illustrate the topology of possible nematic textures we introduce the following alternative parametrization of the $\boldsymbol{Q}$ eigenvalues [73]:

$$\lambda_1 = \frac{2}{3}s\ \cos\psi, \tag{2.64}$$

$$\lambda_2 = -\frac{2}{3}s\ \cos\left(\psi - \frac{\pi}{3}\right), \tag{2.65}$$

$$\lambda_3 = -\frac{2}{3}s\ \cos\left(\psi + \frac{\pi}{3}\right), \tag{2.66}$$

where

$$s = \sqrt{\frac{3}{2}Tr(\boldsymbol{Q}^2)}\ . \tag{2.67}$$

Note that in case if elastic distortions exist nematic ordering is said to achieve some degree of biaxial ordering. The degree of biaxiality can be measured by the following quantity [76]:

$$\beta^2 = 1 - \frac{6(Tr(\boldsymbol{Q})^3)^2}{(Tr(\boldsymbol{Q})^2)^3}. \tag{2.68}$$

From Eq. (2.68) one can see that the case $\beta^2 = 0$ corresponds to the uniaxial configuration, whereas the maximum degree of biaxiality represents by $\beta^2 = 1$.

In Figure 2.1, the main feature of this parametrization with respect to the degree of biaxiality of unit TD is depicted. The case $s = 0$ corresponds to an isotropic or disordered state. Furthermore, the biaxiality measure can be determined by $\beta^2 = \sin^2(3\psi)$.Configurations $\{\psi = 0, \psi = \frac{2\pi}{3}, \psi = -\frac{2\pi}{3}\}$ correspond to uniaxial states with a positive scalar order parameter S and $\{\psi = \pi, \psi = -\frac{\pi}{3}, \psi = \frac{\pi}{3}\}$ to uniaxial states with a negative value of S for the nematic director aligned along $\boldsymbol{e}_1$, $\boldsymbol{e}_2$ and $\boldsymbol{e}_3$, respectively. The degree of biaxiality attains its maximum at the angles: $\psi = \pm\frac{\pi}{6}$, $\psi = \pm\frac{\pi}{2}$ and $\psi = \pm\frac{5\pi}{6}$ [12].

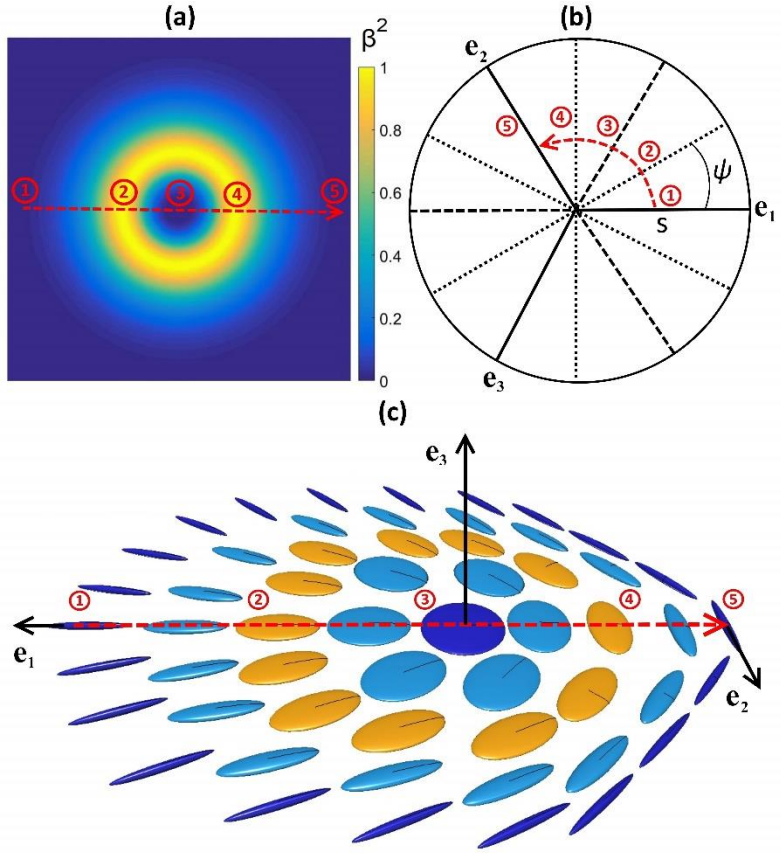

Figure 2.1: *Schematic representation of a biaxial core and possible configurations of the system in the phase space* $\{s, \psi\}$. (a): Top view of a characteristic degree of biaxiality $\beta^2(x, y)$ of an elementary unit $m_0 = 1/2$.The dashed red line depicted in the figure indicates a path from the state with positive uniaxiality (point ①) via states with a maximal degree of biaxiality (points ②, ④) and negative uniaxiality (point ③) to state with positive uniaxiality (point ⑤). The corresponding paths in the order parameter space $\{s, \psi\}$ and in superellipsoid shape space are shown in (Fig.0 (b)) and (Fig.0 (c)) respectively. (b): Nematic states in the phase space {s, ψ}. Solid line stands for positively uniaxial states $(S > 0)$; $\boldsymbol{n}(\psi = 0) = \boldsymbol{e}_1$, $\boldsymbol{n}(\psi = 2\pi/3) = \boldsymbol{e}_2$, $\boldsymbol{n}(\psi = -2\pi/3) = \boldsymbol{e}_3$. Dashed lines denote negatively uniaxial states $(S < 0)$; $\boldsymbol{n}(\psi = \pi) = \boldsymbol{e}_1$, $\boldsymbol{n}(\psi = -\pi/3) = \boldsymbol{e}_2$, $\boldsymbol{n}(\psi = \pi/3) = \boldsymbol{e}_3$. Dotted lines indicate the states with a maximal degree of biaxiality $\beta^2 = 1$. The trajectory shown in the $\{s, \psi\}$ space joining points ① and ⑤ for the equilibrium texture shown in Figure 2.1(a). A circle corresponds to the maximum value of the parameter $s = 1$. At the center of the circle, $s = 0$ and the phase is isotropic. (c): A biaxial core structure of $m_0 = \frac{1}{2}$ disclination with the color code of $\beta^2 \in$ [0,1].

For scaling purposes, we introduce the reduced temperature [73]:

$$\tau = \frac{24ac}{b^2} = \frac{T - T_*}{T_{**} - T_*}, \tag{2.69}$$

where T_{**} is the nematic *superheating* temperature. The corresponding superheating bulk nematic order parameter S_{**} is given by [12]:

$$S_{**} = \frac{b}{4c}. \tag{2.70}$$

In terms of these quantities, the equilibrium scalar order parameter corresponding to a global minimum in a bulk homogeneous uniaxial configuration exists for $\tau_{IN} \leq \frac{T_{IN}-T_*}{T_{**}-T_*} = \frac{8}{9}$ and can be expressed as [12]:

$$S_{eq}(\tau \leq \tau_{IN}) = S_{**}(1 + \sqrt{1-\tau}). \tag{2.71}$$

It is convenient to scale the nematic order parameter with respect to $S_{**} = S_{eq}(T_{**})$; therefore we introduce $\widetilde{\boldsymbol{Q}} = \boldsymbol{Q}/S_{**}$, $\widetilde{\boldsymbol{Q}}_s = \boldsymbol{Q}_s S/S_{**}$, $\tilde{q}_1 = q_1/S_{**}$, $\tilde{q}_2 = q_2/S_{**}$, $\tilde{q}_3 = q_3/S_{**}$, $\tilde{S}_s = S_s/S_{**}$.

An important role in our modeling is played by the biaxial order parameter correlation length ξ_b, which roughly estimates the linear core size of common TDs. Its size is estimated by [73]:

$$\xi_b = \sqrt{\frac{4k_i c}{b^2(\sqrt{1-\tau}+1)}} = \frac{\xi_b^{(0)}}{\sqrt{1+\sqrt{1-\tau}}}, \tag{2.72}$$

where $\xi_b^{(0)}$ is the temperature independent biaxial correlation length. The external field coherence length is expressed as $\xi_E \propto \sqrt{k_i S_{**}/(|\Delta\chi|E^2)}$ and the surface extrapolation length is given by $d \propto k_i S_{**}/w$. We further scale all lengths in units of h and introduce the following dimensionless quantities: $\widetilde{\boldsymbol{\nabla}} = h\boldsymbol{\nabla}$,$\tilde{F} = F/F_0$, where $F_0 = k_i/h^2$. We set $\boldsymbol{e}_s = \cos\varphi_s\, \boldsymbol{e}_x + \sin\varphi_s\, \boldsymbol{e}_y$, which leads to [12]:

$$\frac{1}{2}Tr(\boldsymbol{Q}-\boldsymbol{Q}_s)^2 = q_1^2 + q_2^2 + 3q_3^2 - q_3 S_s + \frac{S_s^2}{3} - S_s[q_1\cos(2\varphi_s) + q_2\sin(2\varphi_s)]. \tag{2.73}$$

By omitting the tildes we express $\{f_c, f_e, f_f, f_s\}$ the dimensionless free energy densities in the following way [12]:

$$f_c = A_e^2[\tfrac{\tau}{6}(q_1^2+q_2^2+3q_3^2) - 2q_3(q_1^2+q_2^2+q_3^2) + \tfrac{1}{4}(q_1^2+q_2^2+3q_3^2)^2], \tag{2.74}$$

$$f_e = |\nabla q_1|^2 + |\nabla q_2|^2 + 3|\nabla q_3|^2, \tag{2.75}$$

$$f_f = -A_f^2(q_1\cos(2\theta_f) + q_2\sin(2\theta_f) + q_3), \tag{2.76}$$

$$f_e = A_s Tr(\boldsymbol{Q}-\boldsymbol{Q}_s)^2, \tag{2.77}$$

where $A_e = h/\xi_b^{(0)}$, $A_f = h/\xi_E$ and $A_s = h^2 w/k_i$ are dimensionless quantities.

Since our aim is to study static and dynamic phenomena in frustrated nematic LCs, on par with static behaviour, we also consider the cases, in which the time evolution of nematic textures is described by using the following simple dynamics of model A [77]:

$$\frac{\partial \boldsymbol{Q}}{\partial t} = -\Gamma\frac{\delta F}{\delta \boldsymbol{Q}}, \tag{2.78}$$

where Γ stands for the kinetic coefficient assumed to be a constant [78]. In case of nematic LCs $\gamma = \Gamma^{-1}$ is a viscosity coefficient controlling the relaxation process [59]. The

appropriate time interval Δt is chosen as 10^{-6} (s). In case of rotational external field $\omega_f = \theta_f/\Delta t$. The corresponding scaling yields: $\tilde{\gamma} = \gamma S_{**}^2 a^2/t_0 k_i$, $t = \epsilon \Delta t$. It follows that:

$$\tilde{\gamma}\frac{\partial \widetilde{\boldsymbol{Q}}}{\partial \epsilon} = -\Gamma \frac{\delta \tilde{F}}{\delta \widetilde{\boldsymbol{Q}}}. \tag{2.79}$$

2.1.2.2.1 Euler-Lagrange equations in 3D

We use standard methods in the calculus of variations to compute Euler-Lagrange equations for extremal points of the Landau-de Gennes energy functional [78]. Minimization of the free energy for given boundary conditions yields the following bulk Euler-Lagrange equations for $q_1(x,y)$, $q_2(x,y)$, $q_3(x,y)$:

$$\left(\frac{\xi_b^{(0)}}{R}\right)^2 \Delta_\perp q_1 - \frac{\tau}{6} q_1 + 2 q_3 q_1 - \frac{q_1}{2}(3q_3^2 + q_1^2 + q_2^2) = 0, \tag{2.80}$$

$$\left(\frac{\xi_b^{(0)}}{R}\right)^2 \Delta_\perp q_2 - \frac{\tau}{6} q_2 + 2 q_2 q_3 - \frac{q_2}{2}(3q_3^2 + q_1^2 + q_2^2) = 0, \tag{2.81}$$

$$\left(\frac{\xi_b^{(0)}}{R}\right)^2 \Delta_\perp q_3 - \frac{\tau}{6} q_3 + \frac{1}{3}(q_1^2 + q_2^2 - 3q_3^2) 2 q_3 q_1 - \frac{q_3}{2}(3q_3^2 + q_1^2 + q_2^2) = 0, \tag{2.82}$$

where $\Delta_\perp = \frac{\partial^2}{\partial x^2} + \frac{\partial^2}{\partial y^2}$ is the Laplace operator in the Cartesian coordinate system, R is the characteristic size of the system.

On the other hand, in the case of $q_1(r,z)$, $q_2(r,z)$, $q_3(r,z)$ parametrization the free energy minimization request the following bulk Euler-Lagrange equations:

$$\left(\frac{\xi_b^{(0)}}{h}\right)^2 \left(\Delta q_1 - \frac{3q_1 + q_2}{r^2}\right) - \frac{\tau}{6} q_1 + \frac{1}{3}(q_2^2 + q_3^2 - 3q_1^2) - \frac{q_0}{2}(3q_1^2 + q_2^2 + q_3^2) = 0, \tag{2.83}$$

$$\left(\frac{\xi_b^{(0)}}{h}\right)^2 \left(\Delta q_2 - \frac{3q_1 + q_2}{r^2}\right) - \frac{\tau}{6} q_2 + 2 q_1 q_2 - \frac{q_2}{2}(3q_1^2 + q_2^2 + q_3^2) = 0, \tag{2.84}$$

$$\left(\frac{\xi_b^{(0)}}{h}\right)^2 \left(\Delta q_3 - \frac{q_3}{r^2}\right) - \frac{\tau}{6} q_3 + 2 q_1 q_3 - \frac{q_3}{2}(3q_1^2 + q_2^2 + q_3^2) = 0, \tag{2.85}$$

where $\Delta = \frac{\partial^2}{\partial r^2} + \frac{1}{r}\frac{\partial}{\partial r} + \frac{\partial^2}{\partial^2 z}$ is the Laplace operator in polar cylindric coordinates, h is the height of the cell. The equations are solved by a standard relaxation method for given boundary conditions [79].

2.1.2.2.2 Interaction with NPs

Our interest is also to study interactions between NPs and LC surrounding, in which NPs are immersed. We restrict our attention to a plane parallel hybrid cell exhibiting a cylindrical symmetry. NP is regarded to be cylindrically shaped and set at an arbitrary

position z at the symmetry axis of the cell. In order to elucidate its trapping capabilities, we introduce a force exhibiting on NP. For this purpose, we evaluate the Ericksen stress tensor $\boldsymbol{T}^{(E)}$ at LC-NP interface and the performing the following integration [80]:

$$F = \int \boldsymbol{T}^{(E)} \cdot \boldsymbol{v} d^2\boldsymbol{r}, \tag{2.86}$$

where $\boldsymbol{v}$ stands for a local outer unit normal vector. Moreover, in terms of the volume LC free energy the Ericksen stress tensor can be written as follows [79]:

$$\boldsymbol{T}^{(E)} = W\boldsymbol{I} - \boldsymbol{\nabla Q} \odot \frac{\partial f}{\partial \boldsymbol{\nabla Q}}. \tag{2.87}$$

For any pair of third-rank tensors, it holds:

$$(\boldsymbol{X} \odot \boldsymbol{Y})_{\boldsymbol{ij}} = \sum_{h,k} X_{hki} Y_{hkj}. \tag{2.88}$$

In the dimensionless form, using the parameterization described above, the tensor and force read as:

$$\tilde{\boldsymbol{T}}^{(E)} = \boldsymbol{T}^{(E)} \frac{(4C)^3}{B^4}, \tilde{F} = F \frac{(4C)^3}{h^2 B^4}. \tag{2.89}$$

Taking into account the fact that the transmitted force to the plate exhibits vanishing component along $\boldsymbol{v}$, which is an arbitrary vector in the $(\boldsymbol{e}_r, \boldsymbol{e}_\varphi)$ plane, we conclude that the transmitted force has a non-vanishing component along $\boldsymbol{e}_z$. According to this $\tilde{F}$ can be expressed as a sum of integrals run over the top, bottom and lateral surfaces of a NP:

$$\frac{\tilde{F}}{2\pi} = \int_{top} \boldsymbol{e}_z \cdot \boldsymbol{T}^{(E)} \boldsymbol{e}_z r \, dr - \int_{bottom} \boldsymbol{e}_z \cdot \boldsymbol{T}^{(E)} \boldsymbol{e}_z r \, dz + \int_{wall} \boldsymbol{e}_z \cdot \boldsymbol{T}^{(E)} \boldsymbol{e}_r r \, dz, \tag{2.90}$$

where the components $\boldsymbol{e}_z \cdot \boldsymbol{T}^{(E)} \, \boldsymbol{e}_z$ and $\boldsymbol{e}_z \cdot \boldsymbol{T}^{(E)} \, \boldsymbol{e}_r$ are given by:

$$\begin{aligned} \boldsymbol{e}_z \cdot \boldsymbol{T}^{(E)} \, \boldsymbol{e}_z = \xi_b^2 \Big(& 3(q_{0,r}^2 - q_{0,z}^2) + (q_{1,r}^2 - q_{1,z}^2) + (q_{2,r}^2 - q_{2,z}^2) + \\ & \frac{q_3^2 + (3q_0^2 - q_1^2)}{r^2} \Big) + \frac{\tau}{6}(3q_0^2 + q_1^2 + q_3^2) + 2q_0(q_0^2 - q_1^2 - q_3^2) + \frac{1}{4}(3q_0^2 + q_1^2 + q_3^2)^2, \end{aligned} \tag{2.91}$$

$$\boldsymbol{e}_z \cdot \boldsymbol{T}^{(E)} \, \boldsymbol{e}_r = -2\xi_b^2 (3q_{0,r}q_{0,z} + q_{1,r}q_{1,z} + q_{3,r}q_{3,z}). \tag{2.92}$$

2.2 Curvatures

In this Section, the basics of the differential geometry of surfaces are introduced. The mesoscopic Landau modeling is presented describing the interaction between nematic ordering and curvature. Internal and external curvature contributions are presented. In particular, the impact of the Gaussian curvature on position and number of topological defects is analysed.

We begin an analytical study of surfaces by introducing the standard parametrization of the surface $\boldsymbol{r}(u,v) = \big(x(u,v), y(u,v), z(u,v)\big)$, where the pair (u,v) denotes surface coordinates. Of our interest is to determine the basic intrinsic properties of a surface. For this purpose, we introduce the first fundamental form, which characterizes the internal geometry of the surface in the neighbourhood of a given point [80]:

$$I := d\boldsymbol{r}^2 = E(u,v)du^2 + 2F(u,v)dudv + G(u,v)dv^2, \tag{2.93}$$

where $E = \boldsymbol{r}_{,u} \cdot \boldsymbol{r}_{,u}$, $F = \boldsymbol{r}_{,u} \cdot \boldsymbol{r}_{,v}$, $G = \boldsymbol{r}_{,v} \cdot \boldsymbol{r}_{,v}$ are its coefficients. It can be regarded as the inner product of the tangent vectors. Furthermore, the second fundamental form is expressed as [81]:

$$II := (-d\boldsymbol{r} \cdot \boldsymbol{n}) = L(u,v)du^2 + 2M(u,v)dudv + N(u,v)dv^2, \tag{2.94}$$

where $L = \boldsymbol{r}_{,vv} \cdot \boldsymbol{n}$, $M = \boldsymbol{r}_{,uv} \cdot \boldsymbol{n}$, $N = \boldsymbol{r}_{,uu} \cdot \boldsymbol{n}$ are the coefficients of the second fundamental form, $\boldsymbol{n}$ denotes a unit normal vector. Here $\boldsymbol{r}_{,u} = \partial \boldsymbol{r}/\partial u$ and $\boldsymbol{r}_{,vv} = \partial^2 \boldsymbol{r}/\partial v^2$, $\boldsymbol{r}_{,uv} = \partial^2 \boldsymbol{r}/\partial u \partial v$, $\boldsymbol{r}_{,uu} = \partial^2 \boldsymbol{r}/\partial u^2$.

The first and second quadratic forms have two important joint scalar invariants with respect to the transformation of coordinates on the surface. More specifically, the ratio of the discriminants of these forms is equal to the Gaussian curvature K of a surface [82]:

$$K = \frac{LN - M^2}{EG - F^2} = \frac{\det(II)}{\det(I)}. \tag{2.95}$$

The extrinsic measure of the curvature, namely the Mean curvature H, is defined by:

$$H = \frac{EN + GL - 2FM}{2(EG - F^2)}. \tag{2.96}$$

Moreover, those two invariants could be rewritten in terms of principal curvatures. For this purpose, let us consider the Weingarten tensor $\boldsymbol{C}$ [63], representing the curvature tensor describing a local surface patch embedded in $\mathbb{R}^3$ space defined by Eq. (2.34).

The measure sheding light on how the surface is bended by a different amount in differencing directions at a given point is determined by two principal curvatures [83]:

$$C_{1,2} = \frac{EN + GL \mp \sqrt{(EN + GL)^2 - 4EG(LN - M^2)}}{2EG}. \tag{2.97}$$

One curvature determines the minimum bending, whereas the second one describes the maximum bending of the surface. They can also be expressed as $C_1 = \frac{1}{R_1}$, $C_2 = \frac{1}{R_2}$, where R_1 and R_2 are radii of circles that best fit the principal curvature at an arbitrary point. As a result, the key invariants can be rewritten in terms of the principal curvatures, namely as a trace and determinant of the curvature tensor $\boldsymbol{C}$. It follows:

$$H = \frac{1}{2}(C_1 + C_2) = \frac{Tr[C]}{2}, \tag{2.98}$$

$$K = C_1 C_2 = Det[C]. \tag{2.99}$$

Depending on values and signs of the principal curvatures, one can distinguish among different types of surfaces. In elliptic surfaces, the two principal curvatures are positive. In hyperbolic surfaces, the principal curvatures possess the same absolute value but are of different sign. Finally, in flat surfaces, the principal curvatures are equal to zero.

In order to demonstrate different impacts of the intrinsic and extrinsic curvatures on curved surface let us consider the simplest possible free energy density expression [84]:

$$f_e = k|\boldsymbol{\nabla}_s \boldsymbol{n}|^2, \tag{2.100}$$

where k is the positive elastic constant, $\boldsymbol{\nabla}_s = (\boldsymbol{I} - \boldsymbol{v} \otimes \boldsymbol{v})\boldsymbol{\nabla}$ is the surface gradient [17], $\boldsymbol{I}$ is the 3D identity tensor, $\boldsymbol{\nabla}$ is the covential 3D gradient operator, $\boldsymbol{v}$ is the surface normal.

The curvature tensor has diagonal form in the surface principal curvatures frame $(\boldsymbol{e}_1, \boldsymbol{e}_2)$. According to the Euler Curvature Formula [85] the normal curvature C, in a direction which is tilted with respect to the director first principal direction by an angle η, can be expressed as:

$$C = C_1 \cos^2 \eta + C_2 \sin^2 \eta. \tag{2.101}$$

Taking into account the expression of $\boldsymbol{n}$ in the same frame described in Eqs. (2.37 ,2.38) one can express:

$$\boldsymbol{\nabla}_s \boldsymbol{n} = \cos\eta\, \boldsymbol{\nabla}_s \boldsymbol{e}_1 - \sin\eta\, \boldsymbol{e}_1 \otimes \boldsymbol{\nabla}_s \eta + \sin\eta\, \nabla_s \boldsymbol{e}_2 + \cos\eta\, \boldsymbol{e}_2 \otimes \boldsymbol{\nabla}_s \eta. \tag{2.102}$$

Moreover, taking into relations [63]:

$$\boldsymbol{\nabla}_s \boldsymbol{e}_1 = \kappa_{q1} \boldsymbol{e}_2 \otimes \boldsymbol{e}_1 + \kappa_{q2} \boldsymbol{e}_2 \otimes \boldsymbol{e}_2 - C_1 \boldsymbol{v} \otimes \boldsymbol{e}_1, \tag{2.103}$$

$$\boldsymbol{\nabla}_s \boldsymbol{e}_2 = -\kappa_{q1} \boldsymbol{e}_1 \otimes \boldsymbol{e}_1 - \kappa_{q2} \boldsymbol{e}_1 \otimes \boldsymbol{e}_2 - C_2 \boldsymbol{v} \otimes \boldsymbol{e}_2, \tag{2.104}$$

where κ_{q1}, κ_{q2} are geodesic curvatures of the lines of principal curvatures C_1, C_2, we obtain [68]:

$$|\boldsymbol{\nabla}_s \boldsymbol{n}|^2 = |\boldsymbol{\nabla}_s \eta + \boldsymbol{A}|^2 + \boldsymbol{n} \cdot \boldsymbol{C}^2 \boldsymbol{n}, \tag{2.105}$$

where the quantity $\boldsymbol{A}$ is the so called spin connection [21]. It can also be expressed as:

$$\boldsymbol{A} = \kappa_{q1} \boldsymbol{e}_1 + \kappa_{q2} \boldsymbol{e}_2. \tag{2.106}$$

It is related with the Gaussian curvature via the expression

$$K = |\boldsymbol{\nabla} \times \boldsymbol{A}|. \tag{2.107}$$

Summarizing the above, the free energy density $f_e = f_e^{(int)} + f_e^{(ext)}$ could be rewritten in the following form:

$$f_e^{(int)} = k|\boldsymbol{\nabla}_s \eta + \boldsymbol{A}|^2, \tag{2.108}$$

$$f_e^{(ext)} = k\boldsymbol{n} \cdot \boldsymbol{C}^2 \boldsymbol{n} = k(C_1^2 \cos^2 \eta + C_2^2 \sin^2 \eta). \tag{2.109}$$

The contribution defined by Eq. (2.108) can be thought of as the intrinsic term, whereas the contribution depicted in Eq. (2.109) describes the extrinsic impact.

If $K = 0$ a homogenous orientational ordering is imposed by the intrinsic term. On the other hand, in cases where surface patches exhibit nonzero Gaussian curvature, a geometric frustration is introduced. It descends from the fact that there is incompatibility of parallel and straight directions on the surface with nonzero Gaussian curvature. Hence, spatially nonhomogeneous ordering leads to minimizing of $f_e^{(int)}$. Expressing elastic free energy contributions by means of the covariant derivative approach gives only intrinsic-type contributions. More precisely, the covariant derivative is determined by the parallel transport. For instance, if the covariant derivative of $\boldsymbol{n}$ is equal to zero, the vector is said to be parallel transported. Mathematically, this is expressed as [63]:

$$\boldsymbol{\nabla}_s \boldsymbol{n} = -(\mathbf{v} \otimes \boldsymbol{\nabla}_s \mathbf{v})\boldsymbol{n}. \tag{2.110}$$

The parallel transport condition yields:

$$\boldsymbol{\nabla}_s \eta = -\boldsymbol{A} = -\kappa_{q1}\boldsymbol{e}_1 + \kappa_{q2}\boldsymbol{e}_2. \tag{2.111}$$

Consequently, $f_e^{(int)}$ is minimized if $\boldsymbol{n}$ is parallel transported. Configurations satisfying this condition display a local orientational structure with minimal possible elastic free energy distortions.

The extrinsic term can be regarded as an effective external field tending to align the $\boldsymbol{n}$ along the principal directions. Pushing this analogy further, one can find that extrinsic term is akin to the energy term typically used to study biological membranes [87] consisting of thin plates with anisotropic properties [88, 89]:

$$f_H = \frac{K_1}{2}(Tr\boldsymbol{M})^2 + K_2 Det\boldsymbol{M}, \tag{2.112}$$

where K_1 and K_2 are the positive constants. The tensor $\boldsymbol{M}$ characterizes the mismatch between the intrinsic curvature of inclusion and the local membrane curvature. It is defined as: $\boldsymbol{M} = \boldsymbol{R}_{tot}\boldsymbol{C}_m\boldsymbol{R}_{tot}^{-1} - \boldsymbol{C}$, where $\boldsymbol{R}_{tot}$ is the rotational matrix, which identify the rotation of the system by angle η, $\boldsymbol{C}_m$ is the intrinsic curvature of the inclusion. The f_H as well as $f_e^{(ext)}$ term attains its minimum value provided that the non-curved rod-like molecule is aligned along the principal direction exhibiting lower curvature [69].

Summarizing, the intrinsic elastic term fingerprints the variations of $\boldsymbol{n}$ within a 2D curved space. Contrary, the extrinsic contribution indicates how $\boldsymbol{n}$ is embedded in 3D space [69].

2.2.1 Geometrical theorems

In this Subsection, a brief overview of key theorems, which link differential geometry and topology and a creation of TDs is presented. Afterwards, the effective topological charge cancellation neutralization mechanism is discussed.

2.2.1.1 Gauss-Bonnet and Poincaré-Hopf theorems

The Gauss-Bonnet theorem establishes a deep link between two areas: topology and differential geometry. It is of high importance for the reason that it helps us to understand how geometrical information of a surface joins with a purely topological characteristic. The theorem relates curvature with angles characterizing a surface patch [90] and can be expressed as:

$$\alpha + \beta + \gamma = \pi + \iint_{\zeta} K \, d^2\boldsymbol{r}. \tag{2.113}$$

Here α, β, γ are the inner angles of the geodesic triangle on the surface, $d^2\boldsymbol{r} = \sqrt{EG - F^2}\, dx\, dy$ stands for the surface area, where E, G, F are the coefficients of the first fundamental form. From the Eq. (2.113) it follows, e.g., that in a case a pheudosphere the sum of inner angles of the geodesic triangle on it is less than π, whereas for a sphere the sum is larger than π. One can see that the Gaussian curvature plays the role of an intrinsic measure of the curvature of a surface at a point.

The Poincaré-Hopf theorem bridges the gap between two seemingly unrelated areas of mathematics. This theorem states that under reasonable conditions the sum of the indices of a vector field on a smooth compact oriented boundaryless manifold equals the Euler

characteristic of the manifold [93]. The Euler characteristic χ of a surface ζ is defined as [94]:

$$\chi = \frac{1}{2\pi}\iint_{\zeta} K\, d^2\boldsymbol{r} = V_i - E_i + F_i, \tag{2.114}$$

where V_i is the number of polyhedron vertices, F_i is the number of faces, E_i is the number of polyhedron edges of a given triangulation of ζ. The Euler characteristic is expressed as $\chi = 2(1-g)$. The integer g (the genus of the surface) indicates the number of "handles" that the surface contains.

Let us consider the surface covered by liquid crystal. In this case, one can observe frustrations in the orientational ordering of LCs. That is, the incompatibility of straight and parallel directions surface is given by entails geometrically induced stresses [25, 62]. To screen these stresses, defects are formed. An intrinsic measure of a shell is the Gaussian curvature. If a surface is deformed, then the Gaussian curvature can be changed pointwise. Consequently, a local Gaussian curvature has strong impacts on the position of TDs on the surface. TDs with positive (negative) topological charge localize to regions of positive (negative) Gaussian curvature.

Therefore, the number of TDs strongly depends on the topology of the hosting surface. According to the Poincaré-Brouwer theorem [21, 94], the total winding number of TDs within a closed surface is given by:

$$m_{tot} = \textstyle\sum_i m_i = \chi. \tag{2.115}$$

If a surface is deformed, its Euler characteristic does not change. Consequently, m_{tot} is a topological invariant. For instance, the spherical topology is characterized by $g = 0$, and it requests $m_{tot} = 2$.

2.2.1.2 Effective Topological Charge Cancelation Mechanism

Let us consider a closed surface with the Gaussian curvature varying from a point to point. If one splits such a surface into the surface patches, then each of these patches could exhibit significantly different average Gaussian curvature. We assign to each such patch $\Delta\zeta$ the average Gaussian curvature [69]:

$$\overline{K} = \frac{1}{\Delta\zeta}\iint_{\Delta\zeta} K\, d^2\boldsymbol{r}. \tag{2.116}$$

Within each patch we introduce an effective topological charge [69]:

$$\Delta m_{eff} = \Delta m + \Delta m_{\mathrm{V}} + \Delta m_K, \tag{2.117}$$

where Δm, Δm_{V}, and Δm_K refers to "real", "virtual" and "spread curvature" topological charge, respectively.

A "real" topological charge determines the total topological charge of existing TDs (exhibiting singularity in the director field distribution in the center of TD's core). A "virtual" TD could be viewed as an "impurity" (e.g. a μm or a nanosized particle) [2], which can produce the same director profile as a defect bearing topological charge $m = \Delta m_V$. A spread topological charge could be effectively regarded as a local surface region exhibiting either positive or negative Gaussian curvature K and is defined as [67, 69, 95]:

$$m_{tot} = \frac{1}{2\pi}\iint_{\zeta} K\, d^2\boldsymbol{r}, \tag{2.118}$$

and it holds:

$$m_{tot}(\zeta) - \frac{1}{2\pi}\iint_{\zeta} K\, d^2\boldsymbol{r} = \Delta m(\zeta) + \Delta m_V(\zeta) + \Delta m_K(\zeta) = 0. \tag{2.119}$$

In the case of closed patches, the effective topological charge cancellation mechanism (ETCC) neutralization mechanism is strictly realised. From Eq. (2.119) it follows that ordered shells unavoidably contain "real" or "virtual" TDs in case of non-toroidal geometries [2]. Furthermore, the number of TDs are characterized by the intrinsic curvature. For instance, in the case of the topology of a sphere, it follows $m_{tot} = 2$, whereas for a catenoid it holds $m_{tot} = -2$. Consequently, on the surface of a sphere (catenoid), one expects either four defects with the topological charge $m = 1/2$ ($m = -1/2$) or two defects bearing $m = 1$ ($m = -1$), or one defect with $m = 2$ ($m = -2$).

There are several works that demonstrated the electrostatic analogy where Gaussian curvature K plays the role of an electric field and topological charges m play the role of electric charges [69, 68, 95]. For example, the topological charge of an isolated TD is conserved. Furthermore, two defects (antidefects) repel each other, while defect and antidefects attract each other [64]. A surface region exhibiting positive (negative) Gaussian curvature is mathematically equivalent to a smeared negative (positive) charged. Although for the toroidal topology it holds $m_{tot} = 0$, it has been demonstrated that curvatures, to which inherent coexistence of regions exhibiting both $K > 0$ and $K < 0$ could trigger the unbinding of pairs (defect, antidefect) [64, 69, 68, 95, 96].

Several recent studies in LCs reveal strong interactions between TDs and nanoparticles (NPs) [32, 33, 95, 97, 98, 99, 100]. In this context, one must distinguish two different situations when NPs do not interact with the nematic director field exhibiting TDs and when they interact strongly. In the former case, NPs tend to assemble within cores of TDs [69], whereas in the latter they could effectively act as a topological charge [95, 100], which in turn leads to changing the total topological charge in the system.

2.2.2 Surfaces with the negative Gaussian curvature

In this Subsection, two surfaces of revolution with negative Gaussian curvature, namely the catenoid and the pseudosphere, are presented. A detailed analysis of their intrinsic characteristics is given. Based on it we can estimate localization of TDs location in ground state configurations.

2.2.2.1 Catenoid

The surface that locally minimizes its area is called to be minimal. In general, the surfaces that locally minimize surface area manifest themselves in various physical phenomena, including soap films, black holes, compound polymers, protein folding [102]. In particular, from the point of view of biological membranes, local neck-like regions with in-plane ordering can be well modelled by catenoid geometries [103]. Such membranes could be mathematically treated as effectively 2D films described in terms of the tensor nematic order parameter field and curvature fields.

The first, who showed mathematically that the catenoid is a minimal surface, was Leonard Euler [103]. Later, the physical interpretation of that surface was given by Plateau, providing experiments with soapy water and glycerin. A catenoid type of surface can be created by rotating a catenary curve when it is placed at a certain distance from its directrix. It is axially symmetric, enclosed surface bounded between the parallel circles of the same radius.

In order to elucidate its main properties let us consider the following parametrization:

$$\begin{cases} x = a\cosh\dfrac{v}{a}\cos u, \\ y = a\cosh\dfrac{v}{a}\sin u, \\ z = v. \end{cases} \tag{2.120}$$

In the Cartesian coordinates $(\boldsymbol{e}_x, \boldsymbol{e}_y, \boldsymbol{e}_z)$ the position vector of a generic point on an axisymmetric surface is determined by [69,104]:

$$\boldsymbol{r} = \rho(v)\cos(u)\boldsymbol{e}_x + \rho(v)\sin(u)\boldsymbol{e}_y + z(v)\boldsymbol{e}_z. \tag{2.121}$$

Here $\rho(v)$ and $z(v)$ are variation parameters defining the profile curve in the (x, z)-plane, v stands for the arc length of the profile curve, and u is the azimuthal angle, where $\in [-\pi, \pi)$, $v \in \mathbb{R}$, a is the neck radius. The catenoid shapes are defined by:

$$\rho(v) = a\cosh v/a\,,\ \ z(v) = v. \tag{2.122}$$

The infinitesimal element of distance within the surface can be expressed as:

$$ds^2 = \cosh^2(\tfrac{v}{a})(du^2 + a^2dv^2). \tag{2.123}$$

Its principal curvatures are given by:

$$C_1 = -C_2 = \frac{1}{a(\cosh\frac{v}{a})^2}. \tag{2.124}$$

The Gausssian curvature is expressed as:

$$K = -\frac{1}{a^2(\cosh\frac{v}{a})^4}. \tag{2.125}$$

As it can be seen from Eq. (2.124) that the Mean curvature is equal to zero:

$$H = 0. \tag{2.126}$$

The surface is said to be minimal if its Mean cuvature equals to zero. Figure 2.2. provides a conceptual illustration of the intrinsic characteristic inherent to catenoid geometry.

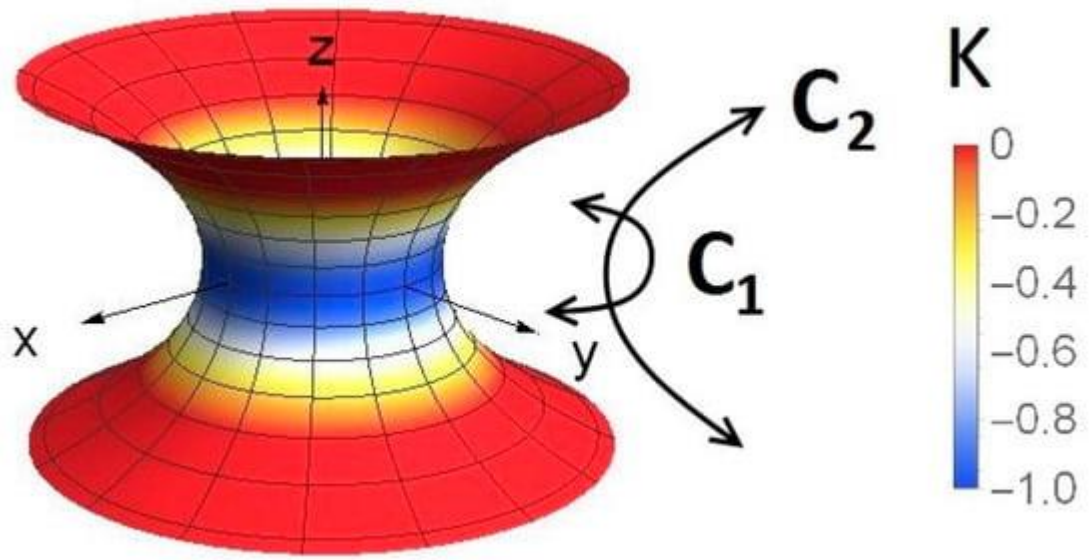

Figure 2.2: *Schematic representation of a catenoid in the Cartesian coordinate system.* Meridians and parallels on the catenoid are described by $u = const$ and $v = const$, respectively, where the (u, v) parametrization is defined in Eqs. (2.121, 2.122). Color determines the Gaussian curvature K. The mean curvature H is zero everywhere on the surface. The arrows indicate the principal directions of $\boldsymbol{C}$.

Among above-mentioned properties, this structure is also of interest due to the fact that the integral of the Gaussian curvature over the catenoid's surface is constant ($\frac{1}{2\pi}\iint K d^2\boldsymbol{r} = -2$). Therefore, in the view of the ETCC mechanism, the catenoid's surface enforces the smeared Gaussian curvature charge $\Delta m_K = -2$, so TDs bearing the total charge $\Delta m = -2$ should be introduced in order to make the nematic patch neutral ($\Delta m_{eff} = 0$) [25].

2.2.2.2 Pseudosphere

In comparison with the above-mentioned surface, the pseudosphere is the constant negative-Gaussian curvature surface of revolution. It is formed by rotating a curve (tractrix) about its asymptote. The name emphasizes the differences with the sphere, which is an example of a surface with the Gaussian curvature, also constant, but positive. It was firstly introduced by Beltrami [105]. The interest in the study of the pseudosphere is due to the fact that the figures drawn on the smooth parts of this surface obey the laws of non-Euclidean geometry. For instance, it can describe carbon-based energetically stable molecular structure [106]. Its parametric form is:

$$\begin{cases} x = a\,\mathrm{sech}\, v \cos u, \\ y = a\,\mathrm{sech}\, v \sin u, \\ z = av - a\tanh v\,, \end{cases} \tag{2.127}$$

where the pseudoshpere shapes are characterized by $\rho(v) = a\,\mathrm{sech}\, v$ and $z(v) = av - a\tanh v$, $u \in [0,2\pi)$, $v \in \mathbb{R}$, a is the radius of pseudosphere.

The surface area element is:

$$ds^2 = a^2\,\mathrm{ctg}^2\, v\;\; dv^2 + a^2 \sin^2 v\, du^2. \tag{2.128}$$

The principal curvatures are expressed as:

$$C_1 = -\frac{1}{a}\operatorname{csch}(v)\,, C_2 = \frac{1}{a}\sinh(v). \tag{2.129}$$

The Gaussian and mean curvatures are:

$$K = -\frac{1}{a^2}, \tag{2.130}$$

$$H = \frac{1}{2a}(\sinh v - \operatorname{csch} v). \tag{2.131}$$

Figure 2.3. schematically represents the differencial geometry quantities of the pseudosphere.

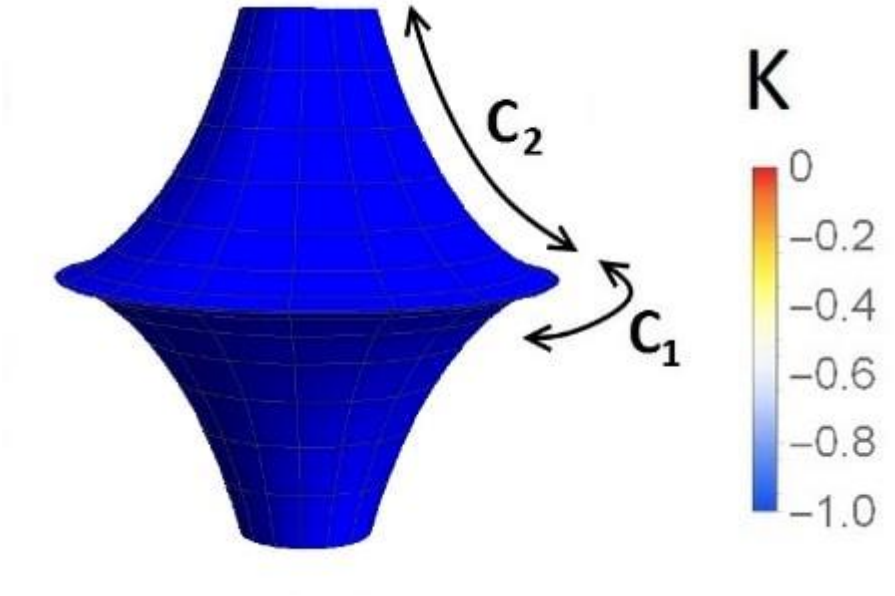

Figure 2.3: *Schematic representation of a pseudosphere in the Cartesian coordinate system.* The surface is colored by a function of the Gaussian curvature K, which is constant, negative everywhere on the surface. The principal curvatures $\{C_1, C_2\}$ are shown as black arrows, which represents corresponding principal directions.

The principal curvatures from Eq. (2.129) indicate the stretching at the horizon and the contradiction at the tip. The Hilbert theorem [107] states that the equator of this surface (the maximal circle with radius $a = a_{max}$) exhibits a singularity at $v = 0$. Consequently, the additional impact into the Gauss–Bonnet and Poincaré-Hopf theorem of the geodesic curvature k_g of the boundary must be suggested: $2\pi\chi = K + \int_{\partial\zeta} k_g\, d\zeta$. Singularities arise because the hyperbolic plane cannot be immersed completely into $\mathbb{R}^3$ [108]. Characteristically, they are cuspidal edges. At the cusp point, the surface converging towards the horizontal plane, which is called the Hilbert horizon [29]. Therefore, an unavoidable singular boundary dictates that TDs in the ground state to be located at the tip of the surface in the absence of an extrinsic curvature.

2.3 Topological Defects

This Section is dedicated to the description of the key characteristics of the topological defects in the nematic liquid crystals in 2D and 3D.

TDs appear in diverse physical fields and span different areas of physics such as biological structures [20, 109], solid crystals [110], liquid crystals [111, 112], flat nanomagnets [113, 114], ferromagnets [115, 116], cosmology [117] and other. For example, the first dynamical of TDs was developed by Kibble in 1976 [118] in order to explain the coarsening dynamics of TDs in the early universe.

In recent years, there is growing confidence that fields might represent a fundamental entity of nature instead of particles [5]. If so, TDs could be regarded as adequate candidates for this role. In fact, it was demonstrated for the first time by Skyrme in 1962 [4]. He proposed the theory in which solitons in the pion field represents mesons.

NLCs represent an adequate testing template for studying fundamental physics of TDs: firstly, due to their ability to exhibit a large variety of different phases and configurations; secondly, because of their inherent and unique combination of softness, fluidity, solidness and an optical anisotropy [119]. In general, TDs can emerge in LCs due to either topological, dynamics or energetic reasons. In addition, TDs in LC phases could be used as efficient traps for appropriate nanoparticles [120], which might pave the way to diverse applications in emerging nanotechnology.

Point and line defects in nematic LCs refer to localized regions where the nematic director field is not uniquely defined. Term disclination line is used for line defects along which the symmetry of rotation is broken [1]. There are two types of disclination lines: twist disclination lines (TDL) and wedge disclination lines (WDL). The formers are described by the director field surrounding TDL, which changes by bend and splay; the latter refers to singular lines around which the director field changes predominantly via twist elastic deformation. TDL exhibit 3D spatial variations, as opposed to WDL, which display 2D spatial variations. Line and point defects can be classified using Franks indices (i.e., winding numbers) and topological charges. The defect lines in the form of loops are topologically equivalent to point defects because they can be continuously transformed from one to another [1]. The characteristic linear core size of the TD is well estimated by the nematic correlation length ξ. The cores of defects typically exhibit biaxial or isotropic ordering.

In order to calculate the topological charge, we need first to introduce the order parameter space. It consists of all possible ground states of the *gauge field* component of the relevant order parameter. For example, in the case of the 3D ferromagnet, it is described by the vector order parameter $\boldsymbol{Q} = \lambda \boldsymbol{n}$, where λ stands for the *amplitude field* and $\boldsymbol{n}$ for the *gauge field.* The corresponding order parameter space forms a unit sphere. In 2D, the order parameter space is a circle. The topological charge of a TD in a general unit vector field $\boldsymbol{n} = n_1\boldsymbol{e}_1 + n_2\boldsymbol{e}_2 + \cdots + n_d\boldsymbol{e}_d$ (i.e.,$|\boldsymbol{n}| = 1$) in a d-dimensional coordinate frame $\{\boldsymbol{e}_1, \boldsymbol{e}_2, \ldots, \boldsymbol{e}_d\}$ is defined by an integral over a surface enclosing a defect [64]:

$$q = \frac{1}{\Omega} \iint \cdots \int Det \begin{vmatrix} n_1 & n_2 & \cdots & n_d \\ \frac{\partial n_1}{\partial u_1} & \frac{\partial n_2}{\partial u_1} & \cdots & \frac{\partial n_d}{\partial u_1} \\ \cdots & \cdots & \cdots & \cdots \\ \frac{\partial n_1}{\partial u_{d-1}} & \frac{\partial n_2}{\partial u_{d-1}} & \cdots & \frac{\partial n_d}{\partial u_1} \end{vmatrix} du_1\, du_2 \cdots du_{d-1}. \tag{2.132}$$

The coordinates $\{u_1, u_2, \ldots, u_{d-1}\}$ determine a *d-1* dimensional surface enclosing a defect, and Ω determines the "solid" angle in d-dimensional space (e.g., in 2D and 3D it equals to $\Omega = 2\pi$ and $\Omega = 4\pi$, respectively). The integral in Eq. (2.132) reveals how many

times all possible configurations of order parameter space are realized in the enclosed region. If this integral is zero, the region cannot contain a single defect (it can contain several defects if the sum of their topological charges equals to zero) [64].

The most remarkable properties of topological charges are the following:

1) They can possess only discrete values [64].

2) The topological charge is a conserved quantity, which leads to a conservation law that is analogous to the law of conservation of electric charges. If boundary conditions are fixed the topological charge conservation rule dictates possible scenario of decomposition, annihilation, and merging of TDs.

3) Pairs $\{q,\text{-}q\}$ are able to annihilate into a defectless state (i.e. in these cases total topological charge equals to zero) [64].

In case of a 2D space, one can use the parametrization $\boldsymbol{n} = n_1\boldsymbol{e}_1 + n_2\boldsymbol{e}_2 = \cos\Theta\,\boldsymbol{e}_1 + \sin\Theta\,\boldsymbol{e}_2$. In this case, Eq. (2.132) yields [64]:

$$q \equiv m = \frac{1}{2\pi}\int Det\begin{vmatrix} n_1 & n_2 \\ \frac{\partial n_1}{\partial u} & \frac{\partial n_2}{\partial u} \end{vmatrix} du = \frac{1}{2\pi}\int \frac{\partial\Theta}{\partial u}\,du = \frac{\Delta\Theta}{2\pi}, \tag{2.133}$$

where the du determines a differential along a closed line enclosing a defect counter clockwise, and $\Delta\Theta$ is the change of the angle Θ on encircling the defect. In 2D one referees to q also as the winding number m. For a vector field, a TD is characterized by an integer value of m, *i.e.* $m \in \{\pm1, \pm2, \pm3, \dots\}$ [64]. A sign is attached to such a winding number, which is positive if $\boldsymbol{n}$ winds in the same sense as the position vector that describes the circuit, and negative otherwise [68]. The defects bearing opposite value of m are commonly referred to as the defects ($m > 0$) and antidefects ($m < 0$) [25]. The head-to-tail symmetry of the unit vector $\pm\boldsymbol{n}$ dictates to winding number takes on the half-integer values, i.e., $m = \pm\frac{1}{2}, \pm\frac{3}{2}, \dots$. Some typical examples of TDs in 3D and 2D are schematically present on Figure 2.4.

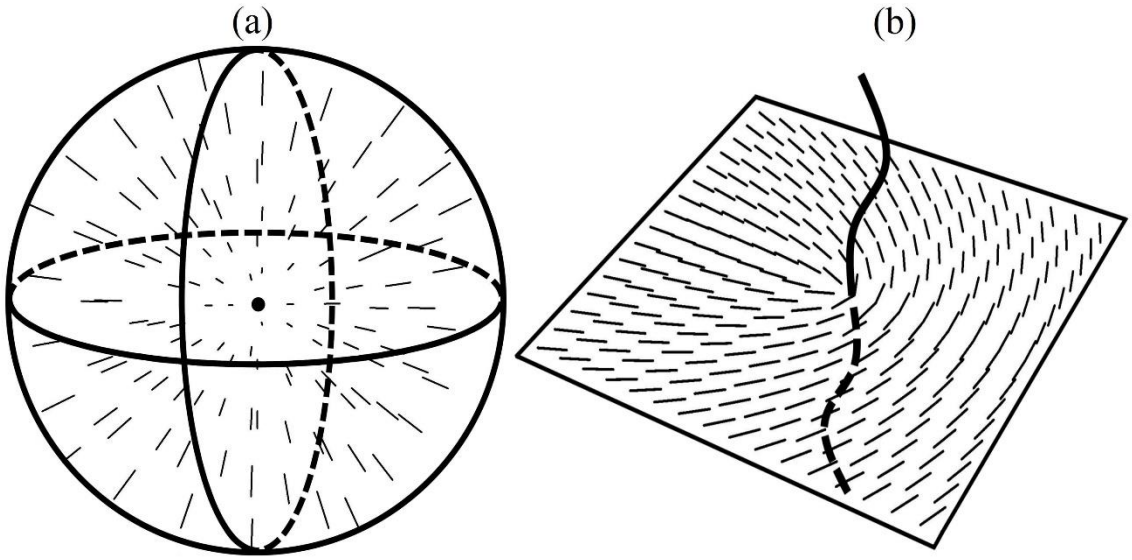

Figure 2.4: *Schematic presentation of (a) the texture of a topological point defect with charge* $q = 1$ *and (b) the cross-section of a disclination line with winding number* $m = 1/2$. The spatial distribution of the director field is indicated by the dashed curves.

Let us consider a planar plane. WDL could be well estimated by the model introduced by Frank, using the one-constant elastic free energy assumption: $K_{11} = K_{33} = K$. The director field can be expressed as:

$$\boldsymbol{n} = (\cos\Theta(x,y), \sin\Theta(x,y), 0), \tag{2.134}$$

where the planar angle Θ is a function of Cartesian coordinates. The minimization of the elastic part of the free energy $F_e = \int f_e dxdy$ gives the following Euler-Lagrange equation:

$$\frac{\partial^2\Theta}{\partial x^2} + \frac{\partial^2\Theta}{\partial y^2} = 0. \tag{2.135}$$

A possible solution can be expressed as:

$$\Theta(x,y) = m\ tan^{-1}\left(\frac{y-y_i}{x-x_i}\right) + \Theta_0 = m\varphi + \Theta_0, \tag{2.136}$$

where m is the winding number, Θ_0 is a constant and the coordinates (x_i, y_i) set the origin of a defect. The condition $\Theta(\varphi = 2\pi) = \Theta(\varphi = 0) + N\pi$ (where N is an integer) leads to discrete numbers $m \in \{0, \pm 1/2, \pm 1, \pm 3/2, \pm 2, ...\}$. If $m = 0$ the structure is said to be homogeneous, i.e. determined only by Θ_0. The director field configuration for TDs with different topological charges is shown in Figure 2.5.

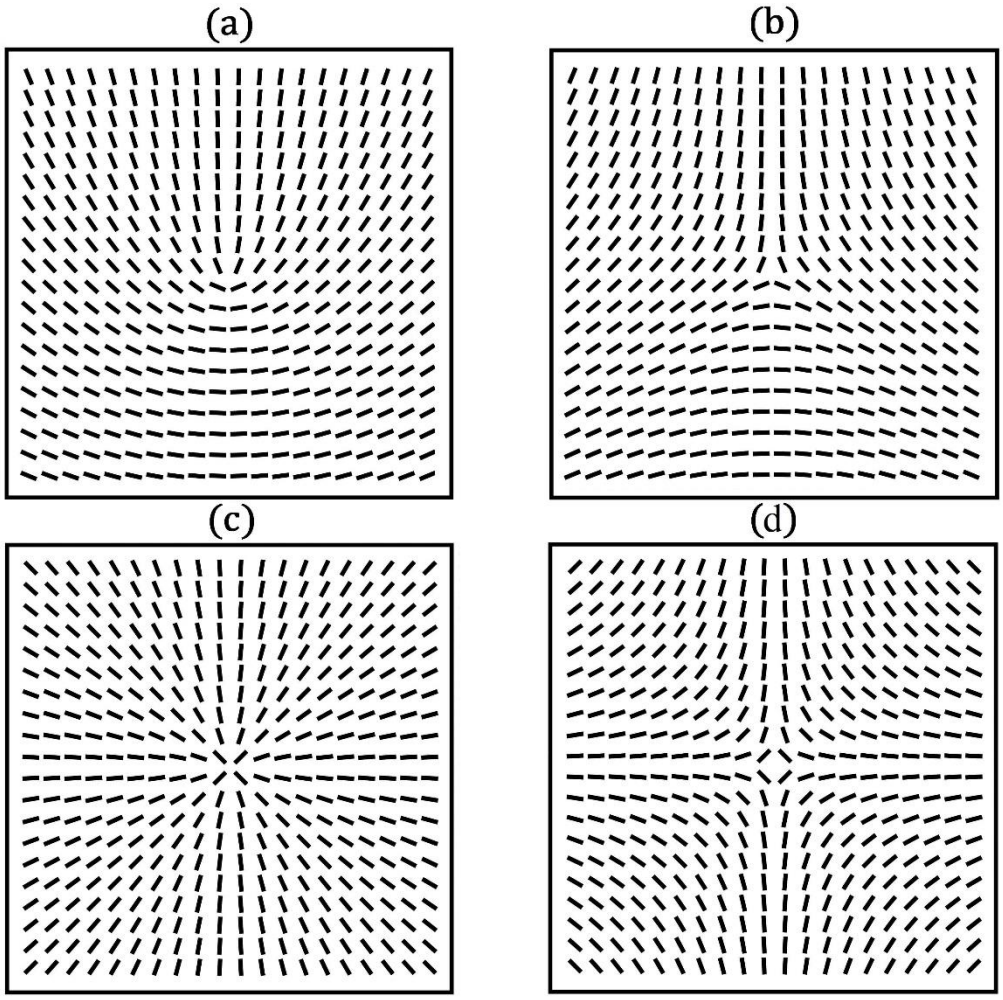

Figure 2.5: *Schematic presentation of topological defects in two dimensions with different topological charges: (a)* $m = 1/2$*,(b)* $m = -1/2$*, (c)* $m = 1$*, (d)* $m = -1$. At the origin of a defect, the director field fails to be defined.

By using Eqs. (2.134) and (2.135) the free energy volume density can be rewritten into:

$$f_e = \frac{1}{2} K (\nabla \Theta)^2. \tag{2.137}$$

By integrating Eq. (2.137) over the distortion and using singular solution Eq. (2.136) we get the elastic free energy per unit length of an isolated defect:

$$F = \pi K_0 m^2 ln \frac{R}{\rho} + F_0, \tag{2.138}$$

where R indicates the size of the system, F_0 is core free energy per unit length of line and ρ is the radius of the melted core.

From the results, we infer two important conclusions. Firstly, the elastic free energy penalty diverges in the limit $R \to \infty$, signalling that a single defect can not exist. Secondly, if we have several defects in a finite volume, from a relatively large distance they effectively act as a single defect bearing an effective charge. It follows that in an infinite system the total charge of TDs must be zero [64].

One can see that the proportionality to m^2 in Eq. (2.138) implies that it is energetically advantageous for a system that TDs exhibiting large topological charge decompose into several TDs with smaller charges. Therefore, the TD with integer strength ($m^2 = 1$) will split into two half-integer strength defects ($m_0 = \frac{1}{2}$), it entails that $\Delta F \sim \frac{1}{4} + \frac{1}{4} = \frac{1}{2}$.

Chapter 3

Results

3.1 Tumbling

Of our interest are qualitative changes in time behavior of the average nematic configuration on a varying amplitude B_0 of the field $\boldsymbol{B}$, the rotation periodicity t_0 and the anchoring strength. In particular, we are interested in phenomena triggered by the dual axis anchoring condition. In simulations, we typically consider systems with $M \times N \times L = 90 \times 90 \times 10$ and $\gamma = 2$ deep in the nematic phase. We study dynamical structural response of the system on varying model parameters, where we use Brownian molecular dynamics. At the lateral sites of the system, we impose the periodic boundary condition.

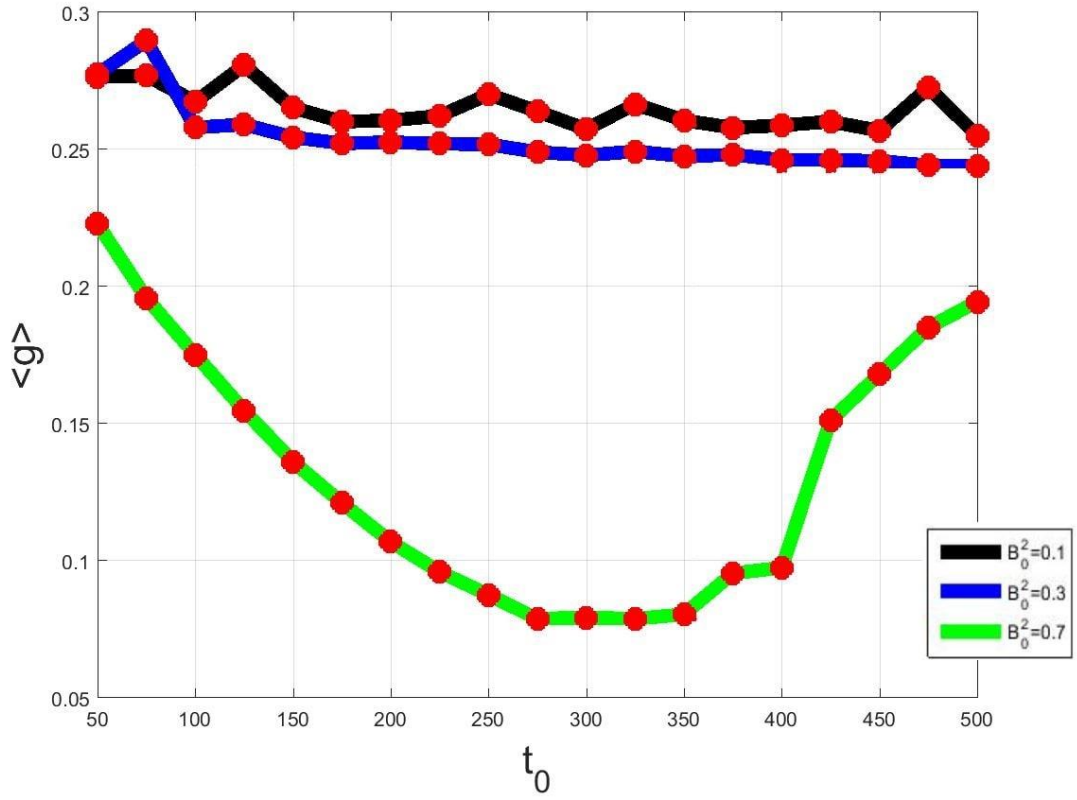

Figure 3.1: *Plot of* $\langle g \rangle$ *versus* t_0*, for different values of* B_0*:* $B_0^2 = 0.1$ *,* $B_0^2 = 0.3$*,* $B_0^2 = 0.7$.

Our systematic study shows that the quantity $\langle g \rangle$ (see Eq. (2.31)) reveals regime exhibiting maximal complexity, as demonstrated in Figure 3.1. It turns out to appear for a sufficiently large value of the amplitude B_0. In the case if, it is too low, relatively large fluctuations dominate in $\langle g(t_0) \rangle$ dependence (depicted by the black and blue solid lines in Figure 3.1) and qualitatively similar behavior in the whole interval of studied values of t_0. On the other hand, for large enough values of B_0 one could observe a "u-type" $\langle g(t_0) \rangle$ dependence, which is illustrated by the green solid line in Figure 3.1. Such dependence fingerprints complex $\boldsymbol{S}_\alpha(t)$ behavior on varying t_0, which is shown in Figure 3.2.

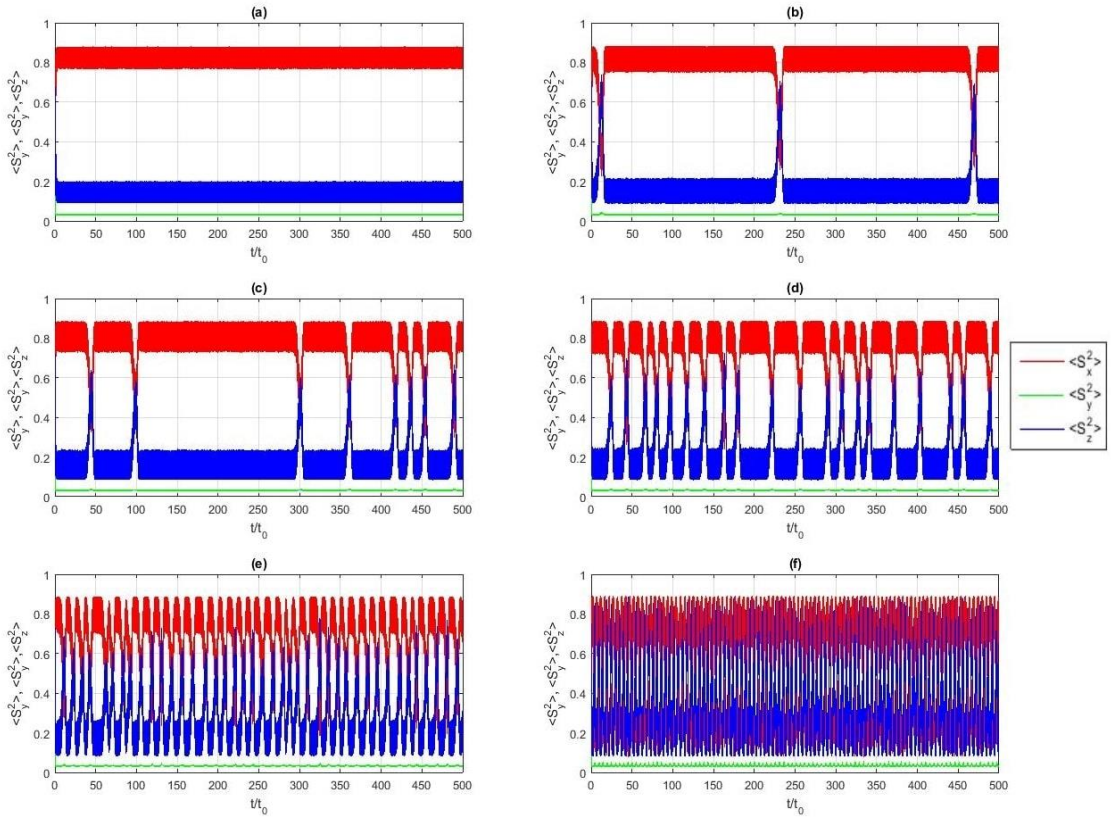

Figure 3.2: *The behavior of nematic spins in x- and z-directions for* $B_0^2 = 0.7$ *for different periods:* $t_0 = 350$ *(a),* $t_0 = 375$ *(b),* $t_0 = 400$ *(c),* $t_0 = 425$ *(d),* $t_0 = 450$ *(e),* $t_0 = 500$ *(f).* No impurities are present.

In the shown case, one can distinguish three qualitatively different regimes for $B_0^2 = 0.7$ on increasing t_0. In the regime $t_0 < t_c^{(1)}$~370, where $t_c^{(1)}$ roughly locates the minimum of $\langle g(t_0) \rangle$, the field rotation is too fast for spins to follow $\boldsymbol{B}$. Consequently, $\boldsymbol{S}_\alpha(t)$ fluctuates about a well-defined average orientation (see Figure 3.2, the case: $t_0 = 350$). In the 2$^{\text{nd}}$ regime, extending in the interval $t_c^{(1)}$~$350 < t_0 < t_c^{(2)}$~425, $\boldsymbol{S}_\alpha(t)$ displays relatively irregular attempts to reorient (see Figure 3.2**,** the case: $350 < t_0 < 425$). One could observe some sort of period doubling behaviour within this interval, which is an inherent feature of a chaotic process. Finally, for a slow enough rotation of $\boldsymbol{B}$ (i.e. $t_0 > t_c^{(2)}$) we obtain a relatively regular $\boldsymbol{S}_\alpha(t)$ behavior (Figure 3.2**,** $t_0 > 410$). It should be noted that for larger values of B_0 one could observe qualitatively the same behavior, where values of $t_c^{(1)}$ and $t_c^{(2)}$ are functions of B_0.

At the next stage, we show that the $\boldsymbol{S}_\alpha(t)$ dynamics can be strongly influenced by the anchoring strength. In Figure 3.3 we follow $\boldsymbol{S}_\alpha(t)$ behaviour on varying the anchoring strength W_s. One sees that below W_s~5 one observes tumbling-like dynamics, where the characteristic frequency increases with decreasing value of W_s.

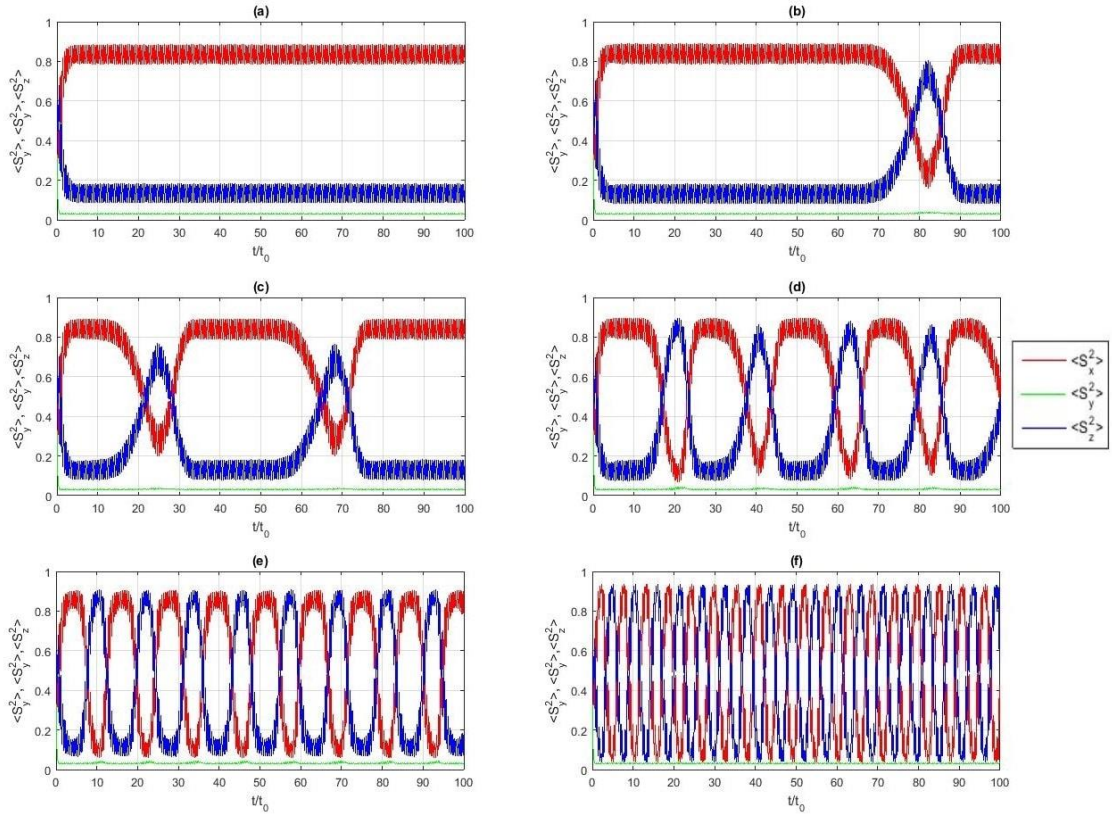

Figure 3.3: *The behavior of nematic spins* $\langle S_x^2\rangle$, $\langle S_y^2\rangle$, $\langle S_z^2\rangle$ *for different values of the anchoring constant:* $W_s = 5.0$ *(a),* $W_s = 4.66$ *(b),* $W_s = 4.5$ *(c),* $W_s = 4.2$ *(d),* $W_s = 3.0$ *(e),* $W_s = 1.0$ *(f).* No impurities are present.

It is also of interest to investigate the role of impurities in the system behaviour. For this purpose, we introduce the probability p for a site to be occupied by an impurity. In Figure 3.4 we report results of nematic spins $\langle S_x^2\rangle, \langle S_y^2\rangle, \langle S_z^2\rangle$ versus the periods of rotation. Keeping $p = 0.01$ and increasing t_0 from 50 to 500, the transition from just oscillation to chaotic behavior occurs, which is illustrated in Figure 3.4. However, we observed that, in comparison to the case illustrated in Figure 3.2 there is a frequency shift in the range of lower values t_0. As consequence, the system displays chaotic behavior for larger values of amplitude in comparison with the case demonstrated in Figure 3.2.

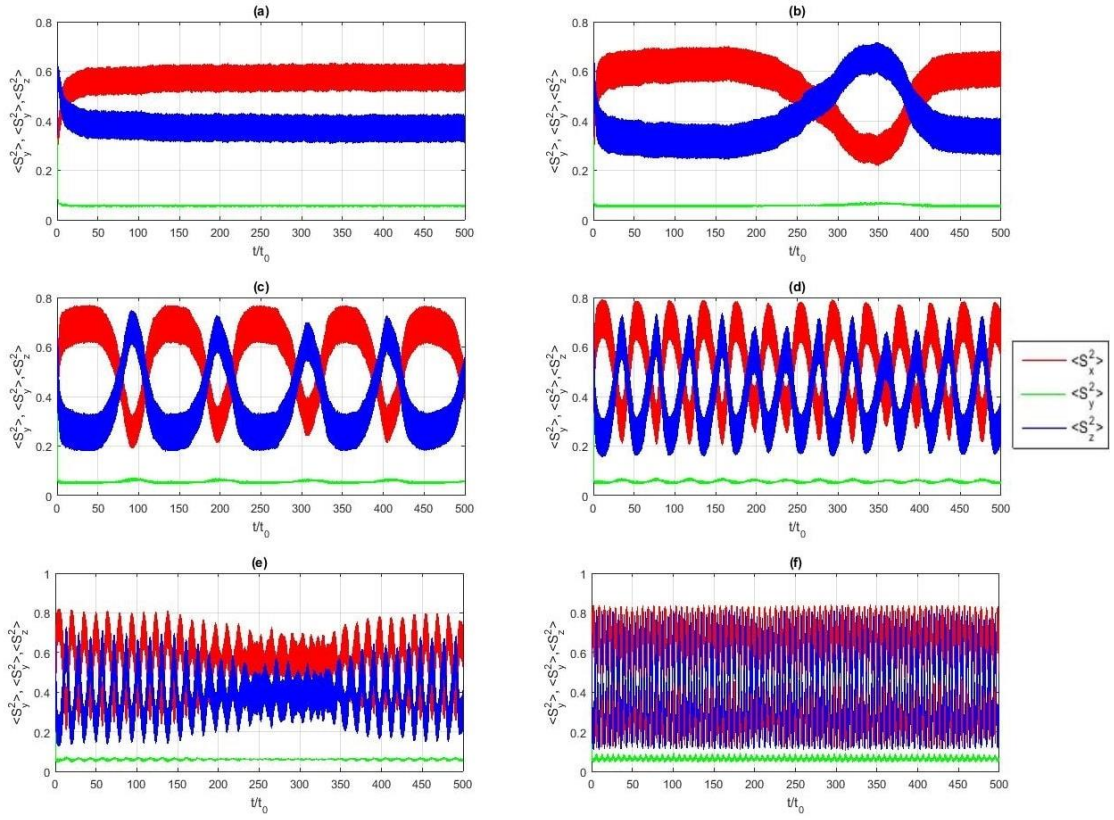

Figure 3.4: *The average behavior of nematic spins in x-, y- and z-directions for* $B_0^2 = 0.7$ *for different periods:* $t_0 = 100$ *(a),* $t_0 = 150$ *(b),* $t_0 = 200$ *(c),* $t_0 = 250$ *(d),* $t_0 = 300$ *(e),* $t_0 = 450$ *(f),* $p = 0.01$.

3.2 Topological Defects

In this Section, the effect of confinement topology and geometry on spatial positioning of nematic topological defects is given. An analysis of decomposition of TDs into elementary TDs is presented. Afterwards, it is demonstrated that in certain confinement geometries varying order parameter correlation length size could trigger global rotation of an assembly of TDs. Next Subsection considers studying defect pattern diversity in 2D for fixed boundary conditions on varying different control parameters. We demonstrate that non-unique topologic charge can be imposed due to confinement enforced sharp edges. Emphasis is given to an external electric field driven changes between different topologies. Switching between two different diagonal states caused by the rotational electric filed is presented. In addition, global nematic structural changes enabled by the creation or annihilation of pairs $\{defect, antidefect\}$ are shown. In the last Subsection, we show how an external electric field could be used to drag the boojum fingertip towards the interior of a confinement cell. We analyze how NP's surface manipulation influences NP positioning. Special attention is devoted to the impact of mechanical force on a NP immersed in orientationally-ordered LC medium.

3.2.1 Decomposition of TDs and Faraday effect

Of our interest are topological defects in relatively thin nematic liquid crystalline films. In order to study a stabilization of such configurations, we consider a thin plane-parallel cell of thickness h, described in the Cartesian coordinate frame (x, y, z) and shown in Figure 3.5. The top and the bottom plates are placed at $z = 0$ and $z = h$, respectively. We set up special boundary condition at the top plate to which we henceforth refer as the Boundary Anchoring Condition (BAC) [12]. In the case of BAC, we suggest that the cell is relatively thin and the nematic ordering is entirely dominated by conditions at the top "master" plate. We impose a strong uniaxial boundary condition of the order parameter $\boldsymbol{Q}_s$, defined by Eqs. (2.134, 2.136). The latter is either a circle of radius $R = \sqrt{x^2 + y^2}$ or a trapezoid characterized by a distance R. Note that the radius is large with respect to the relevant nematic order correlation length. We allow nematic molecules to freely rotate in the (x, y) plane inside the given boundary. In these simulations, the nematic ordering is treated as effectively two dimensional. Consequently, we neglect variations along the z-axis and set $\boldsymbol{Q} = \boldsymbol{Q}(x, y)$ [121].

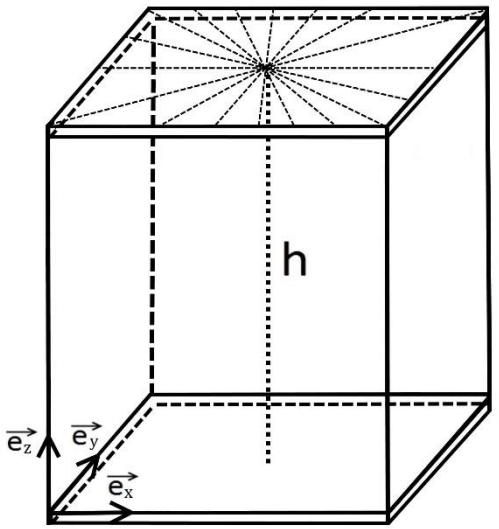

Figure 3.5: *Geometry of cell used in simulations.* At the top "master" plate uniaxial nematic structures exhibiting effectively two-dimensional $\boldsymbol{Q} = \boldsymbol{Q}(x, y)$ behavior are enforced [121].

Note that in our simulations we mimic geometric set-ups which could be realized experimentally using, for instance, the atomic force microscope scribing method [11]. In typical experimental set up one confines a nematic LC within a thin plane-parallel cell, where at least one ("master") surface imposes anchoring conditions inscribed via an AFM stylus [11], with a planar-degenerate "slave" as the other surface.

We first restrict our attention to the case in which the total topological charge of strength m is enforced inside the circular boundary of radius R. For this purpose, at the boundary, we strongly impose the nematic ordering defined by Eq. (2.136). The resulting configurations are plotted in Figures (3.6, 3.7).

In Figure 3.6, we plot equilibrium biaxiality profiles in which cores of TDs are clearly visible. One can see the general tendency for the imposed total charges always decompose into TDs bearing elementary charges $m_0 = 1/2$. It is a consequence of a local elastic cost

$\Delta F \sim m^2$. The cores of m_0 TDs are fingerprinted by a volcano-like rim where β^2 [12, 121]. For $m = 1$, $m = 2$, $m = 4$ and $m = 6$ the patterns possess 2, 4, 8 and 12 TDs. Due to the so called head-to-tail nematic symmetry, it holds $m_0 = \pm 1/2$. We consider only cases with $m > 0$. The TDs tend to assemble close to the boundary. The resulting director orientations are plotted in Figure 3.7. We plot eigenvectors of $\boldsymbol{Q}$ with the largest positive eigenvalue (which we set to be $\boldsymbol{e}_1$), which in the uniaxial limit corresponds to the nematic director field. Note that the nematic textures are essentially uniaxial, except close to the defects cores. For this reason, we henceforth refer to $\boldsymbol{e}_1$ as the nematic director field. The ordering becomes increasingly spatially uniform in the central region with increasing values of m [70].

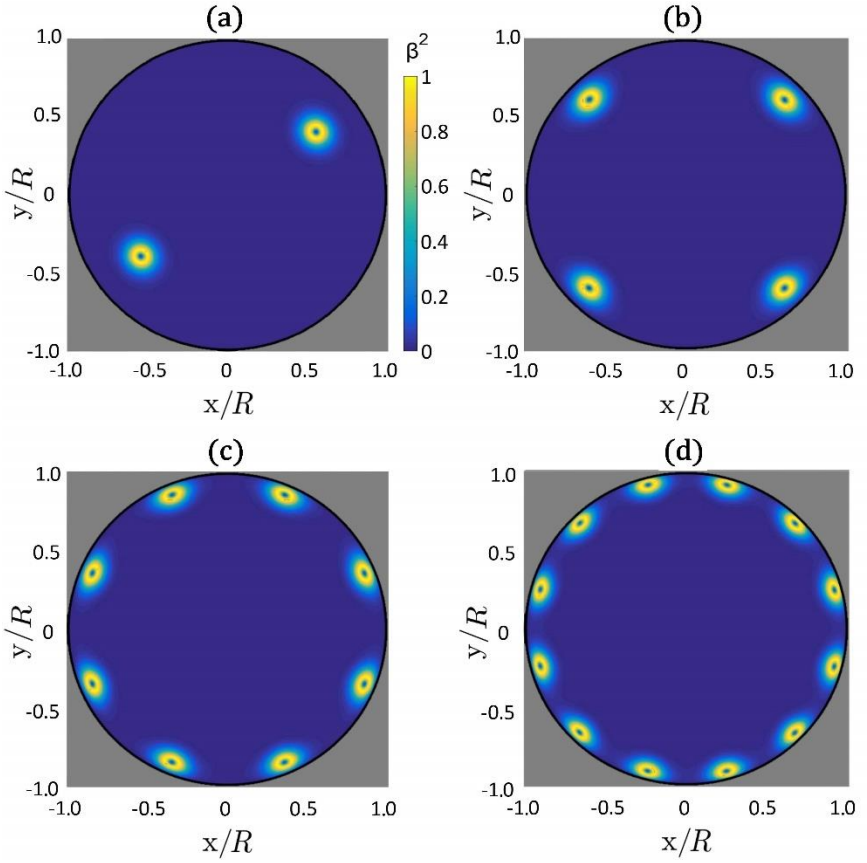

Figure 3.6: *Plots of $\beta^2(x, y)$ for different imposed total topological charges using BAC: (a) $m = 1$, (b) $m = 2$, (c) $m = 4$, (d) $m = 6$.* In all cases, TDs are decomposed into elementary units bearing the charge $m_0 = 1/2$, which assemble close to the bounding circle. In all figures, we set: $R/\xi_b = 30$, $\tau = -8$. The corresponding orientational order is depicted in Figure 3.7 [121].

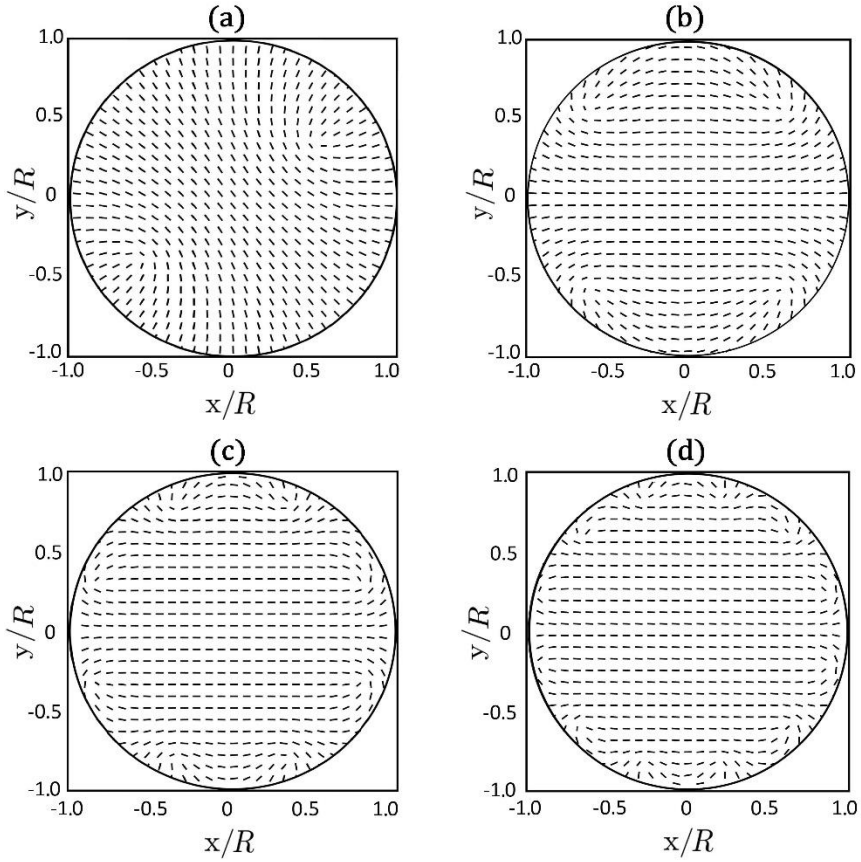

Figure 3.7: *2D Plot of the* $\boldsymbol{Q}$ *eigenvector with the largest positive eigenvalue, corresponding to the 2D biaxiality profiles* $\beta^2(x, y)$ *plotted in Figure 3.6: (a)* $m = 1$*, (b)* $m = 2$*, (c)* $m = 4$*, (d)* $m = 6$*,* $R/\xi_b = 30$*,* $\tau = -8$ [121].

This phenomenon is reminiscent of the Faraday cavity effect in conductors. Namely, if one puts electric charges on a conducting body, the charges assemble at its surface and the resulting electric field inside the body vanishes. The Faraday-like behavior in our simulations is clearly visible for cases $R/\xi_b >> 1$. The absence of an electric field inside the conductor in the electrostatic analogue corresponds in our simulations to a spatially uniform nematic director in the area separated by a distance greater than ξ_b from the confining boundary [121].

At the next stage, we focus on the cases in which the symmetry of the bounding surface is changed. For this reason, we consider a trapezoid shaped boundary, through which we enforce $m = 3$ using Eq. (2.136). The corresponding equilibrium nematic configurations for a given boundary are shown in Figures (3.8, 3.9). In all cases, the imposed charge decays into elementary charges $m_0 = 1/2$, and the charges assemble at the confining boundary as discussed in the previous subsection. For this specific confinement symmetry, we observe the rotation of nematic patterns on decreasing the ration $\eta = R/\xi_b$, where R corresponds to the bottom length of the trapezoid. In practice, one could vary η by changing the temperature of the sample, which affects ξ_b. The rotation of the pattern reveals that the system's energy landscape substantially changes on varying η. From the perspective of TDs, the LC configurations reflect the interplay between mutual repulsion among like defects and interaction of TDs with confinement geometry. Note that for sufficiently symmetric confinement, the rotation disappears. It is also sensitive to the number of TDs [121].

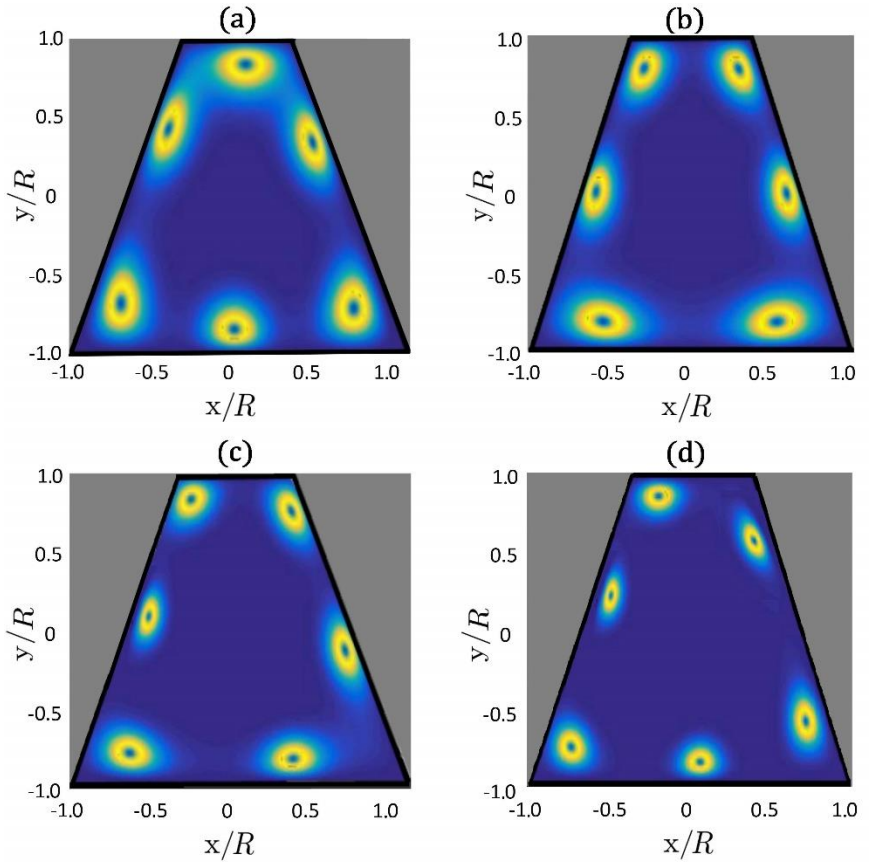

Figure 3.8: $\beta^2(x,y)$ *plots of the configuration of TDs on increasing the ratio* $\eta = R/\xi_b$ *(a)* $\eta = 14$*, (b)* $\eta = 17$*, (c)* $\eta = 21$*, (d)* $\eta = 25$. In practice, this could be achieved by decreasing the temperature of the sample. The trapezoidal boundary enforces the total topological charge $m = 3$, which splits into six $m_0 = 1/2$ elementary charges. Each defect is marked with a number in order to track its position with increasing η [121].

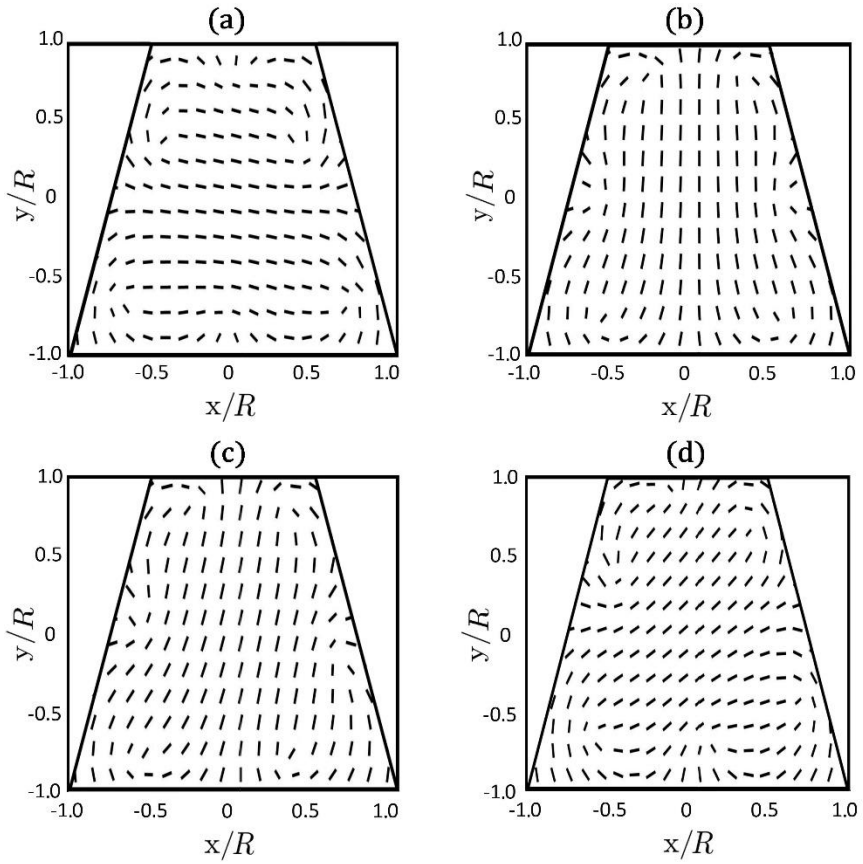

Figure 3.9: *Rotation of the nemaic director field on increasing the ratio* $\eta = R/\xi_b$ *(a)* $\eta = 14$*, (b)* $\eta = 17$*, (c)* $\eta = 21$*, (d)* $\eta = 25$*.* The corresponding biaxiality profile is depicted in Figure 3.8 [121].

3.2.2 Confinement induced TDs

Our goal is to demonstrate that the total topological charge within a 2D region enclosed by a boundary possessing sharp edges is not uniquely defined due to the head-to-tail invariance of $\boldsymbol{n}$. To demonstrate this we use a simple geometry in the Cartesian coordinate system (x, y) depicted in Figure 3.5. The director field in the Cartesian coordinates (x, y) is defined by Eq. (2.134). We consider a nematic LC confined within a square characterised by the length a, where the strong tangential anchoring condition is enforced at the boundaries. Therefore, $\boldsymbol{n}[x = 0, y] = \boldsymbol{n}[x = a, y] = \pm\boldsymbol{e}_y$, $\boldsymbol{n}[x, y = 0] = \boldsymbol{n}[x, y = a] = \pm\boldsymbol{e}_x$.

A total topological charge m_{tot}, which in 2D equals to the winding number, within the bounded region is given by $m_{tot} = \frac{1}{2\pi}\oint \frac{\partial\Theta}{\partial s} ds$, where the integral runs over the closed boundary. The integration is performed counter-clockwise and ds stands for the infinitesimal length along the integration path. The head-to-tail invariance of $\boldsymbol{n}$ allows five different outcomes, yielding $m_{tot} \in [0, \pm 0.5, \pm 1]$. For example, these values could emerge from the following discontinues changes in Θ at the square edges: $m_{tot} = \frac{1}{2\pi}(\frac{\pi}{2} + \frac{\pi}{2} + \frac{\pi}{2} + \frac{\pi}{2}) = 1$, $m_{tot} = \frac{1}{2\pi}(-\frac{\pi}{2} - \frac{\pi}{2} - \frac{\pi}{2} - \frac{\pi}{2}) = -1$, $m_{tot} = \frac{1}{2\pi}(\frac{\pi}{2} - \frac{\pi}{2} + \frac{\pi}{2} - \frac{\pi}{2}) = 0$, $m_{tot} = \frac{1}{2\pi}(\frac{\pi}{2} - \frac{\pi}{2} + \frac{\pi}{2} + \frac{\pi}{2}) = 0.5$, $m_{tot} = \frac{1}{2\pi}(\frac{\pi}{2} - \frac{\pi}{2} - \frac{\pi}{2} - \frac{\pi}{2}) = -1$. Note that these outcomes are allowed by topology. In general, they could be realised in equilibrium due to energetic reasons (i.e., the resulting states should be at least metastable). In the following, we demonstrate that configurations bearing different m_{tot} could be realised within the

confined system. Furthermore, we demonstrate how one could switch between topologically different states using an appropriate external electric field.

In Figure 3.10 we show some stable nematic patterns characterised by different values of m_{tot}. We stabilised them using different initial seed configurations. The structure in Figure 3.10(I) is defectless and $m_{tot} = 0$. We refer to this pattern as the *right diagonal structure*. The structure in Figure 3.10(II) (Figure 3.10(III)) exhibits $m_{tot} = 1$ ($m_{tot} = -1$) and possesses two $m_0 = 1/2$ ($m_0 = -1/2$) TDs and exhibits mirror symmetry. On the contrary, in structures Figure 3.10(IV) and Figure 3.10(V), exhibiting $m_{tot} = 1$ and $m_{tot} = -1$, this symmetry is broken.

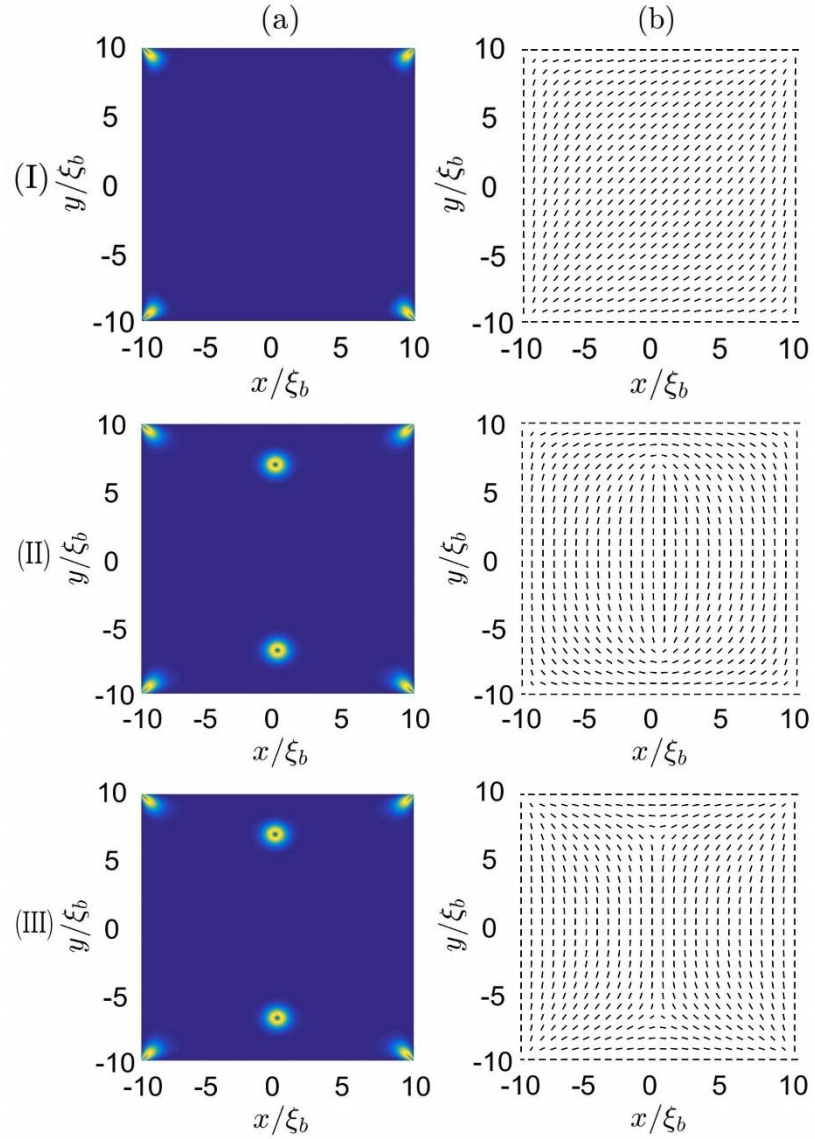

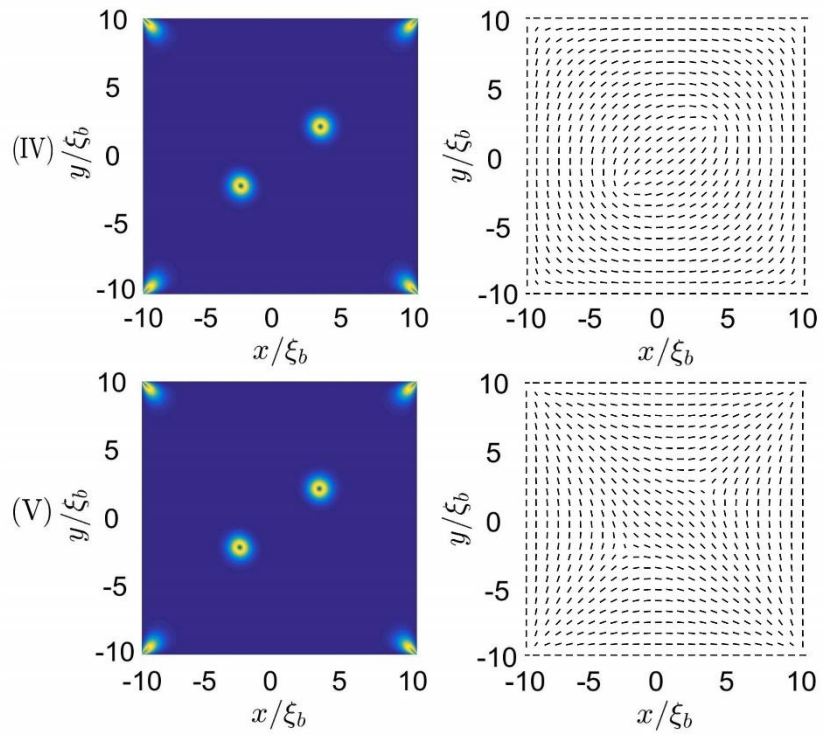

Figure 3.10: *Different order parameter structures realized for the same boundary conditions.* Column (a): $\beta^2(x,y)$ plots of the nematic configuration where we impose different initial states using equation $\Theta = m\ tan^{-1}(\frac{y}{x}) + \frac{\pi}{4}$: (I) $m = 0$, (II) $m = 1/2$, (III) $m = -1/2$, (IV) $m = 1$, (V) $m = -1$. Column (b): 2D plot of the $\boldsymbol{Q}$ eigenvector with the largest positive eigenvalue, corresponding to the 2D biaxiality profiles $\beta^2(x,y)$ plotted in the Column (a). $A_e = 20$, $\tau = -8$.

In Figure 3.11 we illustrate that one could switch between structures exhibiting different values of m_{tot} using an external electric field $\boldsymbol{E}$. For this purpose, we originate from a structure (Figure 3.10(I)) characterised by $m_{tot} = -1$, which is metastable for $\boldsymbol{E} = 0$. Then, we apply a spatially homogeneous $\boldsymbol{E}$ along the right diagonal (i.e. $\boldsymbol{E} = \frac{E}{\sqrt{2}}(\boldsymbol{e}_x + \boldsymbol{e}_y)$) and gradually increase its magnitude. One sees that on average global $\boldsymbol{n}$ orientation becomes better aligned along $\boldsymbol{E}$ which is enabled by dragging defects along the upper right and down left corner (see Figures 3.11(II)-(IV)). For a strong enough value of E both defects are absorbed by respective corners, which result in defect-less structure bearing $m_{tot} = 0$ (Figure 3.11(V)). The latter structure remains qualitatively the same also if the field is afterwards switched off.

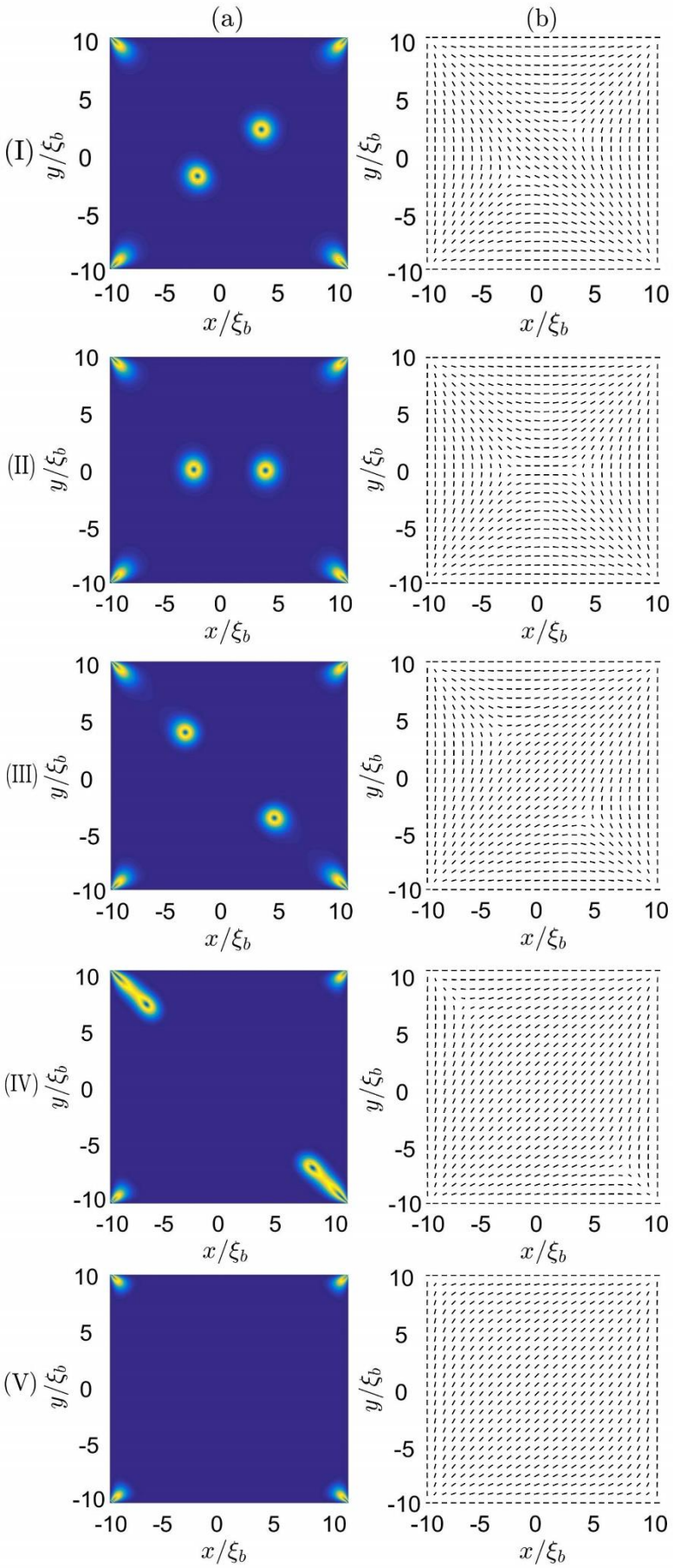
(a)
(b)
(I)
(II)
(III)
(IV)
(V)
y/ξ_b
x/ξ_b
10
5
0
-5
-10

Figure 3.11: *An electric field driven transformation between two different topological states.* In Figure 3.11 (I): (a, b) $\beta^2(x, y)$ plots and corresponding director profiles are shown, where we initially impose a structure bearing a single $m = -1$ defect. The transformation was obtained by increasing the amplitude of the static external electric field A_f: (I) $A_f = 0$, (II) $A_f = 2.5$, (III) $A_f = 12$, (IV) $A_f = 21$, (V) $A_f = 25$. $A_e = 20$, $\theta_f = \pi/4$, $\tau = -8$.

We next demonstrate that a "domain"-type reorientations could be enabled by creation or/and annihilation of pairs {*defect, antidefect*}. For this purpose we originate from the defect-less *left diagonal structure*, see Figure 3.12(I). Then we switch on $\boldsymbol{E}$, which we gradually rotate from $(-\boldsymbol{e}_x + \boldsymbol{e}_y)$ towards $(\boldsymbol{e}_x + \boldsymbol{e}_y)$. These terminal $\boldsymbol{E}$ orientations favour the *left diagonal structure* and *right diagonal structure,* respectively. The reorientation is relatively slow, so that intermediate states are close to equilibrium configurations. The "left-right" structural transformation necessitates the reorientation of the "central" domain (the part of the system, which is roughly aligned along the same direction). To enable this two pairs {*defect, antidefect*} are created in intermediate structures close to the upper and bottom boundary (see Figures. 3.12(II)-(IV)). Therefore, this transformation is enabled by the presence of intermediate (transient) pairs of TDs.

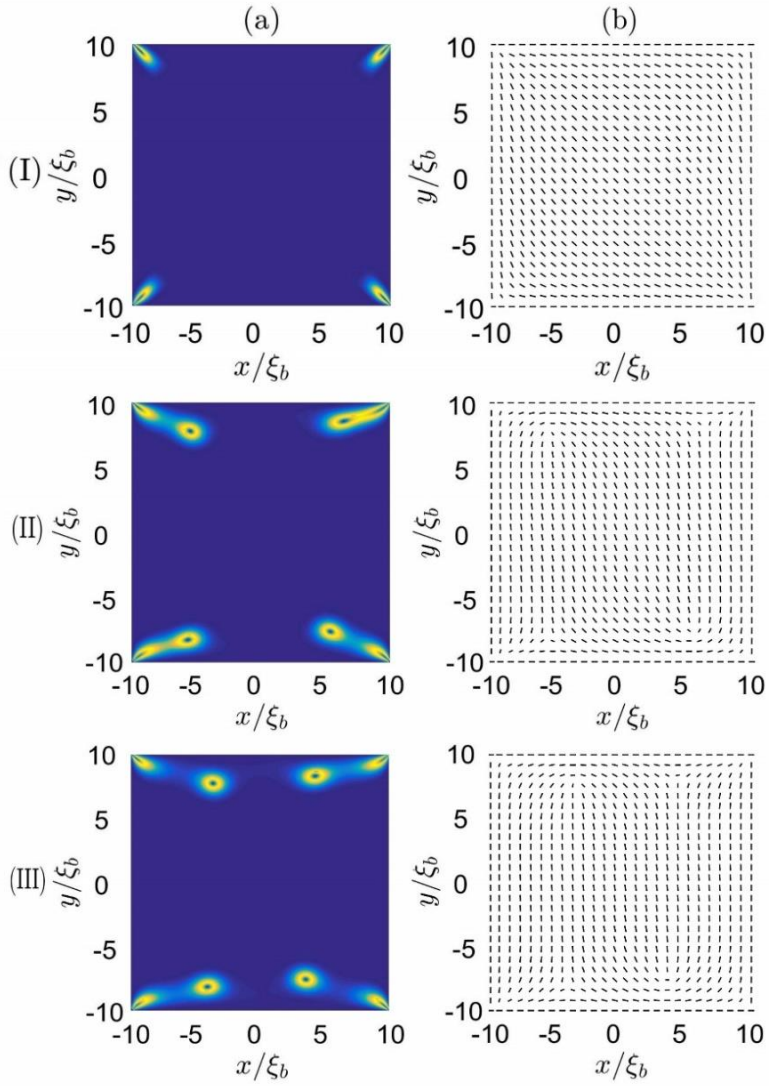

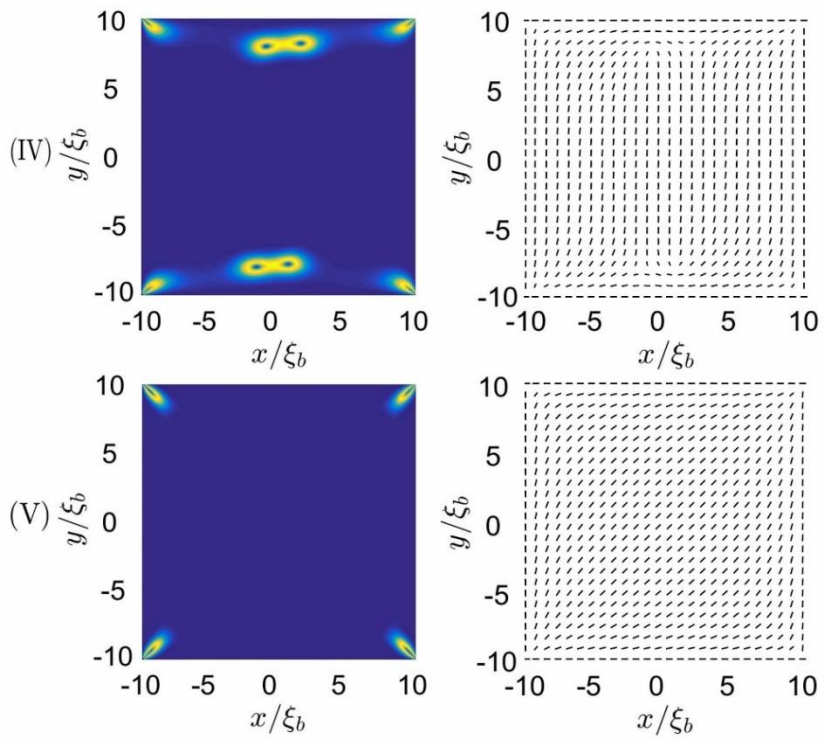

Figure 3.12: *Switching between two different diagonal states.* (I) $\theta_f = 3\pi/4$, (II) $\theta_f = 2\pi/3$, (III) $\theta_f = 5\pi/9$, (IV) $\theta_f = \pi/2$, (V) $\theta_f = \pi/4$. $A_e = 20$, $A_f = 17$, $\tau = -8$.

Note that this "left-right" transformation could be realised also by using other external field driven processes. To illustrate this we switch on a static field $\boldsymbol{E} = \frac{E}{\sqrt{2}}(\boldsymbol{e}_x + \boldsymbol{e}_y)$), where the initial nematic pattern exhibits the *left diagonal structure*, see Figure 3.13 (I). The obtained results are shown in Figure 3.13. One sees that at each corner a defect bearing $m_0 = 1/2$ is formed, where their total topological charge equals zero (Figure 3.13(I)). Afterwards, these TDs are pushed along the diagonals (Figures 3.13(II)-(IV)). Finally, the TDs collide and mutually annihilate at the crossing point of diagonals (Figure 3.13(IV)). This annihilation enables transformation into the *right diagonal structure*, see Figure 3.13 (V).

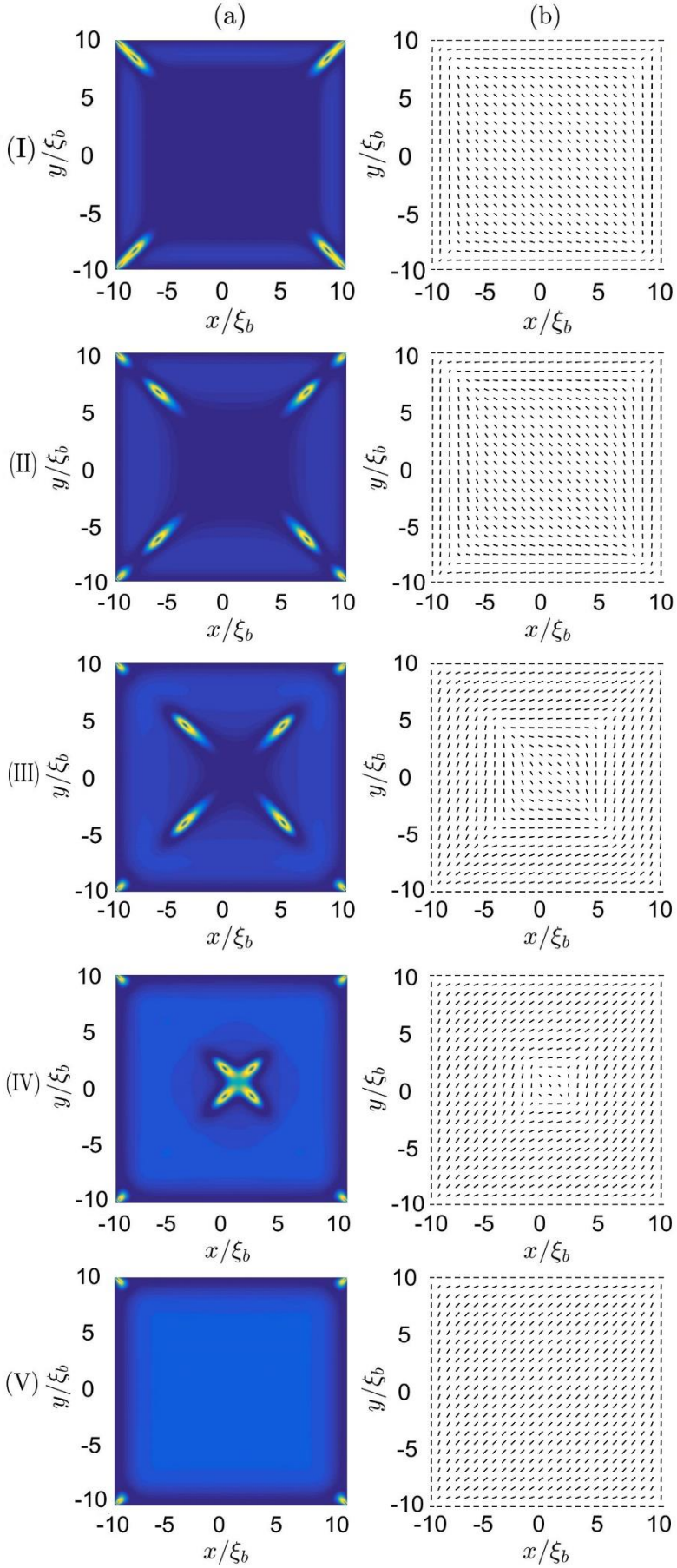
(a)
(b)
(I)
(II)
(III)
(IV)
(V)
10
5
0
-5
-10
y/ξ_b
x/ξ_b

Figure 3.13: *A field driven transformation between a "left diagonal" and "right diagonal" configuration.* Time-dependent field imposed structural changes in biaxiality and director field profile are plotted in column (a) and (b) respectively. (I) $\epsilon = 3$, (II) $\epsilon = 4$, (III) $\epsilon = 6$, (IV) $\epsilon = 7$, (V) $\epsilon = 8$. The other parameters in all cases equal to $A_e = 20$, $A_f = 45$, $\omega_f = 3$, $\gamma = 1$, $\tau = -8$.

Next, we illustrate different ways of manipulations of TDs within the system, which could be realised experimentally. For this purpose, we enforce a pair of {3/2,-3/2} TDs within the square, so that the total topological charge equals zero, see Figure 3.10(I). In simulations, we create these TDs using the *surface anchoring field* enforcing a pair of {3/2,-3/2} point defects. Due to a finite anchoring strength w, the TDs decay into *elementary charges* bearing $m_0 = \pm 1/2$, see Figure 3.14(I). Then we gradually decrease the anchoring strength and follow the annihilation of TDs into the final defect-less state (see Figure 3.14 (II)-(V)). One sees (see Figure 3.14(III)) that the symmetry is broken at intermediate stages. One could mimic experimentally a similar process by imprinting the initial pattern using the AFM scribing method. Effective anchoring strength could be reduced by choosing LCs which exhibits in additional to nematic also SmA ordering. On approaching the N-SmA phase transition the average Frank elastic constant k_i increases. Consequently, the dimensionless quantity $A_s = w^2 h/k_i$ decreases, where h stands for the cell thickness.

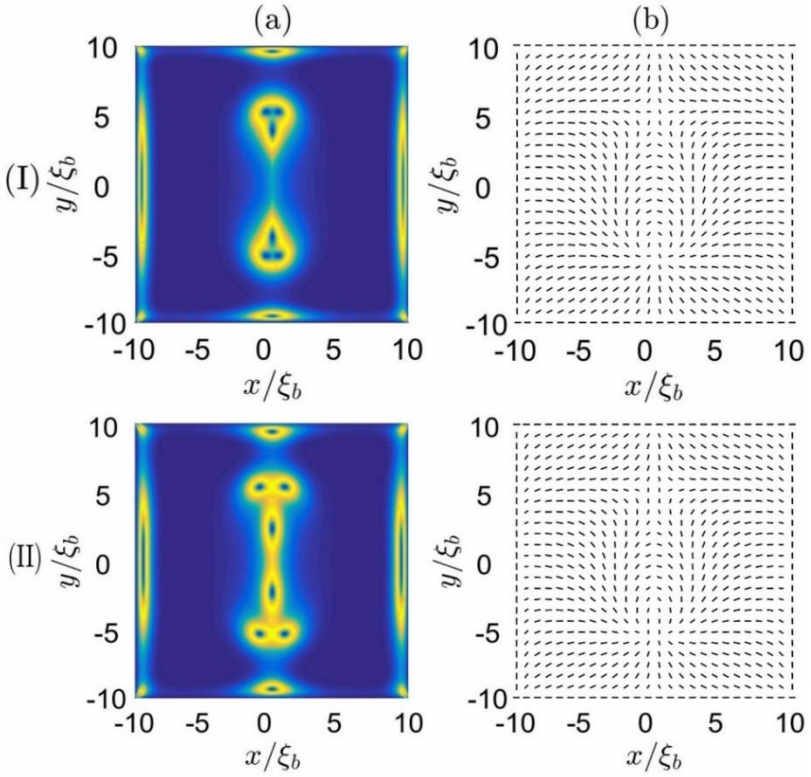

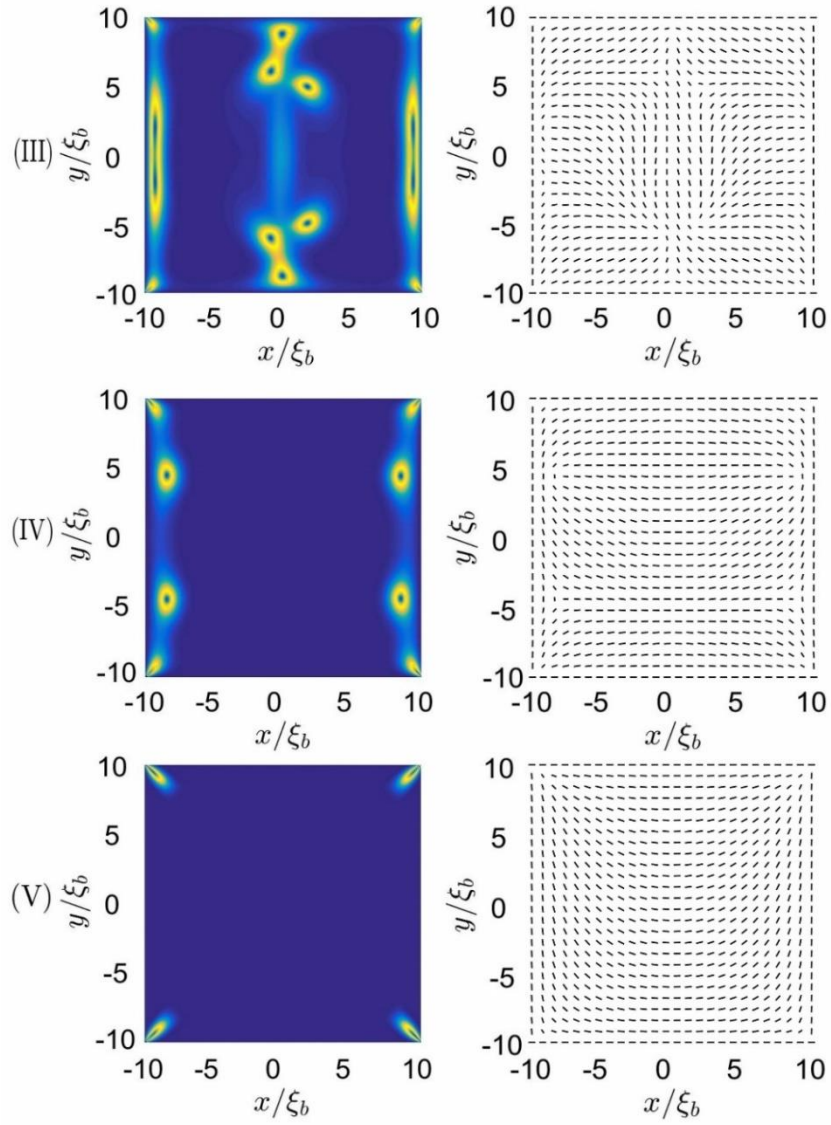

Figure 3.14: *Surface anchoring enforced annihilation of TDs.* The degree of biaxiality β^2 in (x, y) plane plots are shown in the column (a); the corresponding director profiles are depicted in column (b). We impose via field anchoring condition of strength equals A_s a pair of point defects with charges $\{\frac{3}{2}, -\frac{3}{2}\}$. With decreasing anchoring strength the defects annihilate. (I) $A_s = 2.0$, (II) $A_s = 1.2$, (III) $A_s = 0.63$, (IV) $A_s = 0.15$, (V) $A_s = 0.0$. We determine a critical value of $A_s = A_s^{(c)}(m)$~1.2 , where TDs decompose into elementary defects bearing the topological charge $m_0 = 1/2$. $A_e = 20$, $\tau = -8$.

In Fig. 3.15 we illustrate how annihilation of the initial pattern shown in Figure 3.15(I) could be realised by switching on an external field $\boldsymbol{E} = E\boldsymbol{e}_z$, which favours dimensionless structure, in which $\boldsymbol{n}$ is preferentially aligned along $\boldsymbol{e}_z$. Also in these figures (see Figs. 3.15 (II)-(IV)) we mark with red-dashed lines pairs of TDs which annihilate in the next stage shown.

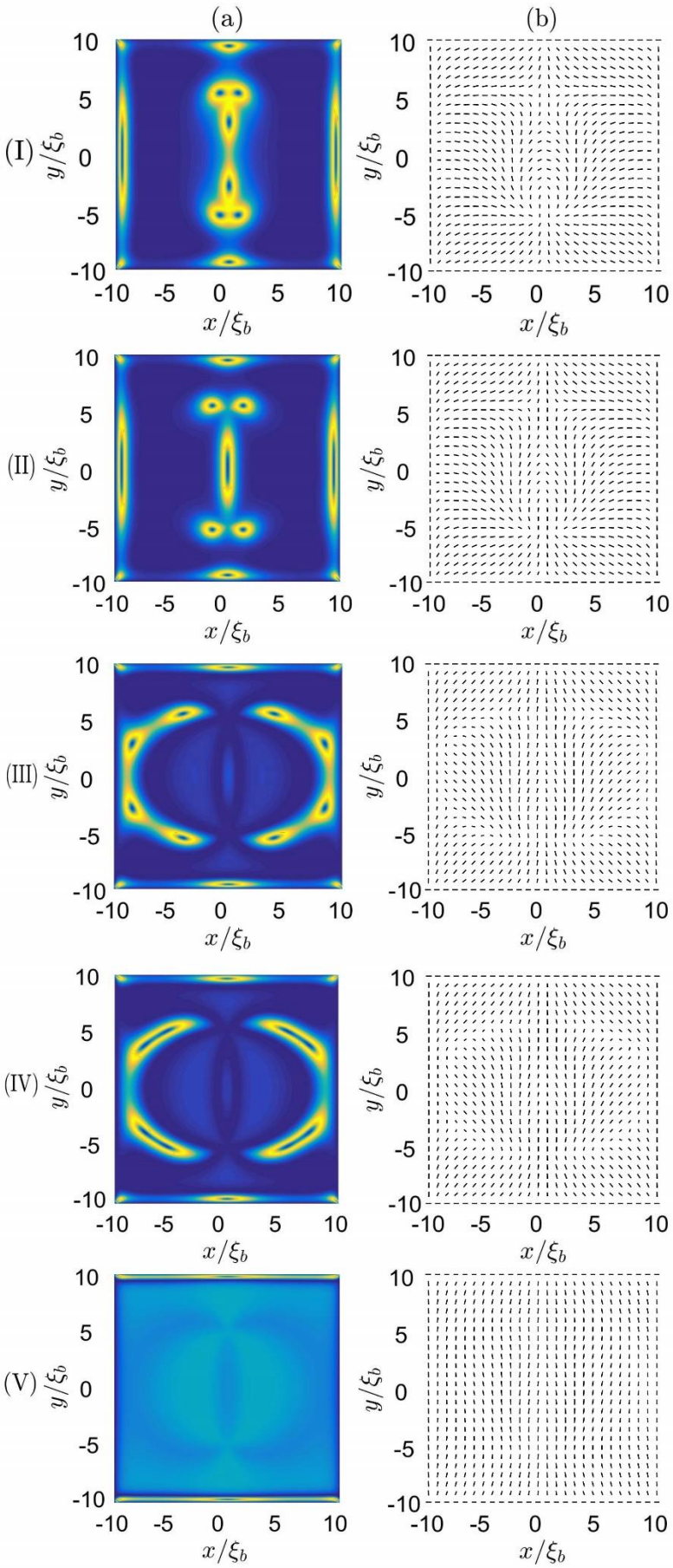
(a)
(b)
(I)
(II)
(III)
(IV)
(V)
y/ξ_b
x/ξ_b
10
5
0
-5
-10

Figure 3.15: *External field driven annihilation of TDs.* We enforce a pair of point defects $\{\frac{3}{2}, -\frac{3}{2}\}$ with the surface anchoring field strength $A_s = 1.2$ as shown in (Figure 3.14(II): a, b)). Then we gradually increase the external field in the z-direction and the imposed defects gradually annihilate into the defectless state. The 2D biaxiality profiles $\beta^2(x, y)$ and corresponding director field profiles were plotted for different amplitudes of the electrical field: (I) $A_f = 0.0$, (II) $A_f = 23$, (III) $A_f = 52$, (IV) $A_f = 54$, (V) $A_f = 90$. $A_e = 20$, $\tau = -8$.

In Figure 3.16 we illustrate that annihilation details are sensitive to details. We consider a similar case as in Figure 3.14, i.e., we gradually decrease the anchoring strength. However, in this case, we introduce "imperfections" (i.e., we introduce two small patch, which locally favors homogeneous orientation). With decreasing anchoring strength a defectless state is reached, which is however different compared to annihilation shown in Figure 3.14. This simulation shows that imperfections could in general lead to different "annihilation paths".

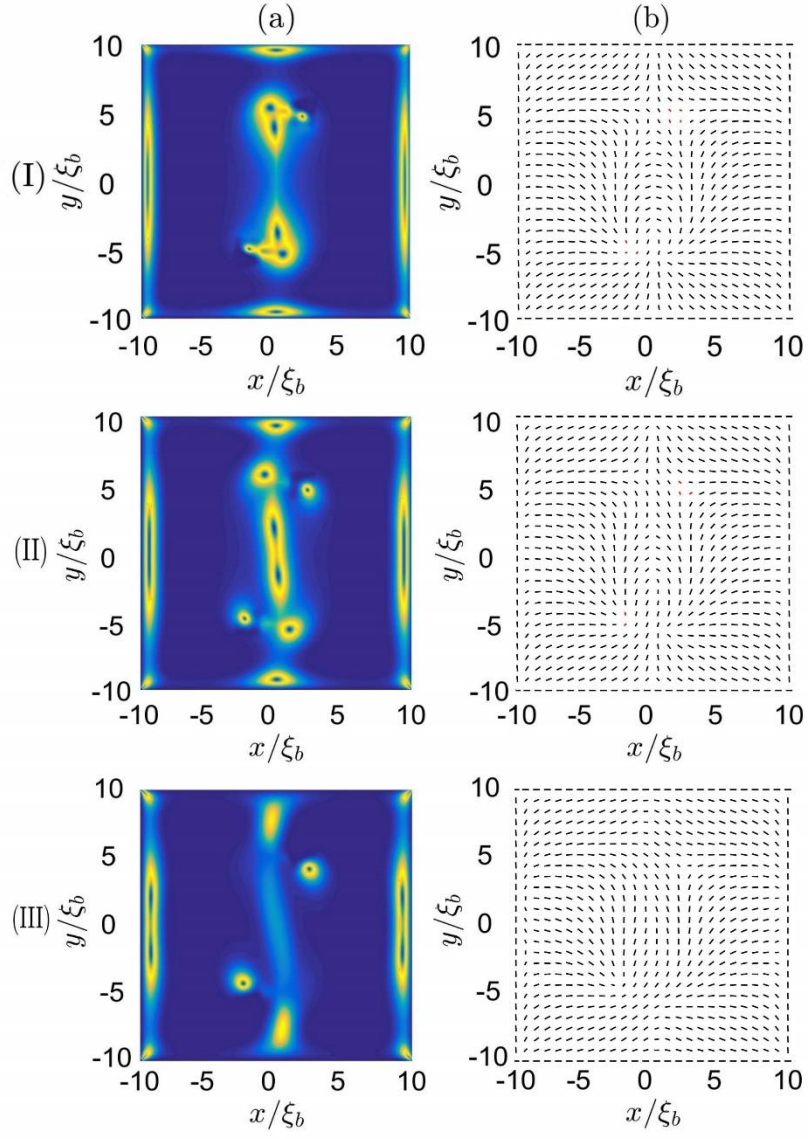

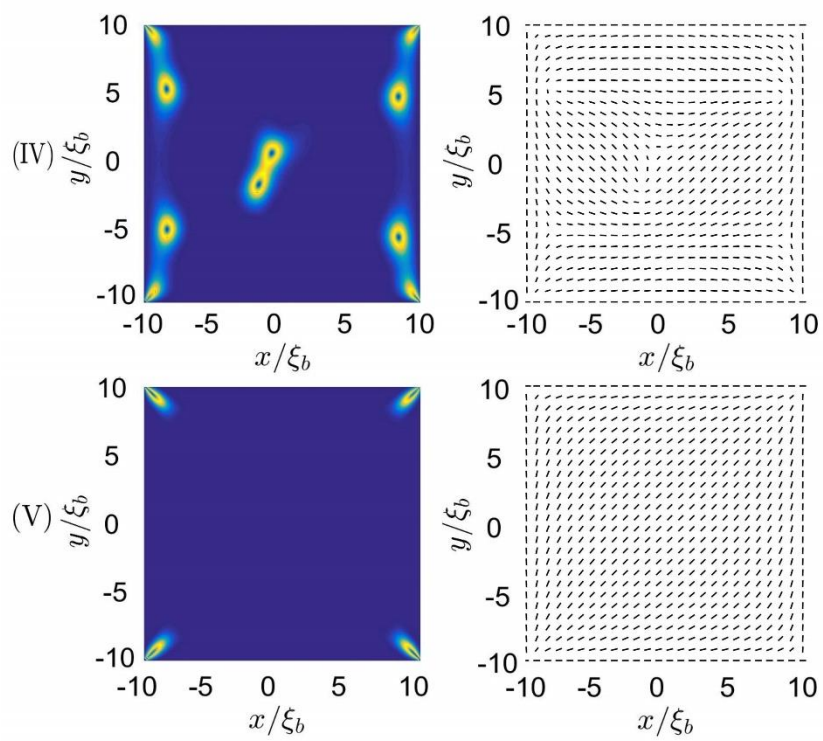

Figure 3.16: *Sensitivity of defects patterns to imperfections enforced by a local perturbation field.* We introduce the the perturbation patches of size $h_p = 2\xi_b$ are placed at coordinates $(x_{p1} = -\frac{h}{10},\ y_{p1} = -\frac{h}{4})$, $(x_{p2} = \frac{h}{10},\ y_{p2} = \frac{h}{4})$ in the system. (I) $A_s = 2.0$, (II) $A_f = 0.98$, (III) $A_f = 0.6$, (IV) $A_f = 0.153$, (V) $A_f = 0.0$. $A_s^{(p)} = 0.1,\ \varphi_{s1}^{(p)} = \varphi_{s2}^{(p)} = \frac{9\pi}{8}$, $A_e = 20,\ \tau = -8$.

3.2.3 Field induced changes in TD structures and positions

Our aim is to demonstrate how one could drag boojum [74] (surface topological defect) towards the cell interior. For sake of simplicity, which does not affect the general validity of results obtained, we restrict our attention to the case in which a cell exhibits a cylindrical symmetry. In the cylindrical coordinate system, we consider the hybrid plane-parallel cell, enforcing the radial uniaxial orientation $\boldsymbol{Q}_{rad}^{(s)} = S_{eq}(\boldsymbol{e}_r \otimes \boldsymbol{e}_r - \frac{\boldsymbol{I}}{3})$ and the uniaxial homeotropic orientation along z-axis $\boldsymbol{Q}_{hom}^{(s)} = S_{eq}(\boldsymbol{e}_z \otimes \boldsymbol{e}_z - \frac{\boldsymbol{I}}{3})$ enforced at the top and bottom plane, respectively, whereas at the cylinder wall free boundary condition is imposed. We henceforth refer to these conditions as Surface Anchoring Condition (SAC). They impose a boojum TD at the top plate [74, 122]. The corresponding geometry of the problem is depicted in Figure 3.17.

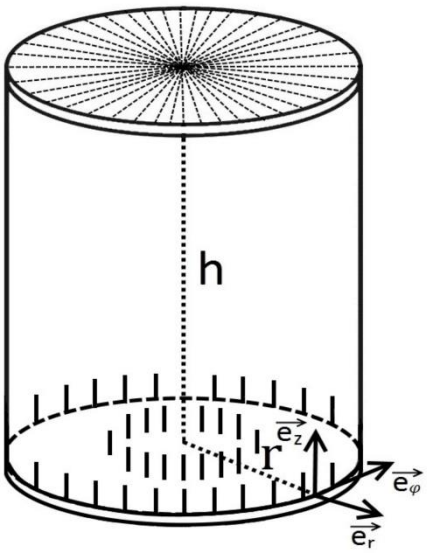

Figure 3.17: *The hybrid plan-parallel cell of thickness h.* The top plate exhibits the radial uniaxial orientation, whereas at the bottom a uniaxial homeotropic orientation along the z-axis is enforced. The free boundary condition is imposed at the lateral cylindrical walls [121].

At the first stage of our investigation, we consider thicker cells and SAC boundary conditions. For sufficiently strong anchoring, a boojum surface defect [74, 122] occurs at the top surface. Its surrounding nematic director field resembles a "classical" half-hedgehog structure. The core structure is relatively complex [74] and is schematically shown in Figure 3.18.

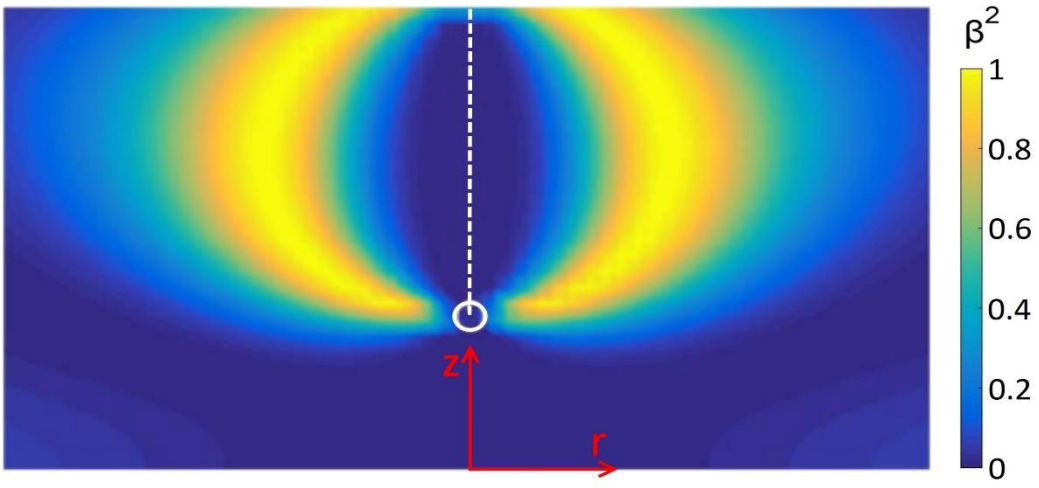

Figure 3.18: *Cross-section through a cylindrically symmetric boojum core structure.* The biaxial shell exhibiting maximal biaxiality joins the melted finger-tip with the top plate. In the case shown, the anchoring strength at the top plate is finite. The negative uniaxial region is indicated by a dashed white line. The fingertip is marked with a circle. The bar code determines the values of β^2 [121].

Its core is characterized by a negatively uniaxial finger, surrounded by a shell exhibiting maximal biaxiality $\beta^2 = 1$. The fingertip is melted due to the topology of the surroundings. To understand this let us consider ideal cylindrically symmetry, which we also adopt in our simulations. The symmetry axis of the defect is uniaxial. Namely, in terms of the parametrization defined by Eq. (2.57), the elastic free energy density includes a term that is linearly proportional with $[(3q_1 + q_2)^2 + q_3^3]/r^2$. The singularity at $r = 0$ can be avoided if uniaxial states are introduced, for which $3q_1 + q_2 = q_3 = 0$. When decreasing the value of z from the top plate, the negative uniaxiality extends to the fingertip (Figure 3.19). Below the tip, the axis is positively uniaxial. The transition from negative to positive uniaxiality requires melting of the nematic ordering in the transition area. A typical spatial variation of the director field, in the radial direction and order changes of the parameter along the symmetry axis, are depicted in Figure 3.19 [121].

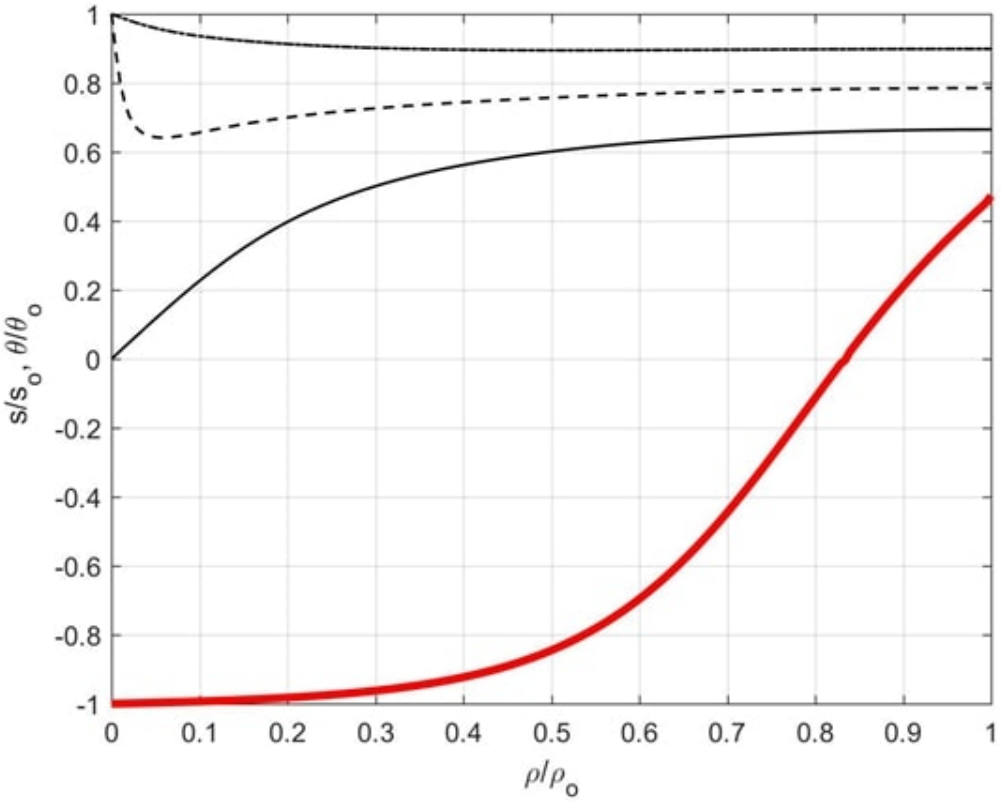

Figure 3.19: *Radial spatial variation of the director field (thin black lines,*$\rho \equiv r$, $\rho \equiv \xi_b$; $\theta_0 \equiv \pi/2$*), and degree of uniaxial order along the symmetry axis (thick red line,* $z \equiv \rho$, $\rho_0 \equiv h$; $S_0 = |S(r = 0,\ r = h)|$, $r = 0$*).* In the simulations, we establish a strong anchoring condition at the top plate $h/\xi_b = 8$, $\tau = -8$ [121].

In the given case, the fingertip (where the nematic ordering is melted) is located at $(r, z) = (0, h - \xi_f)$, where $\xi_f \approx 0.8\xi_b$. For $z > h - \xi_f$ the director field is roughly radial everywhere and $S(r = 0, z) < 0$. For $z < h - \xi_f$ the nematic order is positively uniaxial at $r = 0$ and $\boldsymbol{n} = \boldsymbol{e}_z$. With increasing r the director field monotonically increases its departure from the $z-$axis. We next apply an external electric field along the z-axis and assume that the LC possesses a negative dielectric anisotropy ($\Delta\varepsilon < 0$). In this case, the external field favors the negatively uniaxial part of the boojum. Consequently, it becomes elongated on increasing the field strength, as it is illustrated in Figure 3.20. To

achieve this, the external field must be relatively strong, i.e., $\xi_E \approx \xi_b$, which in a typical LC would correspond to $E \approx 10^8$ V/m [121].

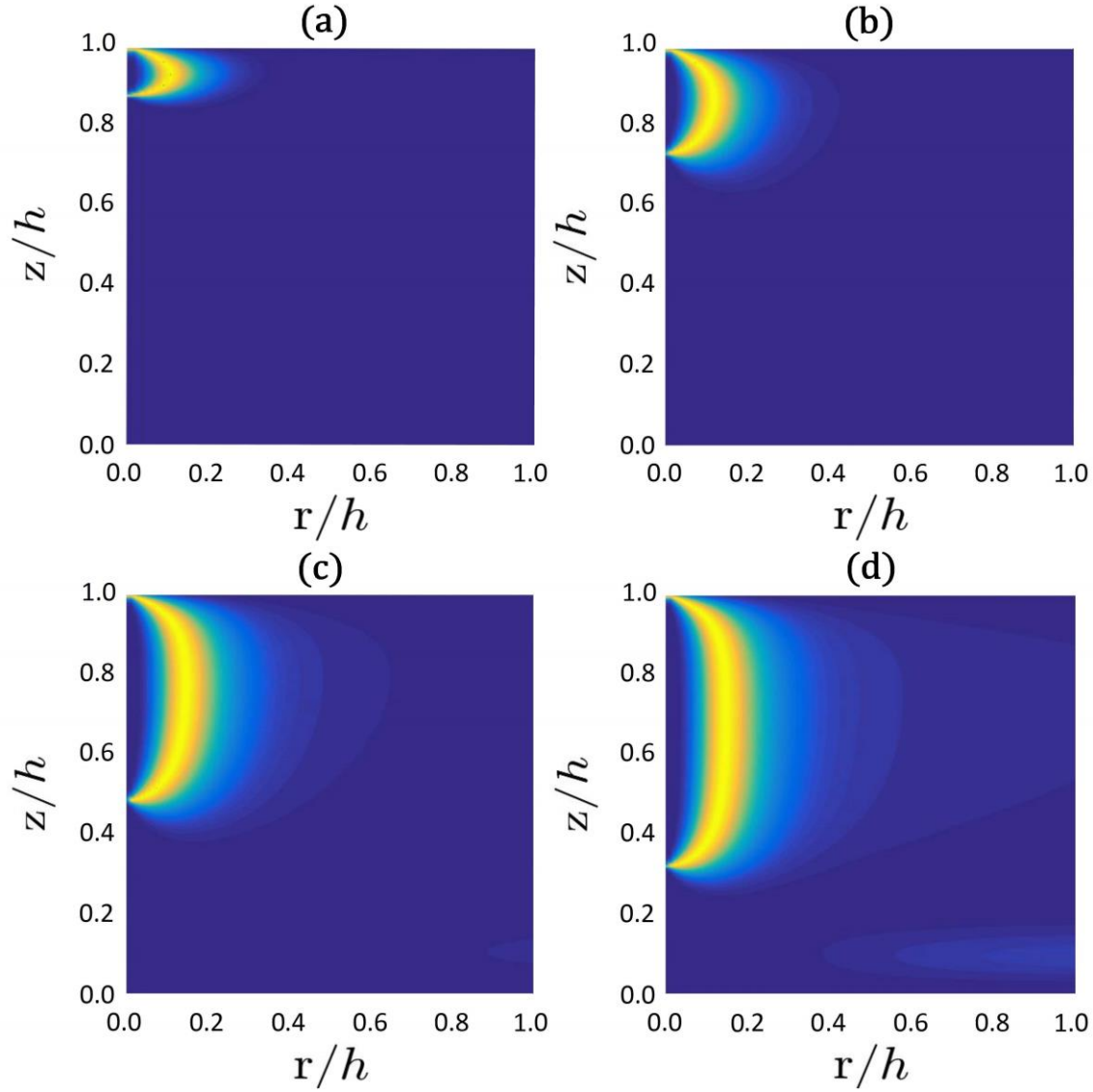

Figure 3.20: *Extension of the fingertip with an increasing external field.* Owing to the cylindrical symmetry, we plot only the right-hand part of the boojum core structure (see Figure 3.18). (a) $h/\xi_E = 0$, (b) $h/\xi_E = 8$, (c) $h/\xi_E = 10$, (d) $h/\xi_E = 12$, $h = 10\xi_b$, $h/d = 100$, $\tau = -8$ [121].

At the second stage of the investigation, our aim was to provide valuable insight into the nature of targeting of NPs towards desired locations immersed in spatially inhomogeneous nematic LC surrounding. For sake of simplicity, which does not affect the general validity of results obtained, we focus on the case in which NP exhibits a cylindrical symmetry. NP is suggested to set at an arbitrary position along the z-axis. The typical size of a NP is chosen to be comparable to the biaxial order parameter correlation length. In order to observe an influence of the surrounding boundary condition on targeting of a NP, we assume three qualitatively different its surface coatings, namely (I) melting, (II) homogeneous ordering along z-axis, (III) radial ordering. As a measure of this interaction, a mechanical force on NP is calculated. Due to the symmetry of the problem, the mechanical force is nonzero in case if it points along $\pm\boldsymbol{e}_z$ directions. The position of the

NP is varied along the z-axis, and for each position, we calculate the equilibrium nematic configuration and the corresponding mechanical force.

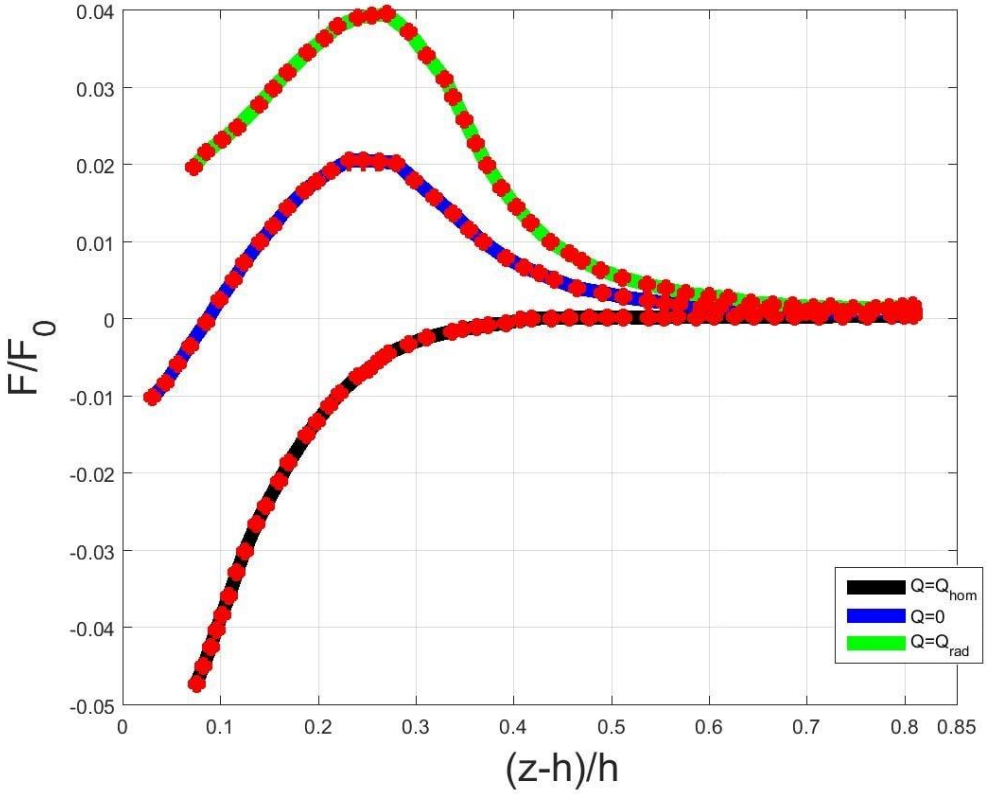

Figure 3.21: *Plot of a mechanical force F as a function of distance z. F_0* determines the reference force. The green black curve represents radial uniaxial order on the NP surface. The blue curve shows the melting of the LC order on the NP surface. The black curve represent homogenous ordering on the NP surface. The force equals zero at the boojum tip.

Figure 3.21 provides a conceptual illustration of the mechanism leading to assembling NP at locations, which exhibit similar local structure. NP surface imposing (i) melted, or (II) radial, or (III) homogeneous ordering, tend to assemble (I) at the fingertip, (II) at the plate, (III) at the bottom plate. One important conclusion follows from this: if one wants to assemble effective nanoparticles in dislocation core, the surface coating must exhibit similar local structure as the defect core structure.

3.2.4 Geometries with negative Gaussian curvature

In this Section, the impact of both the intrinsic and extrinsic curvatures on the number and position of TDs in catenoid and pseudsphere geometry is present. These structures exhibit a negative Gaussian curvature. A detailed analysis of the assembling of antidefects regions with anomalously strong curvature is given. We study also the impact of specific impurities on the assembling of TDs.

3.2.4.1 Catenoid

3.2.4.1.1 Impact of intrinsic curvature

We consider the catenoidal geometry as depicted in Figure 2.2. All lengths in our model are scaled with respect to the radius of the neck a, which represents a typical linear dimension of the film. We refer to the narrowest region of a catenoid as the equatorial ring of radius a.

At the first stage of our investigation, we consider the case in which only the intrinsic orientation elastic term $f_e^{(int)}$ is present. According to the effective charge cancellation mechanism the catenoid's surface enforces the smeared Gaussian curvature charge $\Delta m_K = 2$ at the equatorial ring. It entails creating TDs with total topological charge $\Delta m = -2$ to neutralize the surface patch.

Curvature driven formation of TDs bearing $m = -1/2$ at the equatorial ring by squeezing the catenoid's neck is shown in Figure 3.22. In column (a), we depict the catenoid's shape. Its neck is gradually squeezed on passing downwards. In the case shown in the first row, the curvature and the related nematic elastic distortions are relatively weak. Consequently, it holds $\Delta m_{eff}(\Delta\zeta) = 2$, where $\Delta\zeta$ denotes the catenoid's surface. The nematic order parameter exhibits relatively weak spatial variations, see Figure 3.22 (b). The corresponding nematic director profile is homogeneous in the (u, v) plane as shown in Figure 3.22(c). Therefore, $\boldsymbol{n}$ is aligned along parallels of the catenoid. In the Cartesian coordinates, this corresponds to concentric circles centered at the origin of the z-axis.

In the case shown in the 2nd row of Figure 3.22, elastic distortions at the neck are relatively strong and nematic ordering is almost melted at the neck area (Figure 3.22(b), 2nd row), where the distortions are strongest. However, the local curvature is still not strong enough to trigger the formation of TDs and the nematic director field is still aligned along the parallels [25].

When the critical condition is met, four $m = -1/2$ defects are created at the neck in order to compensate the smeared Gaussian curvature charge. The resulting structure exhibits zero effective topological charge and is in this sense neutral. Representative configurations are depicted in the 3rd row of Figure 3.22. At the center of the cores of TDs, the nematic order parameter is melted (Figure 3.22(b), 3rd row). The characteristic nematic director profile of defects is well visible in the 3rd row of Figure 3.22(c). In the Cartesian coordinates, this profile corresponds to the parallel alignment of $\boldsymbol{n}$ in the regions relatively far from the neck [25].

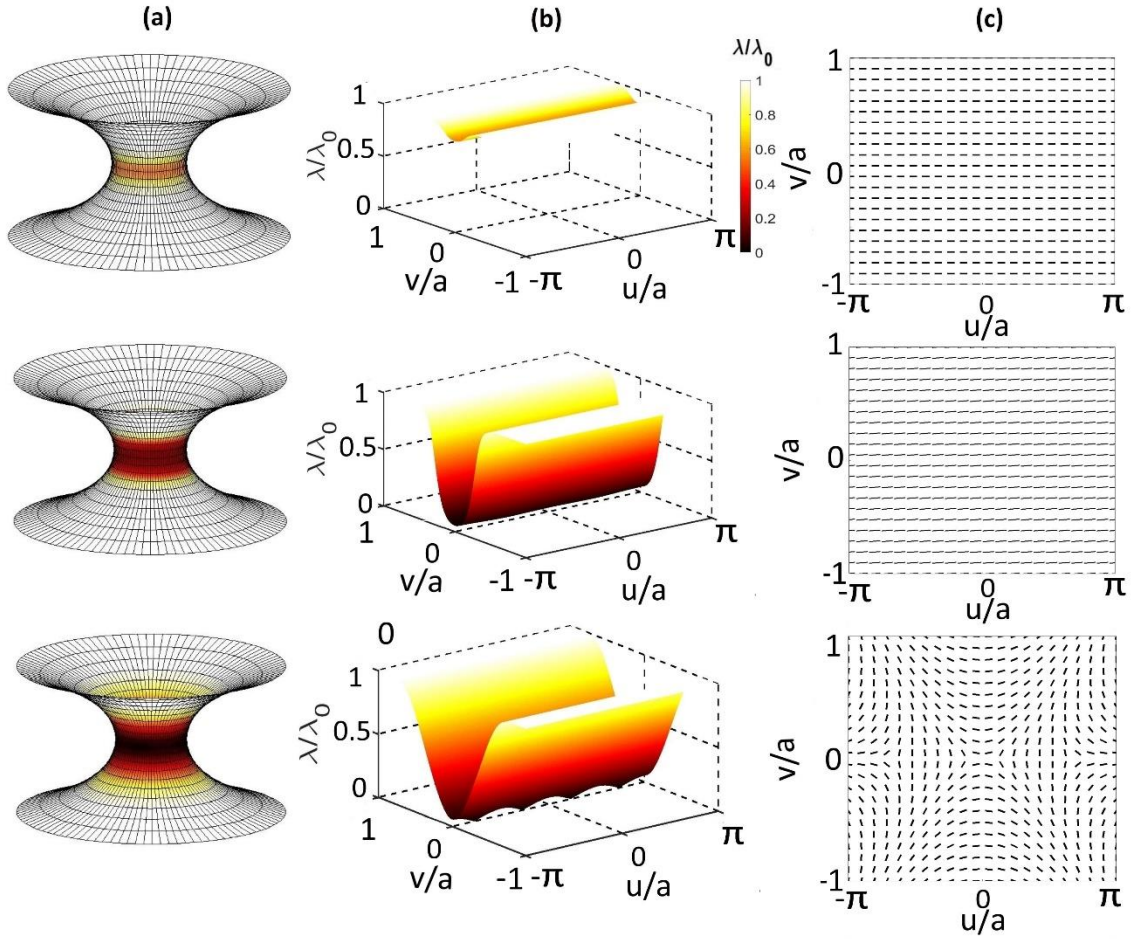

Figure 3.22: *The nematic ordering on catenoid films.* (a) Catenoid's shapes with the superimposed nematic order parameter. (b) The nematic order parameter variation in the (u, v) plane. (c) $\boldsymbol{n}$ spatial variation in the the (u, v) plane. 1st row: $a/\xi = 10$, 2nd row: $a/\xi = 1$, 3rd row: $a/\xi = 0.5$, where ξ is the nematic correlation length [25].

3.2.4.1.2 Impact of extrinsic curvature

In order to study numerically the impact of extrinsic curvature on distribution of TDs in the neck-region we include the term $f_e^{(ext)}$ in the total free energy density expansion defined by Eq. (2.41). Note that the contribution $Tr(\boldsymbol{QC}^2) \propto C_1^2 - C_2^2$ equals zero for the catenoid geometry, for which it holds $C_1 = -C_2$ [65]. Therefore, in our study, only the contribution weighted by $k_e^{(2)}$ is relevant. In our simulations, we consider the case where the only $\boldsymbol{Q}$ is variation parameter while the curvature field is imposed. In simulations, we vary a and the ratio $\mu^{(2)} = k_e^{(2)}/k_i$.

In all cases we consider catenoid possessing small enough a (i.e. comparable to ξ), so that TDs are generated. Note that for $a \gg \xi$ there are no defects. For thin enough *equatorial rings,* TDs that are created via {*defect, antidefect*}=$\{m = 1/2, m = -1/2\}$ pair formation. The *antidefects* are attracted to the *equatorial ring* where negative Gaussian curvature exhibits minimum. The *defects* are expelled outside catenoids, which is enabled in our simulations by the imposed free boundary condition. Furthermore, for catenoids it holds $\Delta m_K(\Delta\zeta) = 2$ [31], where the surface patch $\Delta\zeta$ determines the catenoid's part

exhibiting a relatively strong curvature. In Figures (3.23 and 3.24), we demonstrate the impact of $\mu^{(2)}$ on the distribution of TDs in absence of "impurities". In all cases, four $m_0 = -1/2$ are present. Consequently, the structures are *topologically neutral* (i.e. $\Delta m_{eff}(\Delta\zeta) = 0$). For $\mu^{(2)} = 0$ the effective *extrinsic ordering field* is absent. TDs are assembled at the *equatorial ring* where the Gaussian curvature exhibits the minimal value. On increasing $\mu^{(2)}$ the relative importance of the extrinsic curvature term increases. The resulting *extrinsic ordering field* is strongest at the *equatorial ring* and then monotonously decreases on increasing the distance from the *ring*. For a large enough value of $k_e^{(2)}$ TDs are expelled from the *ring*, as shown in Figure 3.23(c,d) and Figure 3.24(c,d).

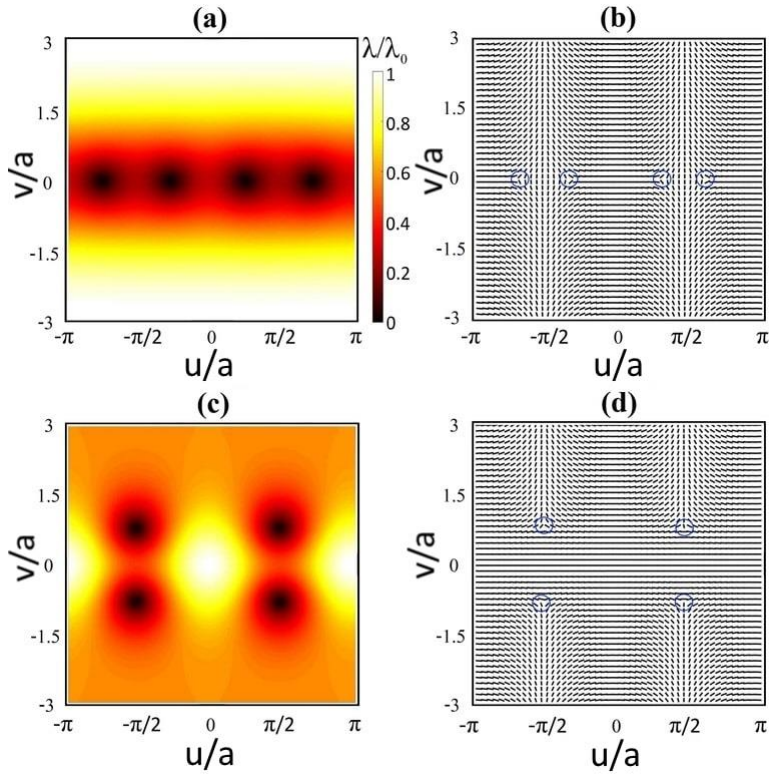

Figure 3.23: *2D Plots of the order parameter (left panel) and the director field (right panel) with decreasing the extrinsic elastic constant $k_e^{(2)}$: (a,b) $\mu^{(2)} = 0.0$, (c,d) $\mu^{(2)} = -2.4$, $a/\xi = 0.5$.* The locations of TDs are marked with blue cirles in (b) and (d) [65].

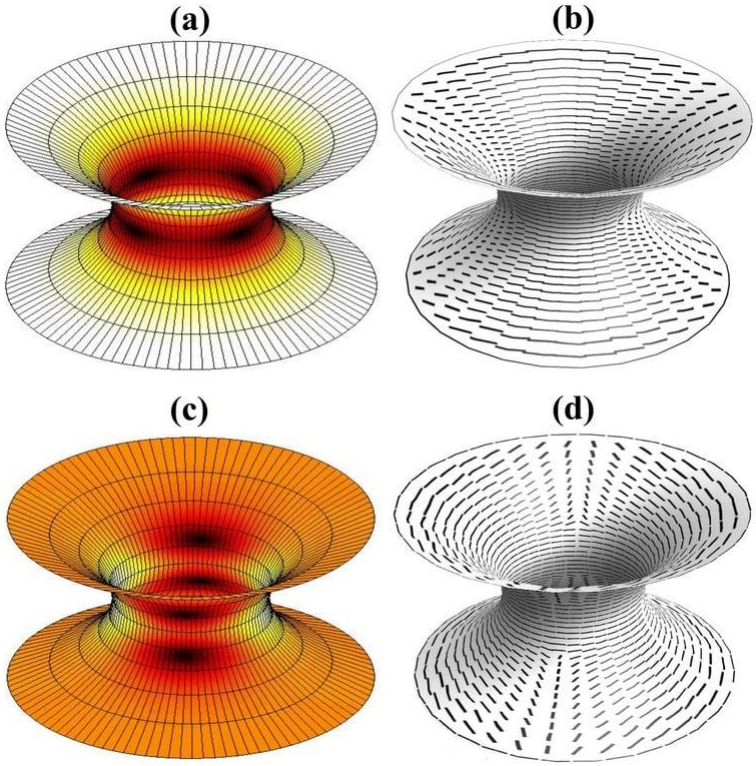

Figure 3.24: *Nematic textures on catenoidal shell upon varying the extrinsic curvature strength.* The corresponding order parameter and director field profiles in the plane (u, v) are depicted in Figure 3.23 [65].

3.2.4.1.3 Impact of impurities

Here we demonstrate the impact of the presence of specific impurities on the assembling of TDs. For this purpose, we insert circular objects of the radius $r = \xi$, which locally enforce either $\Delta m_V = 1$ or $\Delta m_V = -1$. Such conditions could be realized, e.g., by introducing an appropriately surface treated nanoparticle [123].

In Figure 3.25 we analyze the case where a fixed "impurity" enforcing $\Delta m_V = 1$ is placed within the *ring*. One sees that in this case, six $m = -1/2$ TDs exist, corresponding to topologically neutral structures. On increasing $\mu^{(2)}$, the defects redistribute. However, even for relatively large values of $k_e^{(2)}$ two $m = -1/2$ *antidefects* remain localized on the *ring*, because they are strongly pinned to the "impurity".

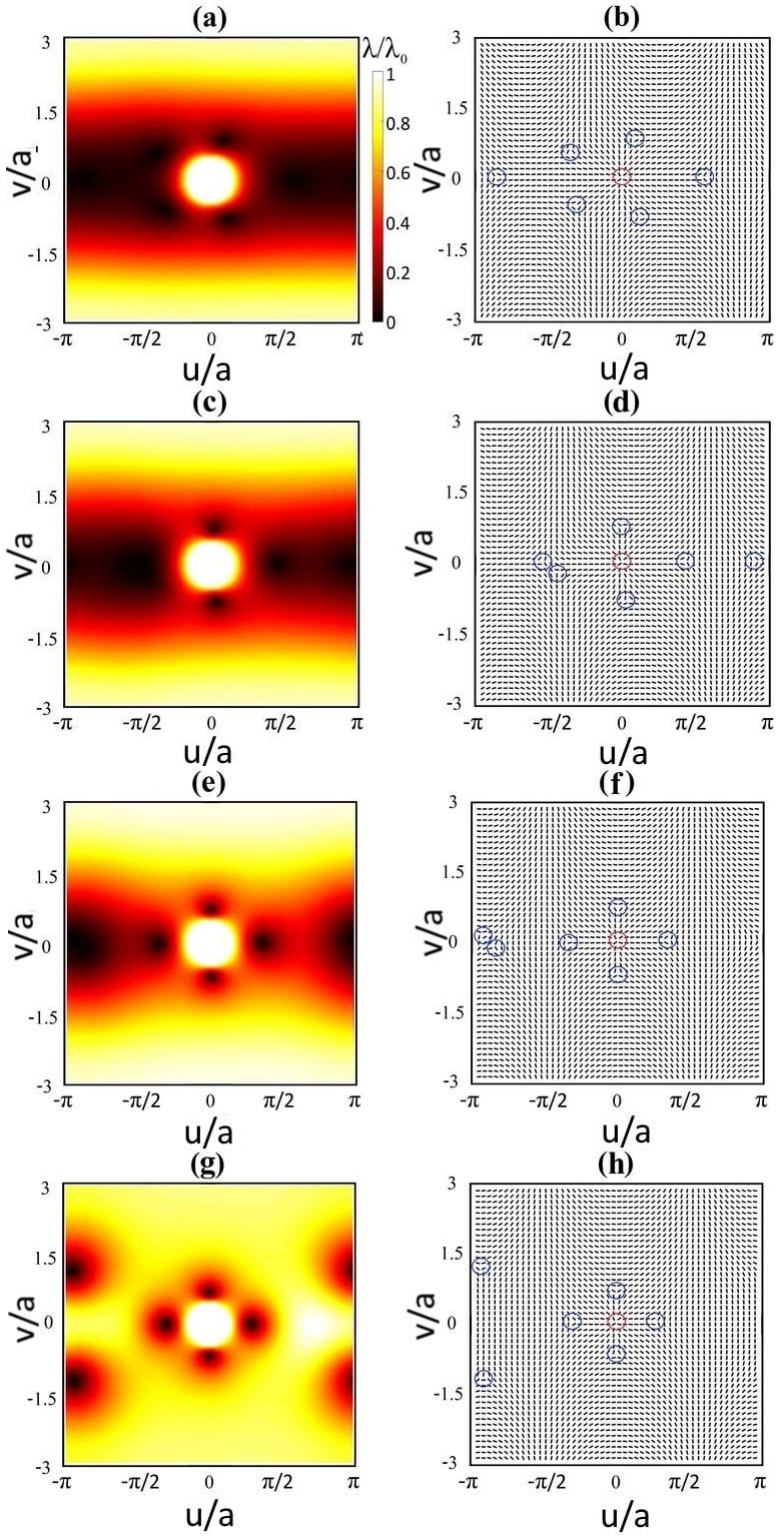

Figure 3.25: *Calculated order parameter and the director field profiles in* (u, v) *plane of the catenoid in the presence of a fixed "impurity" on varying* $k_e^{(2)}$. The order parameter and director field variations are shown in the left and right columns, respectively. The fixed circular NP of the radius $r = \xi$ is placed at $(u_{NP} = 0, v_{NP} = 0)$. The NP effectively acts as a TD bearing $\Delta m_V = 1$. Textures are obtained for (a,b): $\mu^{(2)} = 0.0$, (c,d): $\mu^{(2)} = -1$,

(e,f): $\mu^{(2)} = -2$, (g,h): $\mu^{(2)} = -2.4$, $a/\xi = 0.5$. The locations of TDs are marked with blue cirles and the nanoparticle is marked with the red circle [65].

Finally, in Figure 3.26 we consider a case where fixed "impurity" enforces $\Delta m_V = -1$. In this case, two $m = -1/2$ *antidefects* are introduced and the resulting structures are therefore *topologically neutral*. Note that on increasing $k_e^{(2)}$ the pattern of TDs does not display qualitative changes.

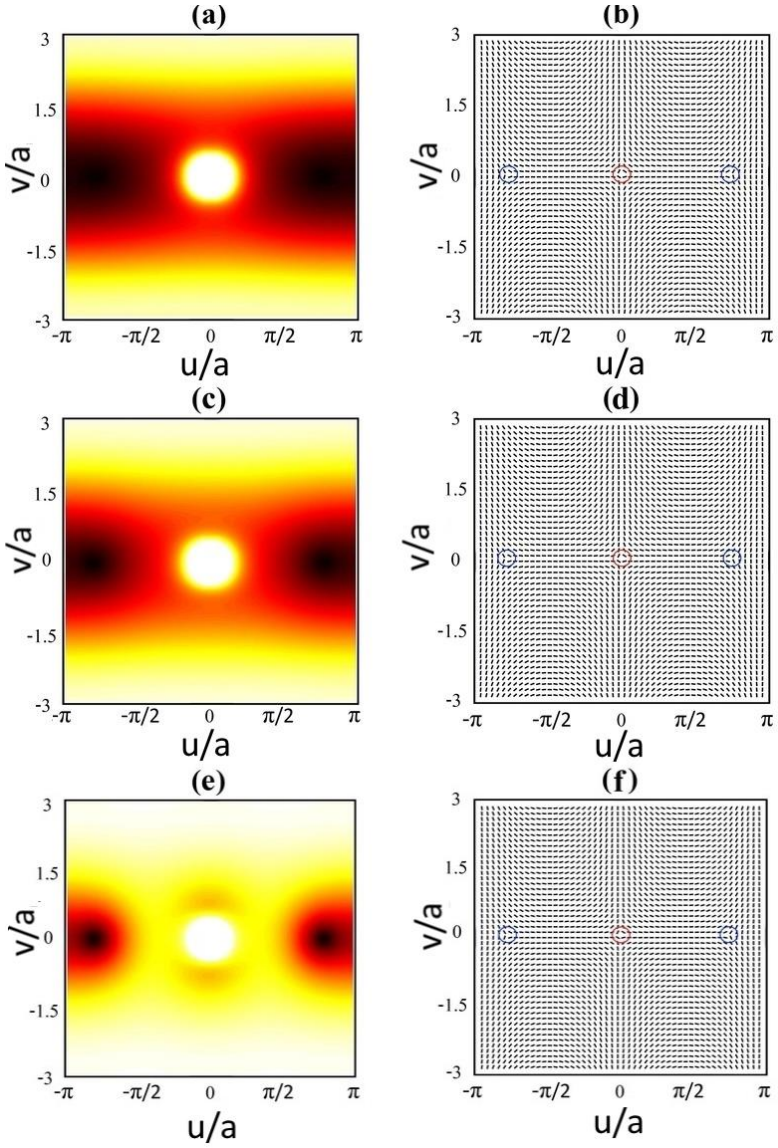

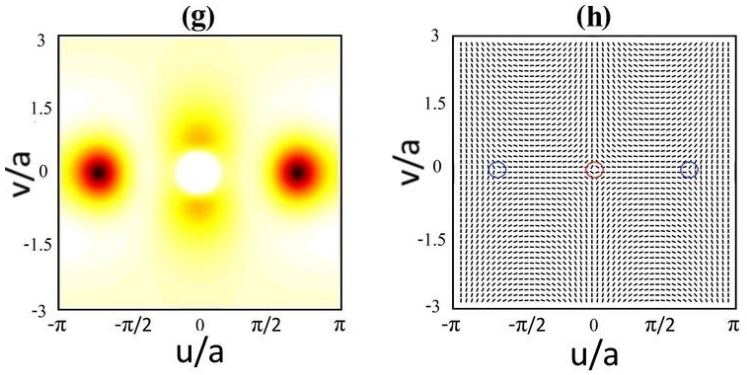

Figure 3.26: *Calculated order parameter and the director field profiles in* (u, v) *plane of the catenoid in the presence of a fixed "impurity" on varying* $k_e^{(2)}$. The order parameter and director field variations are shown in the left and right columns, respectively. The fixed circular NP of the radius $r = \xi$ is placed at $(u_{NP} = 0, v_{NP} = 0)$. The NP effectively acts as a TD bearing $\Delta m_V = 1$. Textures are obtained for (a,b): $\mu^{(2)} = 0.0$, (c,d): $\mu^{(2)} = -1$, (e,f): $\mu^{(2)} = -2$, (g,h): $\mu^{(2)} = -2.4$, $a/\xi = 0.5$. The locations of TDs are marked with blue cirles and the nanoparticle is marked with the red circle [65].

3.2.4.2 Pseudosphere

We next consider a pseudosphere with a radius a. In this case, the principal curvatures are not equal. It implies that its mean curvature is not minimal. Therefore, in this case by the first term in $f_e^{(ext)}$ is finite, see Eq. (2.41). In simulations, we vary the ratio $\mu^{(1)} = k_e^{(1)}/k_i$. Corresponding numerically calculated order parameter textures and director profiles are present in the 2D plane and on the pseudospheric film, depicted in Figure 3.27 and Figure 3.28, respectively.

In Figure 3.27 the left column indicates the order parameter, whereas the right column represents the corresponding nematic director field profiles. The extrinsic field strength is gradually increasing on passing downwards. Firstly, we consider $\mu^{(1)}$ to be equal to zero, i.e., only the extrinsic contribution is present. This case is shown in the first row. The nematic order parameter texture exhibits a layer with a large spatial variation broaden along the singular boundary of the surface. The corresponding nematic order field profile reveals that the structure has the topological charge bearing $\Delta m = -1$. At the tip, the nematic order parameter exhibits relatively weak spatial variations and the corresponding $\boldsymbol{n}$ profile is homogenous in the (u, v) plane and aligned along meridians of the pseudosphere.

The second row (c,d) reflects the case when extrinsic curvature is present. As a consequence, the TD located at the boundary splits into two $m = -1/2$. They begin to repel each other and move along the meridians, direction in which the extrinsic term is enforced. In addition to that, one can see that a pair of positive defects appears near the tips of the surface.

In the case shown in the third row (e,f) one sees that defects and antidefects approach each other on increasing the strength of the extrinsic contribution. Finally, the case depicted at the fourth row (g,h) indicates an appearing two defect walls, connecting the two orthogonal directions. Due to this, the central part including the singular boundary

exhibit the defectless state. This transition corresponds to the reconstruction of the nematic order.

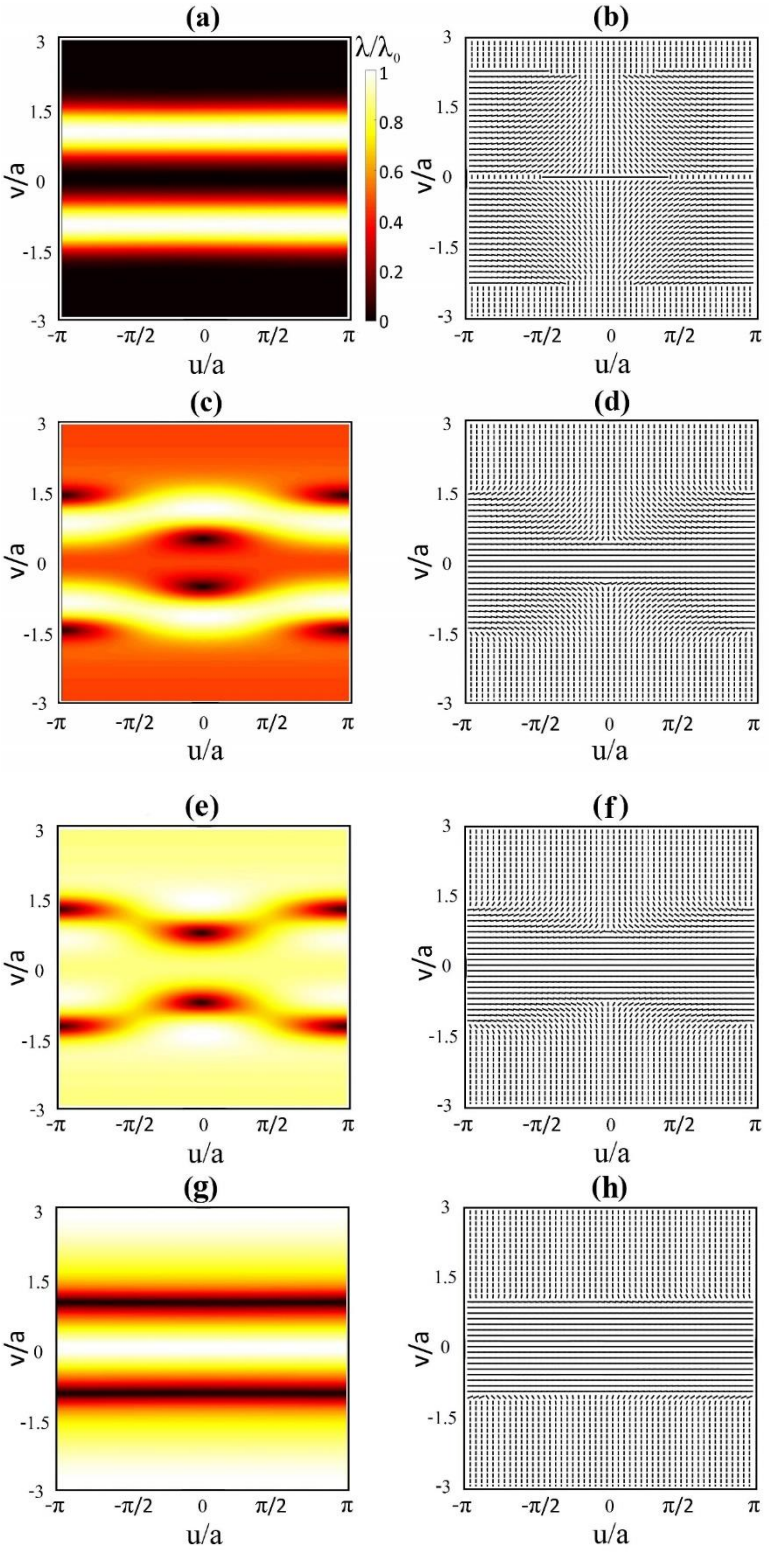

Figure 3.27: *The spatial variations of the scalar order parameter (left column) and correcponding director field profiles (right column) in the plane* (u, v) *with increasing the extrinsic elastic constant* $\mu^{(1)}$. Textures are obtained for (a,b): $\mu^{(1)} = 0.0$, (c,d): $\mu^{(1)} = 0.04$, (e,f): $\mu^{(1)} = 1$, (g,h): $\mu^{(1)} = 1.5$, $a/\xi = 5$, $\tau = -0.5$.

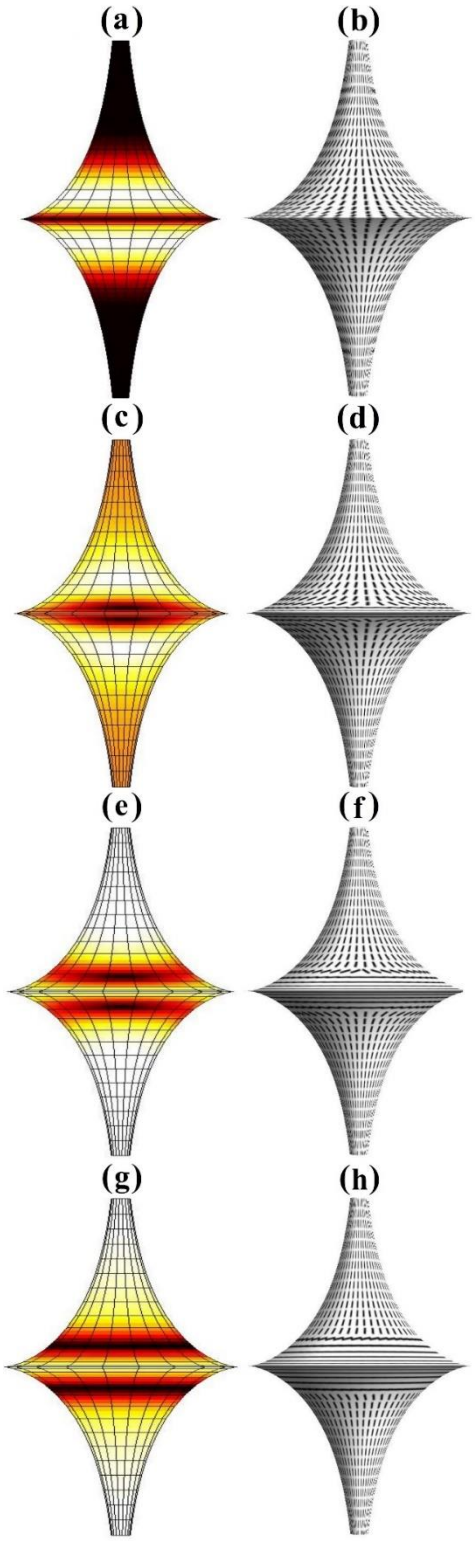

Figure 3.28: *Nematic textures on open ordered film upon increasing the extrinsic elastic constant* $\mu^{(1)}$. The corresponding order parameter and director field profiles in the plane (u, v) are depicted in Figure 3.27.

Chapter 4

Conclusions

In the thesis, we consider static and dynamic phenomena in frustrated nematic LCs. In our theoretical and numerical analysis, we used mesoscopic Landau-de Gennes type modeling and semi-microscopic Lebwohl-Lasher lattice approach. Of our interest were fundamental frustration driven mechanisms, which are of interest also to other branches of physics. We used nematic LCs as a demonstrative system. Namely, in them such phenomena could be relatively easy tested due to their experimental accessibility. At the mesoscopic level, we described nematic orientational order with the nematic tensor order parameter. We studied both the 2D in 3D systems. In the former cases, we studied also curved geometries, which we described with curvature fields. In our semi-microscopic studies, we considered rod-like objects interacting via the Lebwohl-Lasher interaction, where nematic "molecules" occupied cubic lattice sites.

In the main part of our study, we focused on topologically generated TDs. We analysed systems, which could be realized using existing sample preparation technologies and relatively simple measuring methods. For example, experimental set-ups of all studied cases could be realized using the AFM scribing technology recently developed by C. Rosenblatt group [11, 12]. In this approach, an arbitrary pattern could be scribed onto the "master" plate of a plane-parallel cell using an AFM tip. If TDs are enforced then the master surface imposed defect sites are separated for few microns. The second confining substrate, the so-called "slave" plate, enforces isotropic tangential anchoring. Consequently, in thin enough geometries nematic structures within such cells are dominantly influenced by master plates. In these cases, samples display effectively 2D behaviour.

We first considered planar nematic films where we assumed that nematic LCs are confined within relatively thin plane-parallel cells where we neglected spatial variations along the cell thickness. In these cases, we modeled nematic order with the 3D nematic tensor order parameter. We focused on analogies with electrostatics. We studied nematics confined within a circle which enforces a relatively high total winding number $m_{tot} >> 1$. The radius of circles was large with respect to the biaxial nematic order parameter length. In such case, elementary TDs are formed, each bearing $m_0 = 1/2$, where the number of TDs equals to $N = m_{tot}\ /m_0$. All TDs assembled at the confining boundary. Our simulations reveal [122] that on increasing N the central region increasingly exhibits ground state bulk nematic ordering. This phenomenon is analogous to the Faraday cavity effect in electrostatics. Namely, in the latter cases, electric charges assemble at the outer boundary of a conductor in order to cancel the electric field within it. We also demonstrated [122] that effective rotations of assemblies of TDs could be enforced by changing the temperature in asymmetric confinement geometries. Furthermore, TDs could be exploited as efficient traps for appropriate nanoparticles. Our analysis reveals that if they locally favour isotropic anchoring then they are attracted to cores of defects [122]. We have demonstrated that one could precisely control the position of the melted fingertip in a boojum topological defect.

For such purposes, one needs nematic with negative electric anisotropy. In such materials, an appropriately applied external electric field tends to enlarge the boojum finger length. Consequently, the position of the fingertip, where a NP could be trapped, can be sensitively controlled.

Then we considered nematic structure within a rectangular boundary imposing locally strong tangential anchoring. The common belief is that such boundary condition enforces the total winding number m_{tot} to the enclosed nematic phase. However, we have proven, that due to sharp edges within the confining boundary m_{tot} is not uniquely defined. For the rectangular confinement m_{tot} could be equal either to 1, -1, 1/2, -1/2, or 0. Our numerical simulations confirmed this claim. We obtained topologically different structures for the same boundary condition. Furthermore, we showed that one could switch among different topologies using an external electric field $\boldsymbol{E}$. Namely, we demonstrated that using a strong enough $\boldsymbol{E}$ a topological charge could be absorbed by an edge, where the nematic orientation exhibits discontinuous change. In such a way, we realized a topological change without melting. We also considered nematic structures within the rectangular confinement, where we in addition enforced a pair of point defects $\{$*defect, antidefect*$\}$ bearing winding number $\{3/2, -3/2\}$ by a surface anchoring field of finite strength. Such a field could be realised, e.g., using the AFM scribing method. In this case, each of the enforced defects decayed into elementary defects characterised by $m_0 = \pm 1/2$. We studied different mechanisms enabling annihilation of these defects into a defectless state. We enforced annihilation either by applying a strong enough spatially uniform external electric field or by decreasing the strength of the surface anchoring field. Both cases could be relatively easily realized experimentally. For example, one could effectively reduce the relative importance of the surface anchoring strength on approaching a second order nematic-smectic A phase transition. In this case, the bend elastic constant tends to diverge, penalizing structures possessing regions exhibiting bend elastic deformation. Such regions are present if a structure contains pairs of TDs in our setting. Furthermore, we showed that annihilation scenario are strongly susceptible to various perturbations.

Afterwards, we analysed the impact of curved substrates on nematic ordering and TDs within them [25, 64]. In these studies, we modeled orientational order with the 2D nematic tensor order parameter. We characterized curvatures by curvature fields, where the dominant role was played by the Gaussian curvature and the mean curvature. Particular emphasis was put on the role the extrinsic curvature that has been in most studies so far neglected. Namely, common 2D XY-type models rely on covariant derivatives, which allow only the intrinsic curvature terms. However, a simple analysis reveals that in general, both intrinsic and extrinsic contributions should be present. Their relative importance depends on the material properties of systems. In fact, pioneering investigations of impacts of extrinsic curvature have been carried out in studies of membranes, in which they are referred to as deviatoric curvature. We showed that in nematics two qualitatively different symmetry allowed extrinsic elastic contributions are present in free energy density ($f_e^{(ext,1)}$ and $f_e^{(ext,2)}$), which are proportional with $C_1^2 - C_2^2$ or $(C_1 - C_2)^2$, respectively. We first considered catenoid shapes, characterised by $C_1 = -C_2$ in which only $f_e^{(ext,2)}$ is present. In particular, such shapes are often present in biological structures where configurations exhibiting neck-like segments are present. For example, these are inevitable present in membrane fission, fusion or budding processes. If curvature at the catenoid's neck is strong enough four $m = -1/2$ are formed in order to "screen" completely strongly localised negative Gaussian curvature. This phenomenon is well described by the Effective Topological Charge Cancelation (ETCC) mechanism, which claims that the effective charge within each region characterised with the average Gaussian curvature, tends to be neutralised. In catenoids, the so called curvature topological charge equals two. For this

reason, four $m_0 = -1/2$ TDs need to be introduced to neutralize the catenoid's neck region. The relative importance of intrinsic and extrinsic contributions is measured by the ratio $\mu^{(2)} = k_i/k_e^{(2)}$. For a relatively low value of $\mu^{(2)}$ the defects are localised at the neck ring. If $\mu^{(2)}$ exceeds the critical value (which is temperature dependent), the defects are expelled from the ring region but remains localised in the neck region. However, in either case, the ETCC mechanism is obeyed for thin enough necks. To demonstrate the robustness of the ETCC mechanism we inserted also "impurities" at the neck ring, which effectively act as TDs bearing winding number $m = 1$ or $m = -1$. In these cases, additional pairs $\{defect, antidefect\}$ appear in order to neutralize the neck. We also analysed the impact of the extrinsic curvature on pseudospheres. In addition, in this case, the ETCC mechanism is obeyed. However, we observed qualitatively different behaviour on varying the relative importance of the extrinsic contribution, where planar order reconstruction planes were introduced to relieve local frustrations.

We also studied tumbling dynamics within a plane-parallel nematic cell within the semi-macroscopic lattice approach. By using appropriate surface boundary conditions, we could obtain tumbling-like dynamics if an external rotating field $\boldsymbol{B}$ was present. We analysed behaviour on increasing the frequency of the field for appropriate $\boldsymbol{B}$ value. In the limit of a low and high frequency, the nematic structure was collectively following $\boldsymbol{B}$ or remained locked along a symmetry breaking direction. Our analysis revealed that on increasing the external field frequency the transition between these extreme states was realised by a period doubling-like process.

In Summary, we emphasize the following main novelties introduced by our investigations.

(I) We demonstrated phenomenon analogous to the Faraday cavity effects in electrostatics. We showed that TDs tend to assemble at a confining boundary, which enforces topological relatively large topological charge. In such a way, the ground state-like configuration is established in the main part of the confined nematic LC.

(II) For appropriate asymmetric boundary conditions, one could enforce synchronized collective motion of TDs by varying temperature close to the isotropic-nematic phase transition.

(III) We proved that fixed boundary conditions could enforce different total winding number to the confined 2D nematic LC if the confining boundary exhibits sharp edges. Furthermore, transitions among topologically different states could be enforced without melting.

(IV) We demonstrated that an external electric field driven 2D structural transitions could be realised continuously by forming or annihilation of pairs {*defect, antidefect*}.

(V) We showed that surface imposed pairs {*defect, antidefect*} in 2D could be efficiently annihilated by tuning an appropriate control parameter, which enforces spatially homogeneous ordering. Furthermore, details of annihilation processes are relatively strongly susceptible to various perturbations.

(VI) In curved 2D geometries, possessing neck-like regions, extrinsic curvature strongly affects the position of TDs if they are generated by strong enough local curvature.

(VII) In 3D confined nematic LCs, we demonstrated that TDs could be exploited to manipulate precisely (nm scale) position of appropriately surface treated NPs by an external electric field.

(VIII) In confined geometries, which enable tumbling dynamics, transitions between qualitatively different states are realised via a period doubling-like process.

References

[1] Kleman M, Lavrentovich O. *Soft Matter Physics: An introducion*. New York: Springer; 2003.

[2] Mermin N. The topological theory of defects in ordered media. *Rev. Mod. Phys.* 1979;51;591-648.

[3] Zurek WH. Cosmological experiments in superfluid helium? *Nature*. 1985;317: 505–508.

[4] Skyrme THR. A unified field theory of mesons and baryons. *Nucl. Phys.* 1962;31:556-569.

[5] Hobson A. There are no particles, there are only fields. *Am. J. Phys.*2013;81:211-223.

[6] Chaikin P, Lubensky T. *Principles of condensed matter physics*. Cambridge, New York: Cambridge University Press; 1995.

[7] Chandrasekhar S. *Liquid Crystals*. Cambridge: Cambridge University Press; 1992.

[8] Gennes P, Prost J. *The physics of liquid crystals*. Oxford: Clarendon Press; 1993.

[9] Stephen MJ, Straley JP. Physics of liquid crystals. *Rev. Mod. Phys.*1974;46: 617-704.

[10] Kosterlitz JM. Nobel Lecture: Topological defects and phase transitions. *Rev. Mod. Phys.* 2017;89(4):040501(1-7).

[11] Murray BS, Pelcovits RA, Rosenblatt C. Creating arbitrary arrays of two-dimensional topological defects. *Phys. Rev. E.* 2014; 90(5):052501(1-6).

[12] Kralj S, Murray BS, Rosenblatt C. Decomposition of strongly charged topological defects. *Phys. Rev. E.* 2017;95(4):042702(1-9).

[13] Vitelli V, Nelson DR. Nematic textures in spherical shells. *Phys. Rev E.* 2006;74(2):021711(1-18).

[14] Nelson DR. Toward a tetravalent chemistry of colloids. *Nano Lett.* 2002;2(10):1125-1129

[15] Skačej G, Zannoni C. Controlling surface defect valence in colloids. *Phys. Rev. Lett.* 2008;100(19):197802(1-4).

[16] Shin H, Bowick MJ, Xing X. Topological defects in spherical nematics. *Phys. Rev Lett.* 2008;101(3):037802(1-4).

[17] Kralj S, Rosso R, Virga EG. Curvature control of valence on nematic shells. *Soft Matter.* 2011;7(2):670-683.

[18] Vitelli V, Turner AM. Anomalous coupling between topological defects and curvature. *Phys. Rev. Lett.* 2004;93(21):215301(1-4).

[19] Kralj S, Rosso R, Virga EG. Finite-size effects on order reconstruction around nematic defects. *Phys. Rev. E.* 2010;81(2):021702.

[20] MacKintosh FC, Lubensky TC. Orientational order, topology, and vesicle shapes. *Phys. Rev. Lett.* 1991;67(9):1169-1172.

[21] Kamien RD. The geometry of soft materials: a primer. *Rev. Mod. Phys.* 2002; 74(4):953-971.

[22] Kusumaatmaja H, Wales DJ. Defect Motifs for Constant Mean Curvature Surfaces. *Phys. Rev. Lett.* 2013;110(16):165502(1-5).

[23] G. Napoli, Vergori L. Surface free energies for nematic shells. *Phys. Rev. E.* 2012;85(6):061701.

[24] Bowick MJ, Giomi L. Two-dimensional matter: order, curvature and defects. *Advances in Physics.* 2009;58(5):449–563.

[25] Mesarec L, Kurioz P, Iglič A, Góźdź W, Kralj S. Curvature-Controlled Topological Defects. *Crystals.* 2017;7(6):153(1-11).

[26] Santiago JA, Chacón-Acosta G, González-Gaxiola O. Effective potentials in geodesic curves on surfaces. *J. Phys. Conf.* 2014;545:012014(1-5).

[27] Amar MB, Müller MM, Trejo M. Petal shapes of sympetalous flowers: the interplay between growth, geometry and elasticity. *New J. Phys.* 2012;14;085014 (1-14).

[28] Iorio A, Lambiase G. Quantum field theory in curved graphene spacetimes, Lobachevsky geometry, Weyl symmetry, Hawking effect, and all that. *Phys. Rev. D.* 2014;90(2):025006(1-28).

[29] Iorio A. Curved spacetimes and curved graphene: A status report of the Weyl symmetry approach *Int. J. Mod. Phys. D.* 2015;24(5):1530013(1-64).

[30] Kikuchi H, Yokota M, Hisakado M, Yang H, Kajiyama T. Polymer-stabilized liquid crystal blue phases. *Nat. Mater.* 2002;1(1):64-68.

[31] Mbanga BL, Grason GM, Santangelo CD. Frustrated order on extrinsic geometries. *Phys. Rev. Lett.* 2012;108(1):017801(1-5).

[32] Karatairi E, Rožič B, Kutnjak Z, Tzitzios V, Nounesis G, Cordoyiannis G, Thoen J, Glorieux C, Kralj S. Nanoparticle-induced widening of the temperature range of liquid-crystalline blue phases. *Phys. Rev. E.* 2010;81(4):041703(1-5).

[33] Coursault D, Grand J, Zappone B, Ayeb H, Levi G, Felidj N, Lacaze E. Linear self-assembly of nanoparticles within liquid crystal defect arrays. *Adv. Mater.* 2012;24(11):1461-1465.

[34] Hilborn RC. *Chaos and Nonlinear Dynamic.* Norfolk: Oxford university press; 2000.

[35] Waldner F, Barberis BS, Yamazaki H. Route to chaos by irregular periods: Simulations of parallel pumping in ferromagnets. *Phys. Rev. A,* 1985;31(1):420-431.

[36] Eckmann JP. Roads to turbulence in dissipative dynamical systems. *Rev. Mod. Phys.* 1981;53(4):643-654.

[37] Lindsay P. Period Doubling and Chaotic Behavior in a Driven Anharmonic Oscillator. *Phys. Rev. Lett.* 1981;47(19):1349-1352.

[38] Testa J, Pérez J, Jeffries C. Chaotic Behavior of a Driven Nonlinear Oscillator. *Phys. Rev. Lett.* 1982;48(11):714-717.

[39] Echebarria B, Karma A. Instability and spatiotemporal dynamics of alternans in paced cardiac tissue. *Phys. Rev. Lett.* 2002;88(20):208101(1-4).

[40] Echebarria B, Karma A. Amplitude equation approach to spatiotemporal dynamics of cardiac alternans. *Phys. Rev. E.* 2007;76(5):051911(1-23).

[41] Morris HC. *Nonlinear Structures in Physical Systems.* New York: Springer; 1989.

[42] Song JW, Lee HY, Shin SY, Kwon YS. Periodic window, period doubling, and chaos in a liquid crystal bistable optical device. *Appl. Phys. Lett.* 1983;43 (1):14-16.

[43] Kim KJ, Araoka F, Jeong MS, Dhara S, Ishikawa K, Takezoe H.Bistable device using anchoring transition of nematic liquid crystals. *Appl. Phys. Lett.* 2009;95(6):063505(1-3).

[44] Cladis PE, Torza S. Stability of Nematic Liquid Crystals in Couette Flow. *Phys. Rev. Lett.* 1975;35(19):1283-1286.

[45] Manneville P. The Transition to Turbulence in Nematic Liquid Crystals. *Mol. Cryst. and Liq. Cryst.* 1981;70(1):223-250.

[46] Cordoyiannis G, Jampani VSR, Kralj S, Dhara S, Tzitzio V, Basina G, Nounesis G, Kutnjak Z, Tripathi CSP, Losada-Perez P, Jesenek D, Glorieux C, Musevič I, Zidanšek A, Amenitsch H, Thoen J.Different modulated structures of topological defects stabilized by adaptive targeting nanoparticles. *Soft matter.* 2013;9(15):3956-3964.

[47] Knitter S, Liew SF, Xiong W, Guy MI, Solomon GS, Cao H. Topological defect lasers", *J. Opt.* 2016;18:014005 (1-5).

[48] Wang X, Kim YK, Bukusoglu E, Zhang B, Miller DS, Abbott NL. Experimental Insights into the Nanostructure of the Cores of Topological Defects in Liquid Crystals. *Phys. Rev. Lett.* 2016;116(14):147801 (1-5).

[49] Satiro C, Moraes F. Lensing effects in a nematic liquid crystal with topological defects. *Eur. Phys. J. E.* 2006;20(2):173-178.

[50] Manyuhina OV, Laelor KB, Marchetti MC, Bowick MJ. Viral nematics in confined geometries. *Soft Matter.* 2015;11(30):6099-6105.

[51] Zimmerberg J, Kozlov MM. How proteins produce cellular membrane curvature. *Nat. Rev. Mol. Cell Biol.* 2006; 7(1):9–19.

[52] Giblin JT, Mertens JB, Starkman GB. Departures from the Friedmann-Lemaitre-Robertston-Walker cosmological model in an inhomogeneous universe: A numerical examination. *Phys. Rev. Lett.* 2016;116(25):251301(1-5).

[53] Lebwohl PA, Lasher G. Nematic-Liquid-Crystal Order—A Monte Carlo Calculation. *Phys. Rev. A.* 1972;6(1):426-429.

[54] Maier W, Saupe A. Eine eifache molekulare theorie des nematischen kristallinflussigen zustandes. *Zeits. fur Naturf. A.* 1958;13:564-566.

[55] Cleaver DJ, Allen MP. Computer simulation of liquid crystal films. *Mol. Phys.* 1993;80(2):253-27.

[56] Almarza NG, Martín C, Lomba E. Phase behavior of the confined Lebwohl-Lasher model. *Phys. Rev. E.* 2010;82(1):011140(1-8).

[57] Chiccoli C, Pasini P, Sarlah A, Zannoni C, Žumer S. Structures and transitions in thin hybrid nematic films: A Monte Carlo study. *Phys. Rev. E.* 2003;67(5):050703(1-4).

[58] Chiccoli C, Gouripeddi SP, Pasini P, Murthy RPN, Sastry VSS, Zannoni C. Hybrid Nematic Films: A Detailed Monte Carlo Investigation. *Mol. Cryst. Liq. Cryst.* 2009;500(1):118-131.

[59] Blinov L. *Structure and Properties of Liquid Crystals.* Heidelberg: Springer; 2011.

[60] Carbone G, Rosenblatt C. Polar Anchoring Strength of a Tilted Nematic: Confirmation of the Dual Easy Axis Model. *Phys. Rev. Lett.* 2005;94(5):057802 (1-4).

[61] Kralj-Iglič V, Heinrich V, Svetina S, Žekš B. Free energy of closed membrane with anisotropic inclusions. *Eur. Phys. J. B.* 1999;10(1):5–8.

[62] Helfrich W. Elastic properties of lipid bilayers: theory and possible experiments. *Z Naturforsch C.* 1973;28(11):693-703.

[63] Rosso R, Virga EG, Kralj S. Parallel transport and defects on nematic shells. *Continuum Mech. Therm.* 2012;24(4-6):643-664.

[64] Kralj S, Mesarec L, Kurioz P, Rzoska S, Iglič A. Topological Defects: From Simplicity to Complexity. *GJSFR-A.* 2017;17(3):23-43.

[65] Kurioz P, Mesarec L, Iglič A, Kralj S. Assembling of Topological Defects at Neck-Shaped Membrane Parts [published ahead of print January 21, 2019]. *Phys. Status Solidi A.* 2019;1:1800722(1-10).

[66] Napoli G, Vergori L. Surface free energies for nematic shells. *Phys. Rev. E.* 2012;85(6):061701(1-12).

[67] Bowick M, Nelson DR, Travesset A. Curvature-induced defect unbinding in toroidal geometries. *Phys. Rev. E.* 2004;69(4):041102(1-12).

[68] Jesenek D, Kralj S, Rosso R, Virga EG. Defect unbinding on a toroidal nematic shell. *Soft Matter.* 2015;11(12):2434–2444.

[69] Mesarec L, Góźdź W, Iglič A, Kralj S. Effective Topological Charge Cancelation Mechanism. *Sci. Rep.* 2016;6(1):27117(1-12).

[70] Kralj S, Virga EG. Universal fine structure of nematic hedgehogs. *J. Phys. A: Math. Gen.* 2001;34(4):829–838.

[71] Nobili M, Durand G. Disorientation-induced disordering at a nematic-liquid-crystal-solid interface. *Phys. Rev. A.* 1992;46 (10):R6174- R6177.

[72] Kralj S, Virga EG, Žumer S. Biaxial torus around nematic point defects. *Phys. Rev. E.* 1999;60(2):1858-1866.

[73] Bisi F, Gartland EC, Rosso R, Virga EG. Order reconstruction in frustrated nematic twist cells. *Phys. Rev. E.* 2003;68(2):021707(1-10).

[74] Kralj S, Rosso R, Virga EG. Fingered core structure of nematic boojums. *Phys. Rev. E.* 2008;78(3):031701(1-4).

[75] Schopohl N, Sluckin TJ. Defect Core Structure in Nematic Liquid Crystals. *Phys. Rev. Lett.* 1987;59(22):2582–2584.

[76] Kaiser P, Wiese W, Hess S. Stability and Instability of a Uniaxial Alignment Against Biaxial Distortions in the Isotropic and Nematic Phases of Liquid Crystals. *J. Non-Equilib. Thermodyn.* 1992;17(2):153-170.

[77] Hohenberg PC, Halperin BI. Theory of dynamic critical phenomena. *Rev.Mod.Phys.* 1977;49(3):435-479.

[78] Fukuda J, Yokoyama H. Director configuration and dynamics of a nematic liquid crystal around a two-dimensional spherical particle: Numerical analysis using adaptive grids. *Eur. Phys. J. E.* 2001;4:389-396.

[79] Kralj S, Majumdar A. Order reconstruction patterns in nematic liquid crystal wells. *Proc. R. Soc. A.* 2014;470:20140276(1-18).

[80] Repnik R, Nita VN, Kralj S. Mixtures of Nanoparticles and Liquid Crystal Phases Exhibiting Topological Defects. *Mol. Cryst. and Liq. Cryst.* 2012;560(1):115-122.

[81] Dubtsov AV, Pasechnik SV, Shmeliova DV, Kralj S, Repnik R. Controlled Nanoparticle Targeting and Nanoparticle-Driven Nematic Structural Transition. *Adv. in Cond. Matt. Phys.* 2015;803480:1-9.

[82] Blaschke W, Leichtweiss K. *Elementare Differentialgeometrie*. Berlin-Heidelberg: Springer; 1973.

[83] Klingenberg W. *A course in differential geometry*. New York: Springer; 1978.

[84] Baer C. *Elementary Differential Geometr*y. New York: Cambridge Univ. Press; 2011.

[85] Iglič A, Kralj-Iglič V. Izbrana poglavja iz fizike mehke snovi. Ljubljana: Fakulteta za elektrotehniko; 2006.

[86] Kurik MV, Lavrentovich OD. Defects in liquid crystals: homotopy theory and experimental studies. *Sov. Phys. Uspekhi.* 1988;31(3):196–224.

[87] Spivak M. *A comprehensive introduction to differential geometry*. Volume II, Publish or Perish Press; 1999

[88] Iglič A, Babnik B, Gimsa U, Kralj-Iglič V. On the role of membrane anisotropy in the beading transition of undulated tubular membrane structures. *J. Phys A. Math.Gen.*2005;38(40): 8527–8536.

[89] Kralj-Iglič V, Remškar M, Vidmar G, Fošnarič M, Iglič A. Deviatoric elasticity as a possible physical mechanism explaining collapse of inorganic micro and nanotubes. *Phys.Lett.A.* 2002;296(2):151-155.

[90] Iglič A, Tzaphlidou M, Remškar M, Babnik B, Daniel M, Kralj-Iglič V. Stable Shapes of Thin Anisotropic Nano-strips. *Fuller.Nanotub Car.N.* 2005;13(3):183-192.

[91] Carmo MP. *Differential Geometry of Curves and Surface*. New Jersey: Prentice-Hall, 1976.

[92] Hafftka A. Differencial topology and the Poincare-Hopf theorem. The university of Chicago. http://www.math.uchicago.edu/~may/VIGRE/VIGRE2009/REUPapers/Hafftka.pdf/.Published November 10, 2009. Accessed December 21, 2018.

[93] Wright A, Dixon K. The Poincare-Hopf theorem. *The Open Math. Jour.* 2008;1:1-11.

[94] Poincaré H. Mémoire sur les courbes définies par une équation différentielle. J. *Math. Pure Appl.* 1881;7(3):375-422.

[95] Vitelli V, Turner AM. Anomalous Coupling Between Topological Defects and Curvatur. *Phys. Rev. Lett.* 2004;93(21)215301(1-4).

[96] Selinger R, Konya A, Travesset A, Selinger J. Monte Carlo Studies of the XY Model on Two-Dimensional Curved Surfaces. *J. Phys. Chem. B.* 2011;115(48): 13989–13993.

[97] Campbell MG, Tasinkevych M, Smalyukh II. Topological Polymer Dispersed Liquid Crystals with Bulk Nematic Defect Lines Pinned to Handlebody Surfaces. *Phys. Rev. Lett.* 2014;112(19):197801(1-5).

[98] Silvestre NM, Liu Q, Senyuk B, Smalyukh II, Tasinkevych M. Towards Template-Assisted Assembly of Nematic Colloids. *Phys. Rev. Lett.* 2014;112(22):225501(1-5).

[99] Muševič I, Škarabot M, Tkalec U, Ravnik M, Žumer S. Two-Dimensional Nematic Colloidal Crystals Self-Assembled by Topological Defects. *Science.* 2006;313(5789):954–958.

[100] Gharbi MA, Seč D, Lopez-Leon T, Nobili M, Ravnik M, Žumer S, Blanc C. Microparticles confined to a nematic liquid crystal shell. *Soft Matter.* 2013;9 (29):6911-6920.

[101] Colding TH, Minicozzi WP. Shapes of embedded minimal surfaces. *Proc. Of Nat. Acad.* 2006;103(30):11106-11111.

[102] Chabanon M, Rangamani P. Gaussian curvature directs the distribution of spontaneous curvature on bilayer membrane necks. *Soft Matter.* 2018;14(12)2281-2294.

[103] Euler L. *Methodus inveniendi lineas curvas: maximi minimive proprietate gaudentes sive solutio problematis isoperimetrici latissimo sensu accepti.* New York: Springer Science & Business Media; 1952.

[104] Mesarec L, Iglič A, Kralj S. Topological Defect Driven Membrane Fission. *Adv. Biomed. Res. Innov.* 2018;1(1):1-4.

[105] Beltrami E. Saggio di interpretazione della geometria non euclidea. *Gior. Mat.* 1868;6:248–312.

[106] Taioli S, Gabbrielli R, Simonucci S, Pugno NM, Iorio A. Lobachevsky crystallography made real through carbon pseudospheres. *J. Phys. Condens. Matter.* 2016;28(13);13LT01(1-5).

[107] Ovchinnikov A. *Nonlinearity and Geometry.* Warsaw: ed D Wójcik and J Cieślińnski; 1998.

[108] Hilbert D. Uber Flächen von konstanter Gausscher Krümmung. *Trans. Amer. Math. Soc.* 1901;2:87-99.

[109] Funkhouser CM, Sknepnek R, Cruz MO. Topological defects in the bucklig of elastic membranes. *Soft Matter.* 2013;9(1):60-68.

[110] Tilley RJD. *Defects in solids.* Hoboken NJ: Wiley Press; 2008.

[111] Chuang I, Duffer R, Turok N, Yurke B. Cosmology in the Laboratory: Defect Dynamics in Liquid Crystals. *Science.* 1991;251(4999):1336-1342.

[112] Brinkman WF, Cladis PE. Defects in liquid crystals. *Physics Today.* 1982;35(5):48-54.

[113] Tchernyshyov O, Chern GW. Fractional vortices and composite domain walls in flat nanomagnets. *Phys. Rev. Lett.* 2005;95(19):197204(1-4).

[114] Chern GW, Youk H, Tchernyshyov O.Topological defects in flat nanomagnets: The magnetostatic limit. *J. Appl. Phys.* 2006;99(8):08Q505 (1-3).

[115] Kleman M. Bloch and Néel Disclination Lines in a Small Anisotropy Ferromagnet. *Phys. Rev. B.* 1976;13(7):3091-3108.

[116] Braak HP, Caspeks WJ. Point defects in ferromagnets. *Phys. status solidi B.* 1967;24:733-741.

[117] Vachaspati T. Topological defects in the cosmos and lab. *Contemporary Physics.* 1998;39(4):225- 237.

[118] Kibble TWB. Topology of cosmic domains and strings. *J. Phys. A-Math. Gen.* 1976;9:1387-1398.

[119] Luckhurst GR, Sluckin TJ. *Biaxial Nematic Liquid Crystals: Theory, Simulation and Experiment.* Chichester: Wiley Press; 2015.

[120] Poulin P, Stark H, Lubensky T, Weitz D. Novel colloidal interactions in anisotropic fluids. *Science.* 1997;275:1770–1773.

[121] Kurioz P, Kralj M, Murray BS, Rosenblatt C, Kralj S. Nematic topological defects positionally controlled by geometry and external fields. *Beilstein J. Nanotechnol.* 2018; 9:109–118.

[122] Volovik GE. Topological singularities on the surface of an ordered system. *JETP Lett.* 1978;28(2):59-62.

[123] Cordoyiannis G, Losada-Pérez P, Tripathi CSP, Rožič B, Tkalec U, Tzitzios V, Karatairi E, Nounesis G, Kutnjak Z, Muševič I, Glorieux Ch, Kralj S, Thoen J. Blue phase III widening in CE6-dispersed surface-functionalised CdSe nanoparticles. *Liq. Cryst.* 2010;37(11):1419-1426.

Bibliography

Publications Related to the Thesis

Journal Articles

Kralj S, Mesarec L, Kurioz P,Rzoska S,Iglič A. Topological Defects: from Simplicity to Complexity. *GJSFR-A*. 2017;17(3):23-43.

Mesarec L, Kurioz P, Iglič A, Góźdź W, Kralj S. Curvature-Controlled Topological Defects. *Crystals*. 2017;7(6):*153(1-11)*.

Kurioz P, Kralj M, Murray BS, Rosenblatt C, Kralj S. Nematic topological defects positionally controlled by geometry and external fields. *Beilstein J. Nanotechnol*. 2018;9:109-118.

Kurioz P, Mesarec L, Iglič A, Kralj S. Assembling of Topological Defects at Neck-Shaped Membrane Parts [published ahead of print January 21, 2019]. *Phys. Status Solidi A*. 2019;1:1800722(1-10).

Biography

Personal Information:
Pavlo Yuriiovych Kurioz
Nationality: Ukrainian;
Date of Birth: 11.06.1991;
Place of Birth: Kyiv, Ukraine;
Marital Status: single.

Education

Physics-Bachelor student *Faculty of Physics, Taras Shevchenko National University of Kyiv*	01.09.08-30.06.12
Physics-Master student *Faculty of Physics, Taras Shevchenko National University of Kyiv*	01.09.12-30.06.14
Nanoscience and Nanotechnology-PhD student *Jožef Stefan International Postgraduate School*	01.09.14-Present